The Stability at the Solid-Solid and Liquid-Solid Interfaces

Junfeng Xiao

Submitted in partial fulfillment of the
requirements for the degree of
Doctor of Philosophy
in the Graduate School of Arts and Sciences

COLUMBIA UNIVERSITY

2016

ABSTRACT

The Stability at the Solid-Solid and Solid-Liquid Interfaces

Junfeng Xiao

In this thesis, we studied three small subjects in the realm of continuum mechanics: imbibition in fluid mechanics, beam and rod buckling in solid mechanics and shell buckling at the solid-liquid interface.

In chapter 2, we examined the radial imbibition into a homogenous semi-infinite porous media from a point source with infinite liquid supply. We proved that in the absence of gravity (or in the regime while gravity is negligible compared to surface tension), the shape of the wet area is a hemisphere, and the radius of the wet area evolves as a function with respect to time. This new law with respect to time has been verified by Finite Element Method simulation in software COMSOL and a series of experiments using packed glass microsphere as the porous media. We also found that even though the imbibition slows down, the flow rate through the point source remains constant. This new result for three dimensional radial imbibition complements the classic Lucas-Washburn law in one dimension and two dimensional radial imbibition in one plane.

In chapter 3, we studied the elastic beam/rod buckling under lateral constraints in two dimension as well as in three dimension. For the two dimensional case with unique boundary conditions at both ends, the buckled beam can be divided into segments with

alternate curved section and straight section. The curved section can be solved by the Euler beam equation.The straight sections, however, are key to the transition between different buckling modes, and the redistributed length of straight sections sets the upper limit and lower limit for the transition. We compared our theoretical model of varying straight sections with Finite Element Method simulation in software ABAQUS, and good agreements are found. We then attempted to employ this model as an explanation with qualitative feasibility for the crawling snake in horizontal plane between parallel walls, which shows unique shape like square wave. For the three dimensional buckling beam/rod confined in cylindrical constraints, three stages are found for the buckling and post buckling processes: initial two dimensional shape, three dimensional spiral/helix shape and final foldup/alpha shape. We characterized the shape at each stage, and then we calculated the transition points between the three stages using geometrical arguments for energy arguments. The theoretical analysis for three dimensional beam/rod are also complemented with Finite Element Method simulations from ABAQUS.

In chapter 4, we investigated the buckling shape of solid shell filled with liquid core in two dimension and three dimension. A material model for liquid is first described that can be readily incorporated in the framework of solid mechanics. We then applied this material model in two dimensional and three dimensional Finite Element Method simulation using software ABAQUS. For the two dimensional liquid core solid shell model, a linear analysis is first performed to identify that ellipse corresponds to lowest order of

buckling with smallest elastic energy. Finite Element Method simulation is then performed to determine the nonlinear post-buckling process. We discovered that two dimensional liquid core solid shell structures converge to peanut shape eventually while the evolution process is determined by two dimensionless parameters $K\tau/\mu$ and $\rho R^2/\mu\tau$. Amorphous shape exists before final peanut shape for certain models with specific $K\tau/\mu$ and $\rho R^2/\mu\tau$. The two dimensional peanut shape is also verified with Lattice Boltzmann simulations. For the three dimensional liquid core solid shell model, the post buckling shape is studied from Finite Element Method simulations in ABAQUS. Depending on the strain loading rate, the deformations show distinctive patterns. Large loading rate induces herringbone pattern on the surface of solid shell which resembles solid core solid shell structure, while small loading rate induces major concave pattern which resemble empty solid shell structure. For both two dimensional and three dimensional liquid core system, small scale ordered deformation pattern can be generated by increasing the shear stress in liquid core.

In the final chapter, we summarized the discoveries in the dissertation with highlights on the role that geometry plays in all of the three subjects. Recommendations for future studies are also discussed.

Table of Contents

List of Figures

List of Tables

Acknowledgements

First and foremost, I would express my sincere thanks to my advisor, Professor Xi Chen. Professor Chen encourages creativities from students while maintaining the premier standard of scientific researches. He always guided me with his great patience and inspired me with keen perception of mechanics. Professor Chen sets a model that will be followed in my own endeavor. I am also grateful of Professor Qiao Lin, my advisor at Department of Mechanical Engineering, for his timely assistance.

I would also like to thank the thesis committee, Professor James Hone, Professor Arvind Narayanaswamy, Professor Gautam Dasgupta, Professor Qiao Lin and Professor Xi Chen for their participations in the thesis defense and their valuable suggestions.

I couldn't proceed as a PhD student without the support from my parents and other family members. The whole family has created a caring and understanding environment since I was a litter child. At the same time, the pursuit of knowledge and excellences has been instilled to me through my grandfather and my parents' self-practice, and I shall follow that as a motif in my future journey. At last, I would pay my special tribute to my grandfather who passed away in November of 2013. My grandfather expected my graduation in his last days, so I must dedicate this thesis and degree to my beloved grandfather.

I also need to thank the colleagues in the lab for the past few years, who were an

integral part of a vibrant life at Columbia: Jun Xu, Hang Xiao, Xiaoyang Shi, Baoxing Xu, Xiangbiao Liao, Yu Cheng. For most of nights are spent with you in the lab and most of meals are dined with you in joy. I also have the fortune to work with other members in Professor Chen's group, which is truly a diverse and aspiring team. The collaborations with Zixiang Tong and Xiangbiao Liao are inspiring and fruitful. Apart from that, a unique experience was started since 2009 together with colleagues in Mechanical Engineering, such as Te Li, Lei Wang, Yuanda Gao, Jianzhong Zhu, Fan Zhang, Brian Jones and other fellows. Our friendship shall long last.

I should not forget the first two years at Mechanical Engineering, and the help from my former advisor Professor Daniel Attinger. It is Professor Attinger who brought me to Columbia and led me to the field of fluidics. Chapter two in this thesis was finished under his supervision. Professor Attinger taught me the rigor of academics and it is a hallmark I will proudly wear in my own research. I would also say thanks for my former colleagues at LMTP who helped me a lot during my initial adjustment to US life: Amy Betz, Michael Grad, Jie Xu, Erik Huber, Rajneesh Bhardwaj, Liqun Fu and our members of LMTP.

Collaborations with Professor Howard Stone at Princeton University Professor David Hu at Georgia Institute of Technology are greatly appreciated.

China Scholarship Council must be acknowledged for their financial support.

Dedicated to my grandfather

Chapter 1.Introduction and Motivation

1.1 Fluid mechanics, solid mechanics and the interface

The two branches of continuum mechanics, fluid mechanics and solid mechanics, are the main subjects of this thesis. Continuum mechanics is formulated on the principles of Newtonian mechanics, *i.e.* classic mechanics, and is the foundation of a lot of aspects in today's engineering and science. As represented in Figure 1.1, mechanics originally stems from the contact at the interface of two mediae, which can be either solid or fluid. The form of media can be three dimensional bulk, two dimensional shell or one dimensional beam; the shape of interface can be planer or with curvature; interface can be an open geometry or a closed geometry. Caused by some physical and chemical processes which will be detailed in the following chapters, instabilities develop at the interface. The instability will introduce abrupt and morphological changes, rather than gradual and incremental changes, to the interface. This thesis will discuss when these instabilities develop, and if there are multiple unstable states, when does the system transit from one state to another.

To study every specific direction of ever expanding fields in each of the mechanics seems impossible at this era, so only a few topics about instability at the interface will be covered in this thesis. To be specific, beam buckling under lateral constraints and buckling of solid shell liquid core structure are the focus of this thesis, which respectively represents the instability at solid-solid interface and solid-liquid interface. In addition to that, three

dimensional radial imbibition is also investigated, as an exploration in the field of fluid mechanics and as precursor for the following study of fluid-solid interaction.

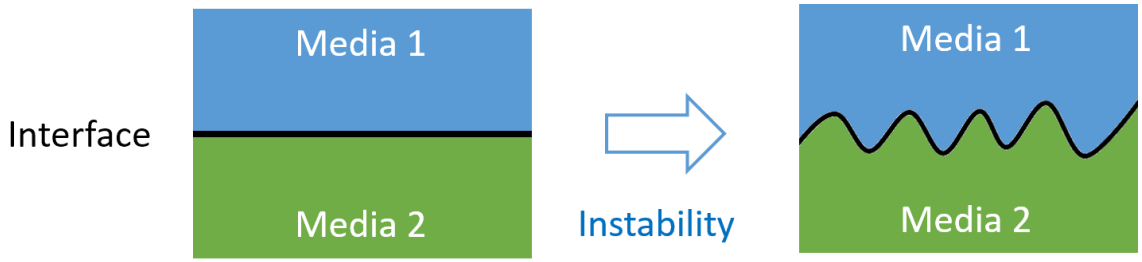

Figure 1.1 Instability at the interface between two mediae. Media 1 and 2 can be either fluid or solid.

1.1.1 Low Reynolds flow: imbibition

Studies in Newtonian fluid mechanics are divided by the Reynolds number of the fluid flow. Flow with Reynolds number smaller than 2300 is laminar flow, while flow with Reynolds number larger than 2300 is turbulent flow. Our studies in this thesis is focusing on the laminar flow regime. With the advent of miniature of mechanic devices, *i.e.* Micro Electrical Mechanical System (MEMS) and Nano Electrical Mechanical System (NEMS), the Reynolds number in these system comes to value around or below 1. Because of size effect, body forces pale compared to surface forces at the small scale, so surface tension becomes the dominant force in the extreme low Reynolds flow regime. Therefore flow related with surface tension, or more broadly microfluidics, is recently a vibrant research area with immediate applications in physical, chemical and biological studies [1-3].

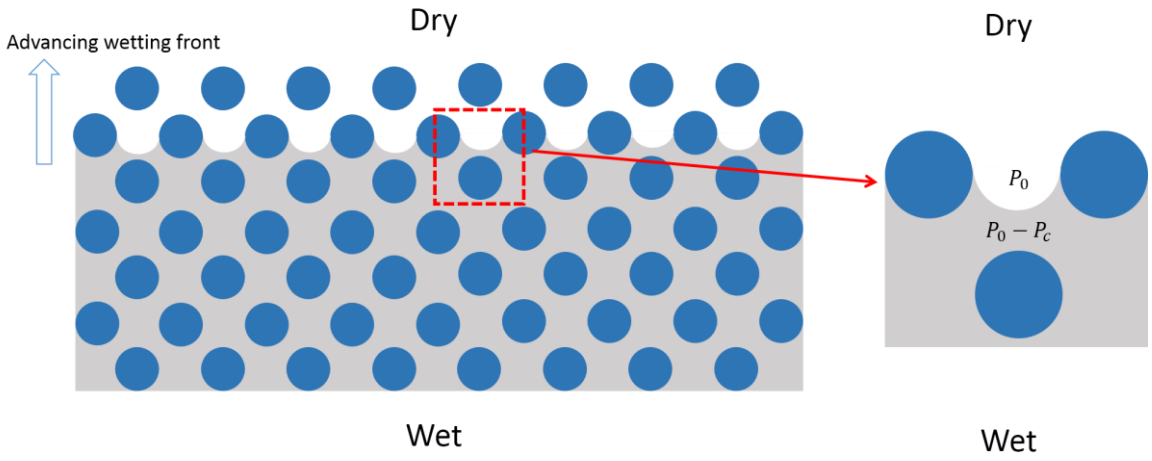

Figure 1.2 Saturated imbibition in the porous media with advancing wetting front where the porous structure is presented by blue dots and liquid is represented by grey region, the capillary pressure P_c on the wetting front is illustrated together with atmospheric pressure P_0 in the zoomed red square.

Imbibition is a flow driven by pressure gradient in porous media, and in our cases we only studied saturated imbibition in the laminar flow regime. In the porous material with micro sized pores, the pressure gradient is usually originated from capillary pressure P_c at the wetting front. Therefore surface tension at the meniscus in Figure 1.2, which causes the capillary pressure, is the driving force in our studies of imbibition. We will use theoretic, numerical and experimental techniques widely used in microfluidics to analyze the imbibition process under a new geometrical constraints.

1.1.2 Stability of solid structure: buckling

Based on the responses of solids to applied stress, studies of solid mechanics can be divided into different regimes: elastic, viscoelastic and plastic. Our study in this thesis will focus on the elastic regime. While a lot of solid mechanics involves dynamics study,

we will look at the static solid structure without motion. However, as the loads (usually compressive stresses) are imposed on the static structure, the structure will gradually deform to a certain point when its shape abruptly changes. This transition when the stability of solid structure in static equilibrium is lost is called buckling. Mathematically speaking, the buckling is corresponding to a point where bifurcating solutions exit for the same equations, with one of the solutions greatly deviating from the initial shape.

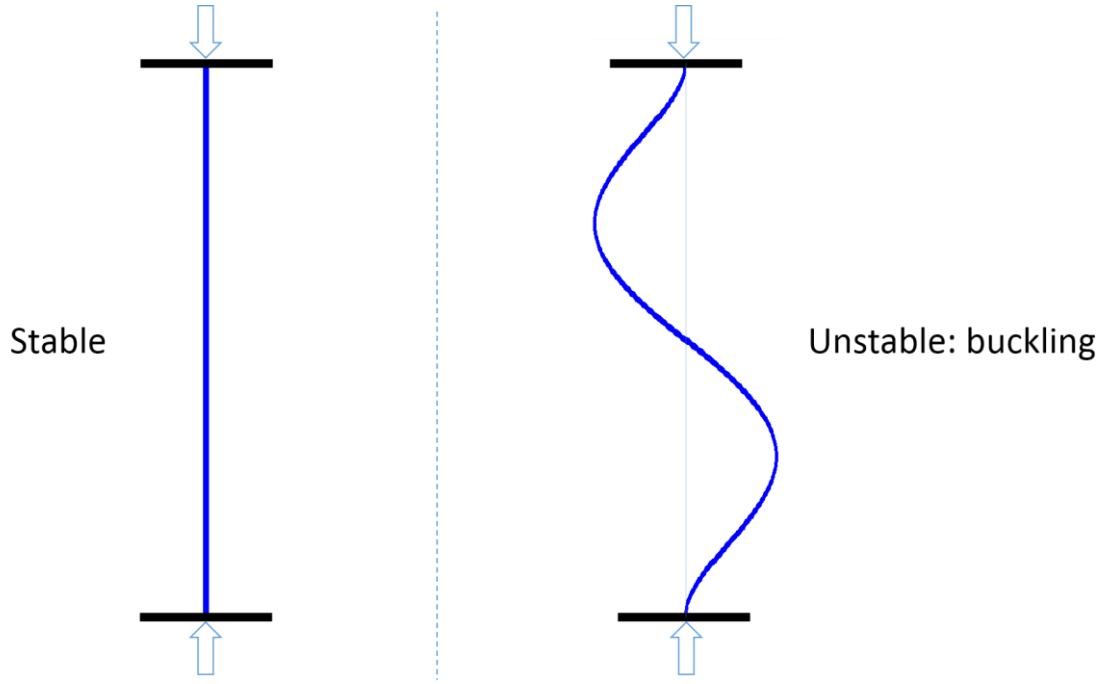

Figure 1.3 Stability of compressed elastic beam: initial straight shape are compared to the buckled tenuous shape.

The buckling of solid structure is typically associated with failure since it deviates from original functional shape which is usually designed to be so. For example the straight rail ways becomes distorted in summer because of the thermal expansion at high temperature induced compression in the steel rail, which is illustrated in Figure 1.3. But

recently researchers have also attempted to guide the buckling process to generate desired shape [4, 5], and it is a novel technique in the category of self-assembly [6].

In addition to the studies of specific topics in fluid mechanics and solid mechanics, we are trying to bridge the two distinct subjects by studying the third topic, the shell buckling at the fluid/solid interface. This third topic requires understanding in both fluid mechanics and solid mechanics, with more emphasis on the stability of solid structure. It is a small attempt in the large and expanding field of Fluid-Solid Interaction.

This thesis is by no means an inclusive study in every aspects of mechanics, but is trying to organize the research discoveries under a coherent theme.

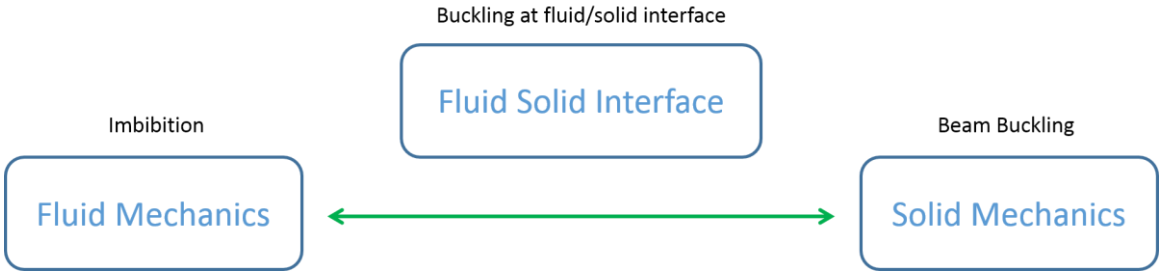

Figure 1.4 Three subjects of this dissertation

1.2 Methodology

The classic fluid mechanics and solid mechanics are described by sets of Partial Deferential Equations (details will be discussed in following specific chapters). Depending on the nature of problem, different techniques would be used towards these problems.

The governing equation of imbibition, Darcy's law in (2.1), is a first order PDE and only involves single spatial parameter in our cases. This series of PDEs can be solved

analytically, and relevant problems have been well documented in literature [7, 8]. So we could expand previous analysis into our problem in different geometries, and new physical laws can be discovered in this manner. This is how we tackled the imbibition problem in chapter 2.

The shape of buckling elastic beam without contact can be described by Euler-Bernoulli beam theory for small deflection problems. In contrary, the contact between beam and constraints divides the beam into several segments whose general shape can't be characterized by a single equation. However, the single section can indeed be described by the beam theory. So in chapter 3 we propose to solve the problem segments by segments, then lump segments together to construct the shape of whole beam. This constructed analytical solution is then compared with the numerical solution from Finite Element Method software ABAQUS. Good agreement between theory and simulation is found, indicating the validation of lumping scheme. Nevertheless, a large part of the analysis is derived from the simulation results.

In chapter 4, the system consists of two separate phases: solid shell and liquid domain. The solid shell itself is usually described by Foppl-Von Carman model which is a fourth order nonlinear PDE. Coupled with the liquid domain, this system is difficulty to solve analytically. We could only draw general yet valuable information from the linear stability analysis based on principle of energy minimization, such as wave number and general shape of the system at the onset of buckling. The exact shape has to be solved

numerically and the characterization of the buckling shape comes from Finite Element Method simulation, especially for large deformation post buckling shapes.

The basics of Finite Element Method for fluid mechanic and solid mechanics have been documented in various textbooks, and they are well implemented in commercialized software packages [9, 10], so they will not be repeated here. However, two special techniques with regarding to FEM in our studies will be discussed in this section.

The first technique, Arbitrary Lagrangian Eulerian (ALE) method, is used to account for the changing of computation domain in fluidic simulation. Fluid is usually described in the Euler formulation, *i.e.* the computation domain is fixed with time. But ALE method can redistribute the mesh in the liquid domain to represent the deforming boundary, so it is useful in the simulation of Fluid-Solid Interaction (FSI) or deformation of droplet or bubble. In our study, the evolution of wetted area is simulated with ALE method in FEM software COMSOL.

The second technique is used in the post buckling analysis of FEM software ABAQUS. The conventional post buckling analysis takes the results of linear buckling analysis as the implanted defects, and then run the static implicit analysis to obtain the final deformation. In our post buckling analysis, we utilized dynamic explicit scheme to simulate the quasi-static process for buckling. The advantage is that the computations converge without tenuous iteration processes, so the simulation is robust while maintaining its accuracy (kinetic energy should be controlled at a very low level to avoid the unnecessary

dynamic effects). In addition to that, an arbitrary small force in a very short time interval is added to the system as a perturbation to break its initial equilibrium instead of implanting defects in the geometry.

Theoretic analysis and numerical simulation can provide qualitative and quantitative information about the studied object, while experiments offer the much needed verification for the analysis. Experiments are performed whenever possible to form an integral part of study. In chapter 2, the experiments are meticulously designed and implemented to measure the wetted area [11]. The related material parameters such as porosity and diffusivity are also determined through experiments. In chapter 3, the experiments of snake locomotion are performed by Professor David Hu at Mechanical Engineering of Georgia Institute of Technology. In chapter 4, representative experiments are done jointly with Professor Ponisseril Somasundaran at Earth and Environmental Engineering of Columbia, but the results are not reflected in this thesis.

The three strategies, theory, simulation and experiment, should be deployed together to ensure a self-contained result. In reality, at least two of the three strategies are used to verify each other's conclusion in each of the chapters.

1.3 Outline of Dissertation

Each subjects of the thesis are handled as a self-contained topic, so each chapter is treated differently with its own introduction and conclusions, but some of the general

understandings will be discussed in final conclusion of chapter 5.

In chapter 1, three subjects of the thesis are framed, and their relation are discussed to illustrate the holistic characteristic of the thesis. Three difference strategies in this thesis, *i.e.* theory, simulation and experiments, are previewed briefly and will be discussed in depth in the following chapters.

In chapter 2, the three dimensional radial imbibition are analyzed theoretically and numerically (in COMSOL), and the results are verified by ensuing experiments. A new law relating wetting area to time is discovered. The radial size of wetted area in three dimensional radial imbibition are compared with classic Lucas-Washburn law (one dimensional imbibition) and radial size of wetted area in two dimensional radial imbibition.

In chapter 3, the buckling beam under lateral constraint are studied theoretically and numerically in both two dimensional case and three dimensional case. The emphasis is put on the shape of buckled beam and the transition between different buckling modes. In the two dimensional case, FEM model is utilized to explain the unique shape discovered in the crawling snake between two parallel walls.

In chapter 4, the buckling of solid shell/liquid core system is examined mostly in the numerical simulation, with complemental linear stability study from the theoretical analysis based on principle of energy minimization. Special efforts are allocated on constructing maps for deformation patterns according to key parameters. The difference between solid core system and liquid core system is also discussed. The analyses are first

performed in two dimensional geometries, and then expanded into three dimensional geometries.

Finally, in chapter 5, the discoveries in this thesis are summarized, and recommendations on future studies are also listed in this chapter.

Chapter 2.Three Dimensional Imbibition from Point Source into Porous Material

2.1 Introduction to imbibition

When a liquid contacts a dry porous medium or an empty capillary tube with a wetting angle smaller than 90°, it is propelled by capillary forces into the medium or the tube. This motion is resisted by viscous forces. As reviewed in reference [12], the phenomenon of diffusive imbibition is of importance for fluid transport in plants and soils, and in industrial processes such as printing, oil recovery, cooking, wine filtering, fabrication of composite materials, behaviors of garments. The forensic discipline of bloodstain pattern analysis would also benefit from a better understanding of stain formation on clothes or carpets for example [13, 14]. More recently, researchers proposed to build low cost microfluidic devices made of paper where imbibition is utilized as the driving force of the flow process [15, 16], so that the pumps and channels becomes unnecessary and microfluidic devices become readily disposable. As devices are scaled down into micro or nano size, surface tension becomes a dominant force, so that imbibition process induced by capillary force should come into consideration in terms of design of Micro Electrical Mechanical System (MEMS) or Nano Electrical Mechanical System (NEMS). This chapter would contribute to imbibition theory in three dimensional geometries, and it's a combination of theoretical analysis, numerical simulation and

experiment verification.

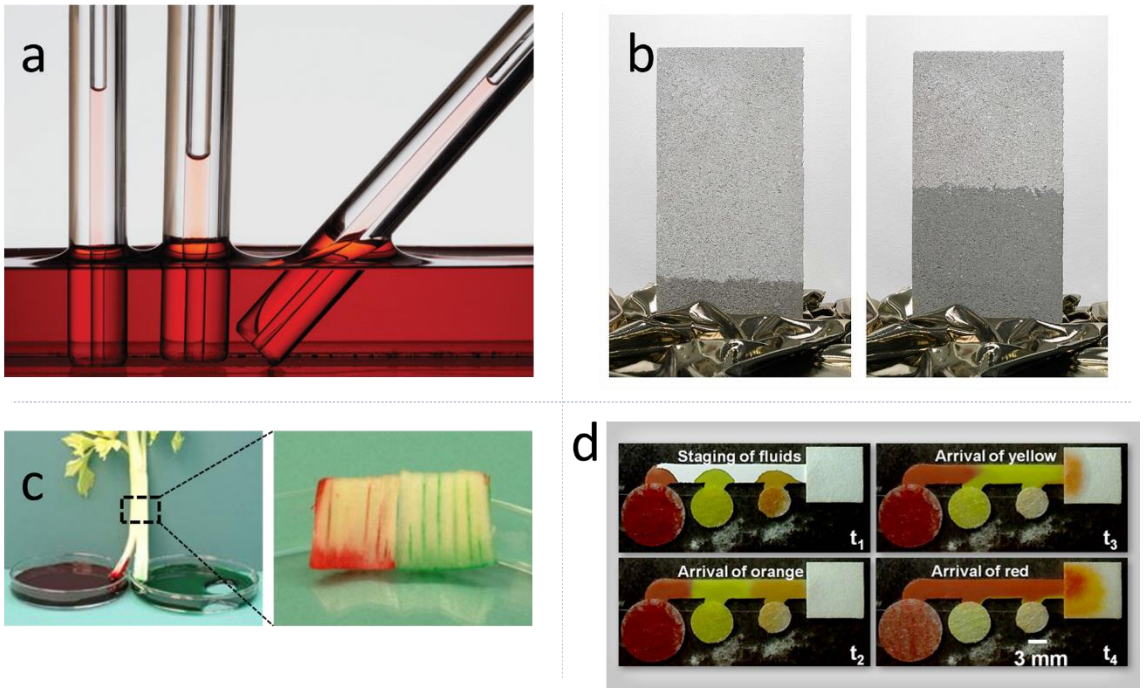

Figure 2.1 Imbibition in different scenarios. a) Imbibition in capillary tubes; b) imbibition in brick; c) imbibition in plant stem; d) paper based microfluidic device [15].

2.1.1 Classic law of imbibition

In an one-dimensional geometry such as a porous rectangular strip or a capillary tube as illustrate in Figure 2.1, the wetting front advances according to a power law $l^2 = Dt$, with l indicates the distance from source to wetting front, D a coefficient that depends on the properties of porous medium and the liquid, and t the time. This law is best known as the 'Lucas-Washburn law' [3, 17] proposed in the 1920s, and is also described as 'diffusive imbibition' [18]. Recently, researchers have proved that this law is applicable to nanoscale porous material [19]. The Lucas-Washburn law is briefly reviewed in this section.

We start from Darcy's Law described in equation (2.1), which depicts the flow

velocity in porous material is proportional to pressure gradient:

$$\mathbf{v} = -\frac{k}{\mu}\nabla p \tag{2.1}$$

where k, μ and $\mathbf{v}$ respectively represent the permeability (m^2) of the porous medium, dynamic viscosity (Pa·s) of the liquid and the average velocity at the advancing dry/wet interface. Here the porous material is assumed to be homogeneous and isotropic, so that the permeability k is a scalar without directional dependence. If liquid loss due to evaporation from the porous media can be neglected, mass conservation for an incompressible flow yields

$$\nabla \cdot \mathbf{v} = 0, \text{ so that } \nabla^2 p = 0 \tag{2.2}$$

In equation (2.1), velocity $\mathbf{v}$ at the wetting front is actually dl/dt and pressure difference between source and wetting front is capillary pressure as illustrated in Figure 1.2 and Figure 2.1. So gradient of pressure in the flow field is p_c/l. p_c represents the capillary pressure at the wetting front which usually depends on the size of pores and surface tension of liquid and is a constant throughout the process, the calculation of capillary pressure will be discussed in the following sections. Substituting velocity and pressure gradient in equation (2.1) yields

$$l\frac{dl}{dt} = \frac{k}{\mu}p_c \tag{2.3}$$

Integration of both sides of above equation gives the evolution of wetting front with respect to time:

$$l = \left(\frac{2kp_c}{\mu}\right)^{1/2} t^{1/2} \tag{2.4}$$

Equation (2.4) is the classic result for one dimensional imbibition process proposed by Washburn. Underwent appropriate scaling process, equation (2.4) can be written in nondimensionalized form:

$$L = T^{1/2} \tag{2.5}$$

This Washburn-Lucas law in (2.5), however, only applies to imbibition in one dimensional porous material or imbibition in capillary tubes. The imbibition in other geometries are deviating from the classic law, so we sort to examine the geometry's effect on the imbibition. And we shall exemplify the geometry's role by comparing the radial imbibition in two dimensional space and radial imbibition in three dimensional space.

2.1.2 Deviation from classic imbibition law

Recently imbibition has been studied for geometries with more than one dimension. For example, Clarke *et al*. [20], Anderson [21] and Hilpert and Ben-David [22] modeled the imbibition of a finite-size droplet into a porous medium, accounting for the deformation of the drop while assuming that the pores fill in the normal direction to the surface of the porous medium. Oko *et al*. [23] used high-speed imaging to measure the imbibition and evaporation of picoliter water droplets on paper media commonly used for inkjet printing. Reyssat *et al*. [18] studied the imbibition in a cone geometry with small opening angle α, and showed that at later times the imbibition varied as $L \sim T^{1/4}$. Mason *et*

al. [24] studied analytically imbibition towards the center of porous cores with cylindrical, spherical and toroidal geometries. Also, Mendez *et al*. [8] described the two-dimensional imbibition process in a thin porous membrane with a fan shape, specifically a rectangular sector attached to a circular sector, and expressed the deviation from the Lucas-Washburn law in the circular sector. In summary, Lucas-Washburn law fails when geometries change from one dimension to higher dimension.

In this chapter, we describe the imbibition process from a point source into a three dimensional homogeneous semi-infinite porous material and two dimensional homogeneous semi-infinite porous material, and it shows prominent deviation from one dimensional Lucas-Washburn Law.

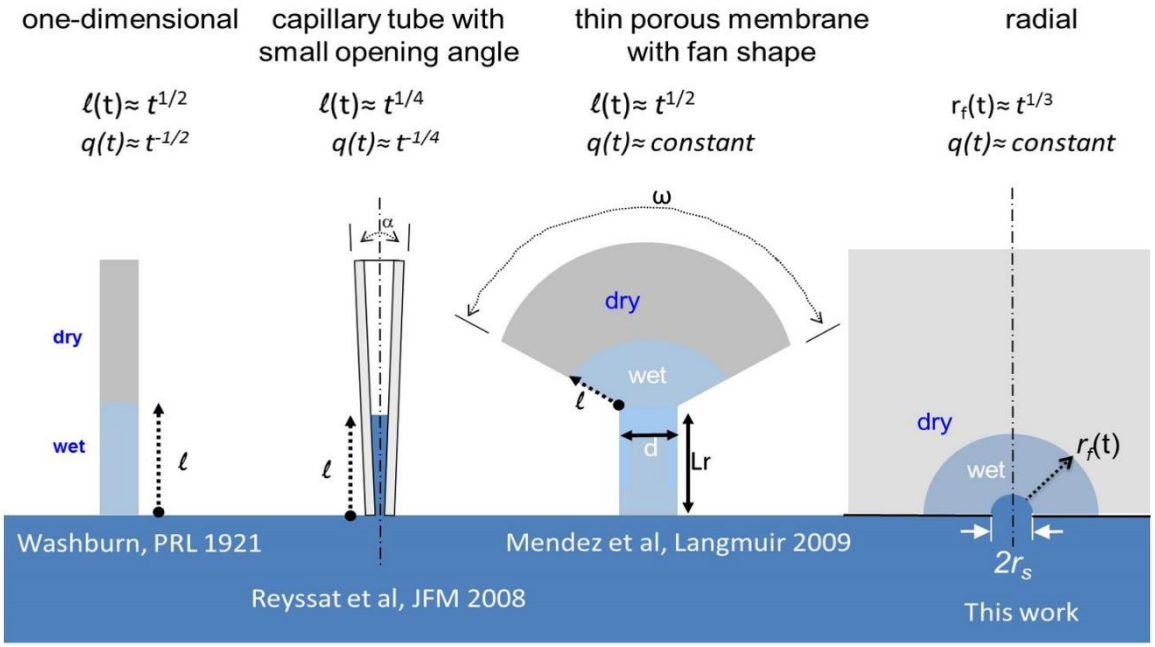

Figure 2.2 Imbibition in different geometries. From left to right, four analytical solutions for imbibition in porous media: one dimensional imbibition process that obeys the Lucas-Washburn law [17]; imbibition in a capillary tube with small opening angle [18], in a thin, fan-shape membrane [8], and in the radial geometry

considered in this work. For each case the evolution of the wetted length l and flow rate q (at long times) are expressed as a power law of the time t.

2.2 Analytical solution for three dimensional imbibition from point source into semi-infinite porous material

The derivation also starts from Darcy's law as stated in equation (2.1) and conservation equation (2.2). The pressure difference, *i.e.* capillary pressure at wetting front is determined by the Laplace pressure:

$$p_c = \frac{2\gamma \cos\theta_c}{r_p} \tag{2.6}$$

where γ, r_p and θ_c are, respectively, the surface tension between the liquid and the atmosphere, a representative radius of the pores, and the contact angle of liquid on the porous material.

To better define the problem we are solving, we've made several standard assumptions before the derivation:

1.The source of liquid is small enough to be considered as a point source, which can provide an infinite liquid supply for the imbibition process.

2.The shape of the advancing liquid front is a hemisphere, so that liquid flows radially from the source to the advancing front and the radial velocity is uniform along the advancing front. The advancing wetting front of liquid is then defined in spherical coordinates as $r = r_f(t)$, with the pressure gradient only in radial direction.

3.The effect of gravity on the liquid flow is neglected, which means hydrostatic

pressure is much smaller than capillary pressure.

The volumetric flow rate of liquid $q(t)$ at the wetting front is advancing velocity times surface area:

$$q(t) = 2\pi r_f^2 u_r \tag{2.7}$$

where $u_r = dr_f/dt$ denotes the radial velocity of liquid at the advancing front. So the radial velocity can be expressed as a function of the pressure gradient using Darcy's Law (2.1):

$$-\frac{dp}{dr} = \frac{\mu q(t)}{2\pi r^2 k} \tag{2.8}$$

The pressure at the source is p_{atm}, while the pressure at the wetting front $r = r_f$ is $p_{atm} - p_c$. Equation (2.8) can be integrated spatially from source $r = r_s$ to the front $r = r_f(t)$ in order to obtain the pressure:

$$p_c = \frac{\mu q(t)}{2\pi k}\left(\frac{1}{r_s} - \frac{1}{r_f}\right) \tag{2.9}$$

Substituting volumetric flow rate (2.7) into (2.9):

$$r_f^2 \frac{dr_f}{dt}\left(\frac{1}{r_s} - \frac{1}{r_f}\right) = \frac{kp_c}{\mu} \tag{2.10}$$

This first order nonlinear ordinary differential equation for the position of the wetting front r_f can be integrated directly with $r_f = r_s$ as the initial condition:

$$\frac{1}{3r_s}\left(r_f^3 - r_s^3\right) - \frac{1}{2}\left(r_f^2 - r_s^2\right) = \frac{kp_c t}{\mu} \tag{2.11}$$

At long times, the r_f^3 term dominates, so (2.11) simplifies to:

$$r_f = \left(\frac{3kp_c r_s}{\mu}\right)^{1/3} t^{1/3} \tag{2.12}$$

According to equation (2.7), in this long time limit, the flow rate $q(t)$ is independent of time, expressed as:

$$q = \frac{2\pi kp_c r_s}{\mu} \tag{2.13}$$

Results (2.12) can be recast in a non-dimensional manner:

$$R(T) = T^{1/3} \tag{2.14}$$

by choosing dimensionless parameters as $R = r_f/r_s$ and $T = 3kp_c t/\mu r_s^2$.

2.3 Numerical solution for three dimensional radial imbibition from point source into semi-infinite porous material

Equation (2.1) and (2.2) are also solved in three dimensional axis-symmetrical coordinates using Finite Element Method package COMSOL. Since the wetting front is moving with time, Arbitrary Lagrangian-Eulerian (ALE) method is employed to account for the evolution of computational domain [9, 25]. An artificial initially wet area, which is depicted as dark grey area in Figure 2.3, is needed as start point of the simulation. This artificial initial wet area is the wet area after a short time interval Δt theoretically, Which means the simulation actually starts at $t(0)= \Delta t$. Since the advancing velocity of wetting front is large due to the large gradient when t is barely larger than 0, Δt tends to be 0 for small initial wet area. Different shapes for the initial wet area such as elliptic and rectangular are tested, while the wet areas all become spherical eventually and the size of

wetting area converges which conforms the assumption 1 and 2. The shape indicated by z_s and r_s at different time is plotted in Figure 2.8.

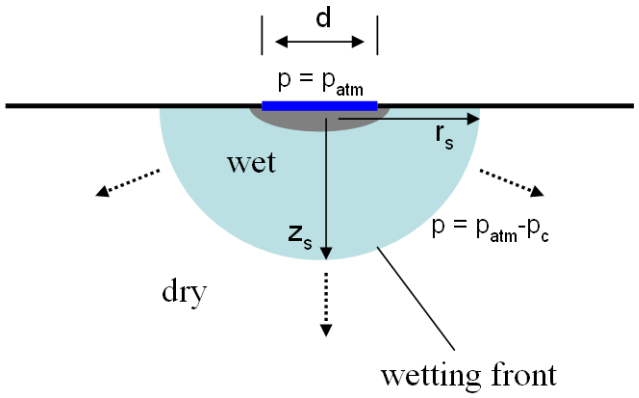

Figure 2.3 2D axis symmetrical model in COMSOL. Liquid source with diameter *d* is colored by dark blue, the artificial initial wet area is colored by dark grey and wet area after *t* is colored by light blue.

Boundary conditions for the pressure in simulation are explained in Figure 2.4. The boundary condition for mesh movement at wetting front is that normal component of mesh velocity equals normal component of liquid velocity, while the tangential velocity of mesh at wetting front is not constrained to improve the mesh quality. COMSOL disturbs the position of inner mesh nodes according to movement of boundaries to obtain a smooth mesh deformation everywhere. One thing to be noted is that quality of mesh deteriorates because mesh could be stretched and distorted as simulation continues, and the mesh is not appropriate for the simulation once it is inverted. So remeshing is needed when mesh quality drops below a criterion, simulation is then restarted from that stop point with new, better-quality mesh.

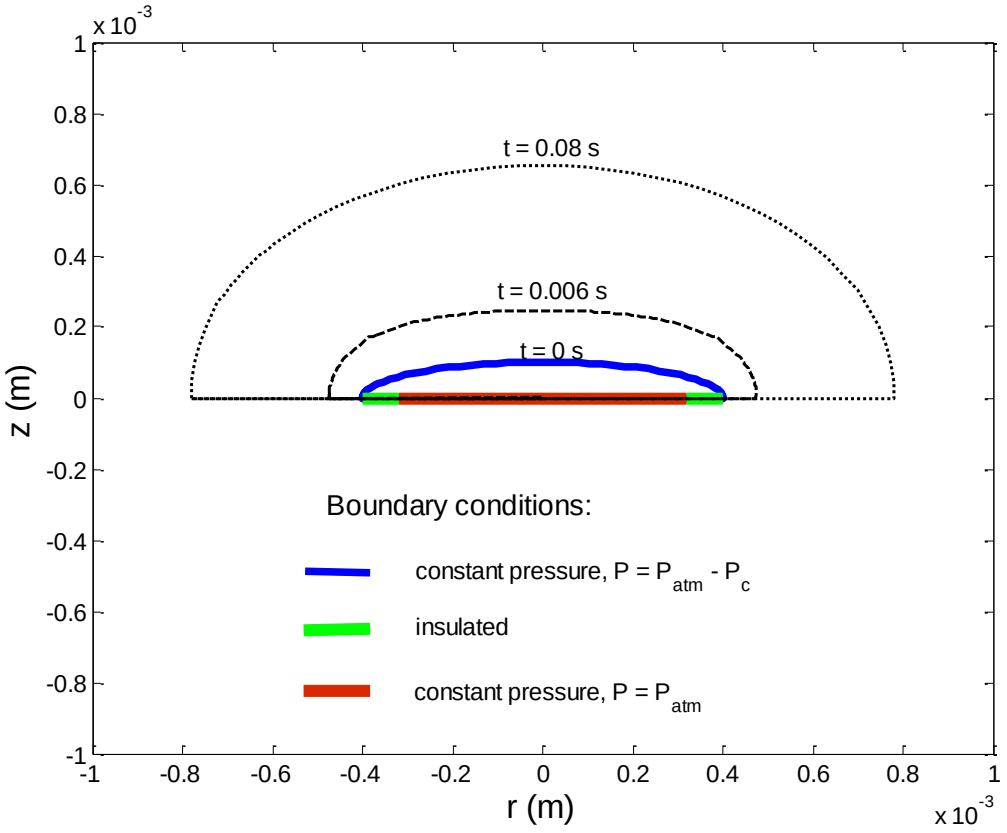

Figure 2.4 Wetting front at remeshing points. Three boundary conditions are also displayed in different colors: pressure at source, pressure at wetting front and boundary at the bottom plate.

2.4 Experimental verification for the analytical solution in three dimensional radial imbibition

Experiments were conducted to measure the evolution of a wetting front with respect to time. Soda lime glass microspheres (P2043SL, Cospheric LLC) were loaded in a polycarbonate box (60 mm x 60 mm x 60 mm) to form a porous medium in the experiments. The microspheres were well mixed in the box using an orbital shaker (miniRoto S56, Fisher Scientific) before each experiment to avoid inhomogeneities in the porous medium. The experimental setup is depicted in Figure 2.5.

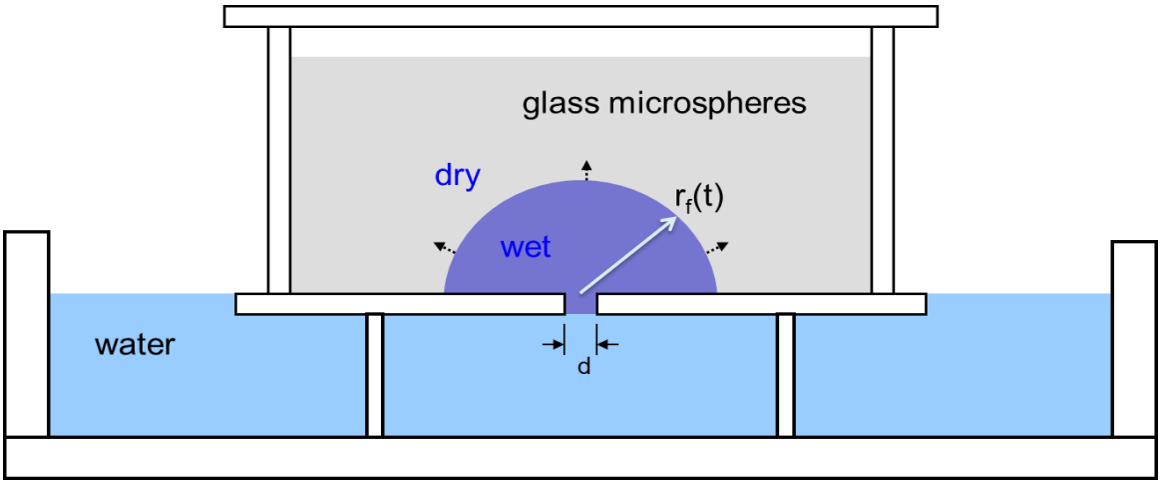

Figure 2.5 Experiment setup for the imbibition measurement

To measure the particle size, the microspheres were immobilized in water between a microscope slide and cover slide, and imaged under an inverted microscope. A MATLAB code was developed to determine the size of 3000 microspheres: the average diameter d_m was measured to be 42 μm, with standard deviation $\sigma = 7$ μm (see Figure 2.6). The porosity was measured to be 0.36 ± 0.02, by comparing three times the weight of an 8 mL beaker filled with dry sand to the same system wetted with water. This porosity value is slightly lower than values measured for packed beds of same size glass particles, as e.g. in reference [26] where particles with diameter of 40 μm were measured to have average porosity of 0.45. The porosity value found in our study is very close however to the porosity of 0.38 ± 0.02 measured in packed beads [27] with grains size between 40 and 300 μm.

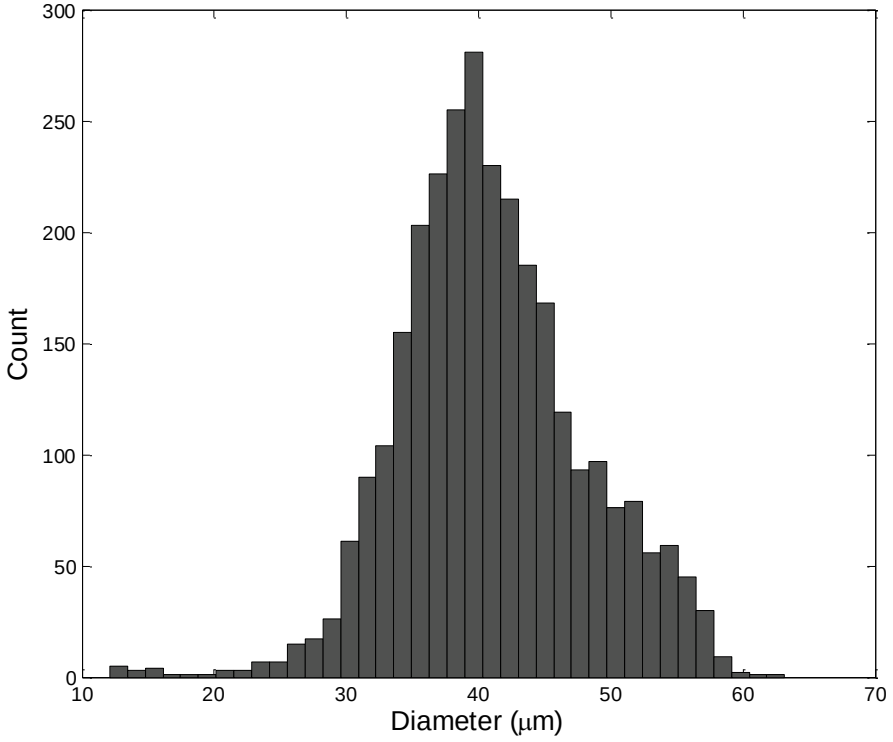

Figure 2.6 The measured size distribution of glass microspheres used in the experiments.

Two important parameters in equation (2.12) need to be determined, namely the permeability k and capillary pressure p_c. For a random packing of microspheres of uniform size, the permeability k of the porous media, as well as the porosity ε, can be determined numerically from the mean diameter of the microspheres d_m using simulations of random sequential deposition events, as shown in reference [28]. The permeability k of the porous media can also be related to the diameter of the microspheres d_m, and the porosity ε estimated using the Kozeny-Carman model [29]:

$$k = \frac{d_m^2}{180} \frac{\varepsilon^3}{(1-\varepsilon)^2} \tag{2.15}$$

We chose to measure the permeability experimentally. A water flow was driven

vertically through a Teflon tube (inner diameter 1.58 mm, length 100 mm) filled with glass microspheres, with the flow rate controlled by a syringe pump. A thin metal mesh membrane (15 μm, Betamesh, BOPP AG, Switzerland) with negligible pressure drop was attached to the exit of the tube to retain the microspheres. The pressure difference in the porous media was measured by a pressure gauge (DPG 110, Omega). Then the permeability of the porous media can be calculated from the measured pressure difference and flow rate according to Darcy's law. The permeability was measured to be $k = (1.21 \pm 0.07) \times 10^{-12}$ m^2. The experimental value of permeability is in good agreement with the value calculated using the Kozeny-Carman model [29] $k = 1.12 \times 10^{-12}$ m^2, or determined numerically in reference [28] as $k = 9.5 \times 10^{-13}$ m^2.

The capillary pressure was measured by a 1-D capillary rise experiment, where vertical imbibition is resisted by gravity, until an equilibrium height h is reached where the hydrostatic pressure is balanced by the capillary pressure, with

$$\rho g h = \frac{2\gamma \cos\theta_c}{r_p} \tag{2.16}$$

The final height h obtained experimentally corresponds to a capillary pressure of 3480 Pa +/-70 Pa. That value was used as the capillary pressure in equations (2.11) and (2.12), and in the results shown in Figure 2.7. If we assume, as in reference [27], that the largest pore size, *i.e.* the maximum radius of curvature, controls the capillary pressure, we can obtain independent values for r_p and θ_c as follows. The capillary pressure obtained by the capillary rise experiment corresponds by equation (2.16) to a maximum radius of curvature $\cos\theta_c/r_p$

= 2.39x104 m^{-1}. Neglecting the non-uniformity of the beads, we assume that all beads with diameter d_m are packed in a cubic face-centered arrangement, with unit cell distance $\sqrt{8}d_m/2$. From simple analytical geometry considerations, a relation can be established between the wetting angle and the largest radius of curvature [30]. Iterations between that relation and equation (2.16) converge towards values of a maximum radius of curvature of 33 μm, which corresponds to a maximum pore size of 26 μm and a wetting angle of 38°, respectively. These estimates are compatible with the actual bead radius (21 μm) and with published literature [31-33], where the wetting angle of water on soda lime glass was measured as 31°. Note that this method of determining independent values of r_p and θ_c is only provided as a side note, since the interpretation of the radial imbibition experiments studied in this paper only relies on the value of the capillary pressure measured in the 1-D capillary rise experiment.

The experimental setup to measure the dynamics of the imbibition process is illustrated in Figure 2.5. A hole with diameter d = 0.64 mm and length of 5.9 mm was drilled in the bottom plate (thickness 5.88 mm) as the inlet for the liquid. In the experiments, the height of the wet volume was always kept below 30 mm, which is a height corresponding to less than 10% of the capillary pressure generated by 42 μm spheres. The box loaded with microspheres was then put in a water-filled glass Petri dish, and the liquid level in the Petri dish was adjusted to be the same as the bottom surface of the polycarbonate box, which assures that pressure at the inlet is atmospheric and that the

imbibition process has access to a nearly infinite liquid supply. The liquid inlet hole was filled with microspheres, so that the wetting liquid reached the top side of the box bottom in less than 5 seconds, as measured by filling the box with a very thin layer of sand. This estimate is in good agreement with predictions from the Lucas-Washburn law, which estimates the invasion time to be less than 1 second. Experiments with fluids that fully wets glass (silicone oils) were inconclusive because spreading proceeded faster along the plastic container walls than in the sand and produce a flat pancake-shaped wetted region in the sand.

The box was capped during the experiments to avoid evaporation. In order to determine the time dependence of the imbibition front the wet region was measured at different time intervals. In particular, after a given time interval, all of the dry microspheres were poured out of the box by gravity [7], by suddenly turning the box upside down. Microspheres in the wet volume stuck to each other due to capillary adhesion caused by water between the spheres. The wet region also adhered to the bottom plate of polycarbonate box, The shape of the wet volume (photographed in Figure 2.7), represented by the height ($z_e(t)$) and radius in the orthogonal directions ($r_L(t)$ and $r_R(t)$), was then measured using a caliper. The experiment was repeated with new dry microspheres for another time interval and in this way the time evolution of the advancing front is determined. This procedure was repeated five times in order to have five values of $z_e(t)$), $r_L(t)$ and $r_R(t)$ for each of the six times reported in Figure 2.7. The experimental error for the imbibition

measurement is shown also. Errors were mainly due to the uncertainty of the dynamic viscosity (+/- 7%), and repeatability and uncertainty in the length measurement of the wet region (+/- 0.7mm). The latter absolute error is the reason why vertical error bars at earlier times are larger.

2.5 Results and further discussion

This section compares the theoretical predictions, equations (2.11) and (2.12), for imbibition from a point source in a semi-infinite domain to the results of our experiments and FEM simulations. To plot the theoretical curve in Figure 2.7, the capillary pressure is estimated according to the 1-D capillary rise measurement described above.

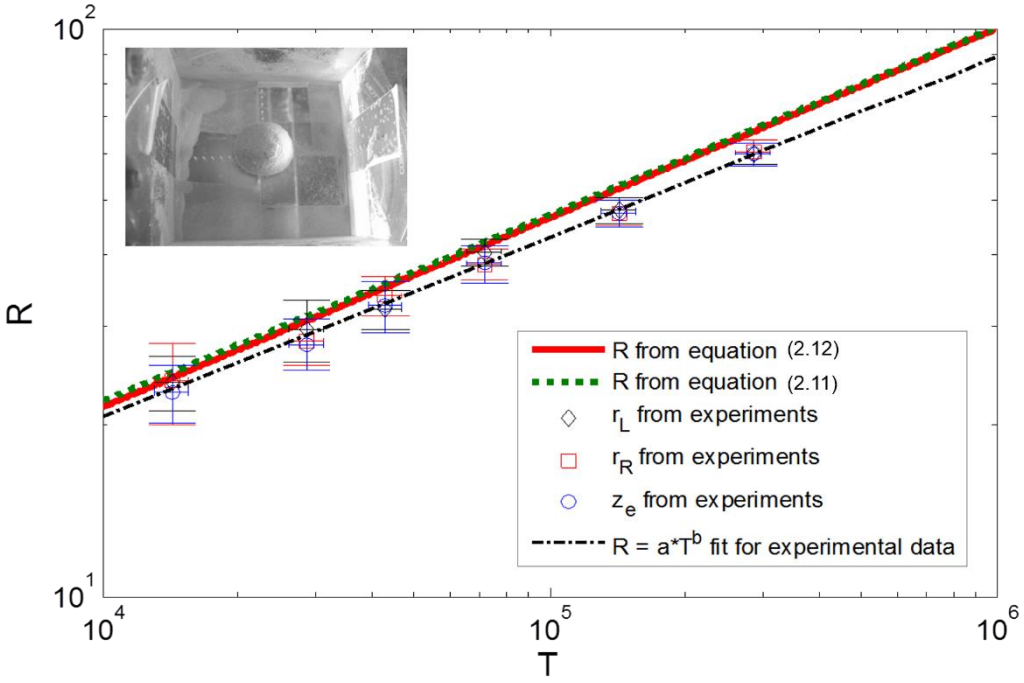

Figure 2.7 Non-dimensionalized size of wet area as a function of time. The top left inset shows the container filled with wetted glass microspheres, after suddenly pouring the dry sand out of the container, as described in the experimental section.

The experimental non-dimensional results of position of the front as a function of time are plotted in Figure 2.7. Three distinct measurements of the front position (r_L, r_R, z_e), as described in the experimental section, are displayed in Figure 2.7. We chose not to measure data points at times shorter than one minute because the measurements involve turning the box upside down so that the dry sand falls away from the wetted region, which is an operation that takes about 5 seconds. For that reason, data points at shorter times have larger uncertainty than at later times, as can be seen with the vertical error bars. The measurements are non-dimensionalized according to equation (2.14), assuming that the contact area between the radial source and the porous medium equals the contact area in the experiments, *i.e.* the cross-section of a tube with diameter d. Therefore, $r_s = d/2\sqrt{2}$. The data points for R_L, R_R and R_Z overlap at every measured time, suggesting that the front spreads as a hemisphere. The average values fitted on the measurements using the power law $R = a \cdot T^b$ are a = 1.03 and b = 0.32, respectively. Both the experimental exponent and prefactor are well within 5% of the predicted value of 1 and 1/3 of the power law found analytically in equation (2.14), respectively, which confirms the cubic root law. The measured slope might be slightly smaller than 1/3 because gravity is not totally negligible for the larger measured radii. Figure 2.7 also compares the full solution of the imbibition problem, equation (2.11), with its approximation for long times, equation (2.12). Results of the comparison show that the relative error between the full solution and its approximation for long times becomes less than 10% for $T > 120$, which in our experiment

corresponds to $t > 0.4$ s.

The simulation results from COMSOL are compared with theoretical analysis in Figure 2.8. The convergence of radial size in different directions are best exemplified by the inlet in Figure 2.8, as the value of ratio z_s/r_s converges to 1 quickly in the simulation. We also compare our results with the Lucas-Washburn Law in Figure 2.8, and a clear deviation from the classical imbibition law is observed.

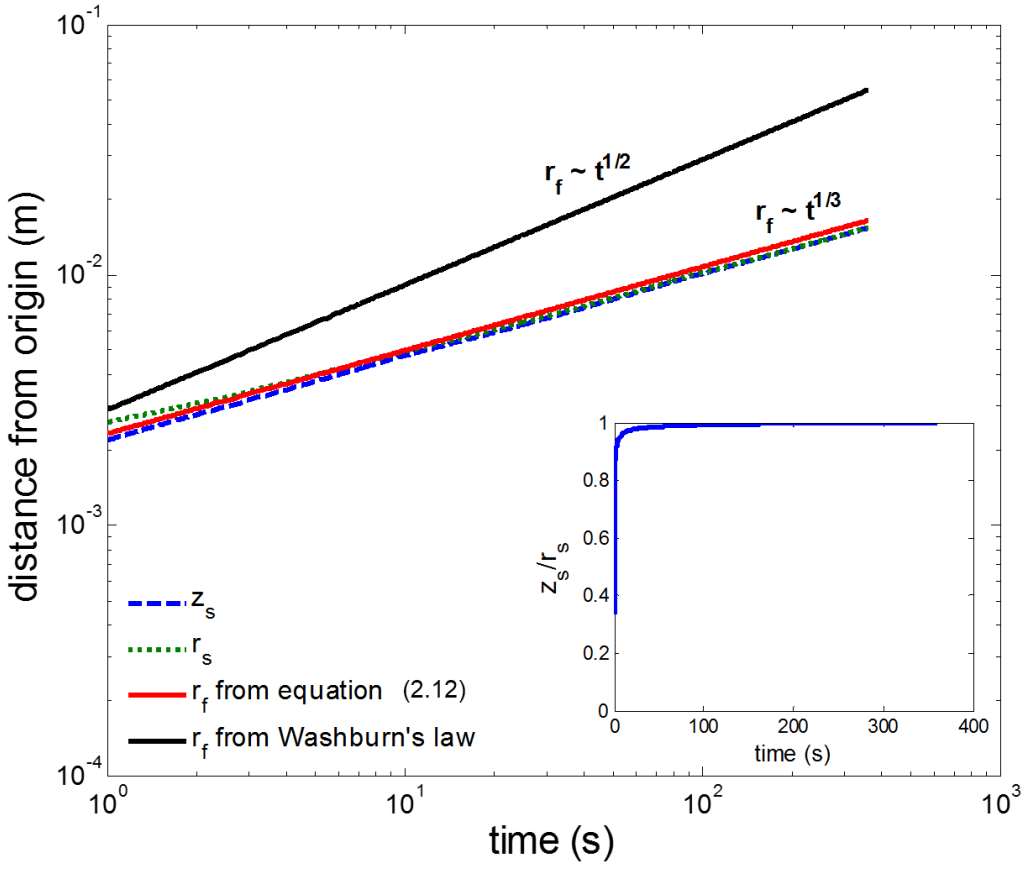

Figure 2.8 Comparison between theoretical results and numerical results. The inset compares the radii in different direction, and its convergence to 1 confirms assumption of spherical wetting area.

Since $r_f \sim t^{1/3}$, the radial velocity of the wetting front goes as $\dot{r}_f \sim t^{2/3}$, which

means the advancing of wetting front slows down as t becomes large. This is conceivable since the pressure gradient, which is the driven force of advancing of wetting front, decreases as r_f increases. The radial velocity of the wetting front obtained from simulation is plotted against theoretical prediction in Figure 2.9a. Small discontinuities are seen at times corresponding to remeshing operations, but the general agreement is very good. Even though the advancing of r_f decelerates, flow rate q remains constant with time as indicated by equation (2.13) and confirmed in Figure 2.9b, because the wet/dry area also increases with time to compensate the deceleration of wetting front.

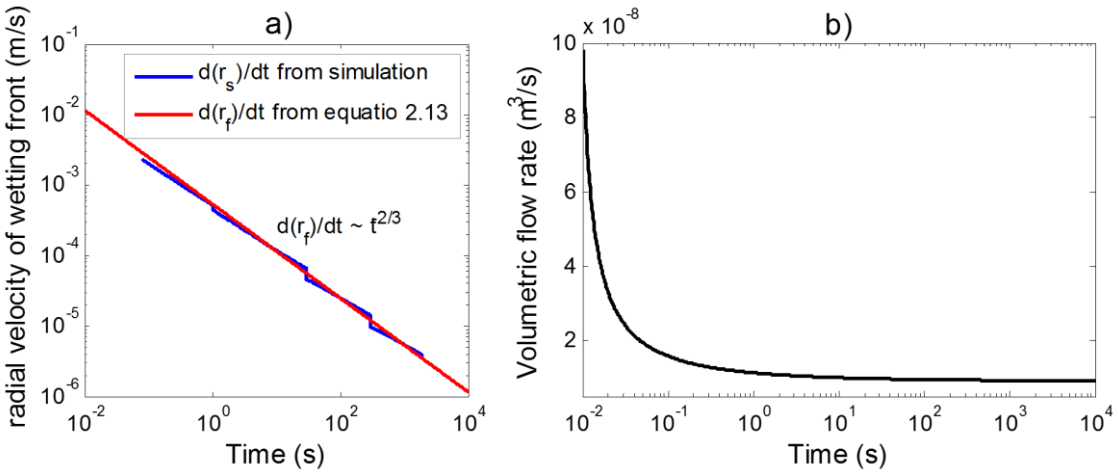

Figure 2.9 a) radial velocity of wetting front; b) flow rate calculated from equation (2.13)

However, when the geometry is reduced from 3D to 2D, the decreasing pressure gradient still holds, the advancing speed still decelerates, but the flow rate is no longer a steady value. The radial imbibition in planar geometry is discussed briefly as a comparison to the 3D radial imbibition law.

The basic equations are still Darcy's law (2.1) with (2.2) and the definition of

capillary pressure in porous media (2.6), but in 2D geometry the flow rate is different as the surface area of wetting front changes:

$$q(t) = \pi r_f \frac{dr_f}{dr} \tag{2.17}$$

So the pressure gradient can be related to radial velocity of wetting front:

$$-\frac{dp}{dr} = \frac{\mu q(t)}{\pi r k} \tag{2.18}$$

With the spatial integration from source $r = r_s$ to the wetting front $r = r_f(t)$:

$$p_c = \frac{\mu q(t)}{\pi k}\left(\ln r_f - \ln r_s\right) \tag{2.19}$$

Plugging flow rate (2.17) into (2.19):

$$r_f \frac{dr_f}{dt}\left(\ln r_f - \ln r_s\right) = \frac{k p_c}{\mu} \tag{2.20}$$

Equation (2.20) can be rewritten to:

$$\frac{r_f}{r_s}\frac{d\, r_f/r_s}{dt}\left(\ln \frac{r_f}{r_s}\right) = \frac{k p_c}{\mu r_s^2} \tag{2.21}$$

With the time integration from starting point $r_f = r_s$ to current time t:

$$\frac{k p_c}{\mu r_s^2} t = \frac{1}{4}\left(\left(\frac{r_f}{r_s}\right)^2 \left(2 \ln \frac{r_f}{r_s} - 1\right) + 1\right) \tag{2.22}$$

Plugging capillary pressure (2.6) into (2.22):

$$\frac{8\gamma \cos\theta\, k}{\mu r_s^2 r_m} t = \left(\frac{r_f}{r_s}\right)^2 \left(2 \ln \frac{r_f}{r_s} - 1\right) + 1 \tag{2.23}$$

This is the implicit solution for radius of wetting front, and it is not easy to discern the inherent law with respect to time as compared to cubic law in (2.12). The radius versus time is solved in a MATLAB code and is plotted in Figure 2.10 for better understanding. As seen in the figure, the wetting front cannot be described by a simple and elegant rule with respect to time.

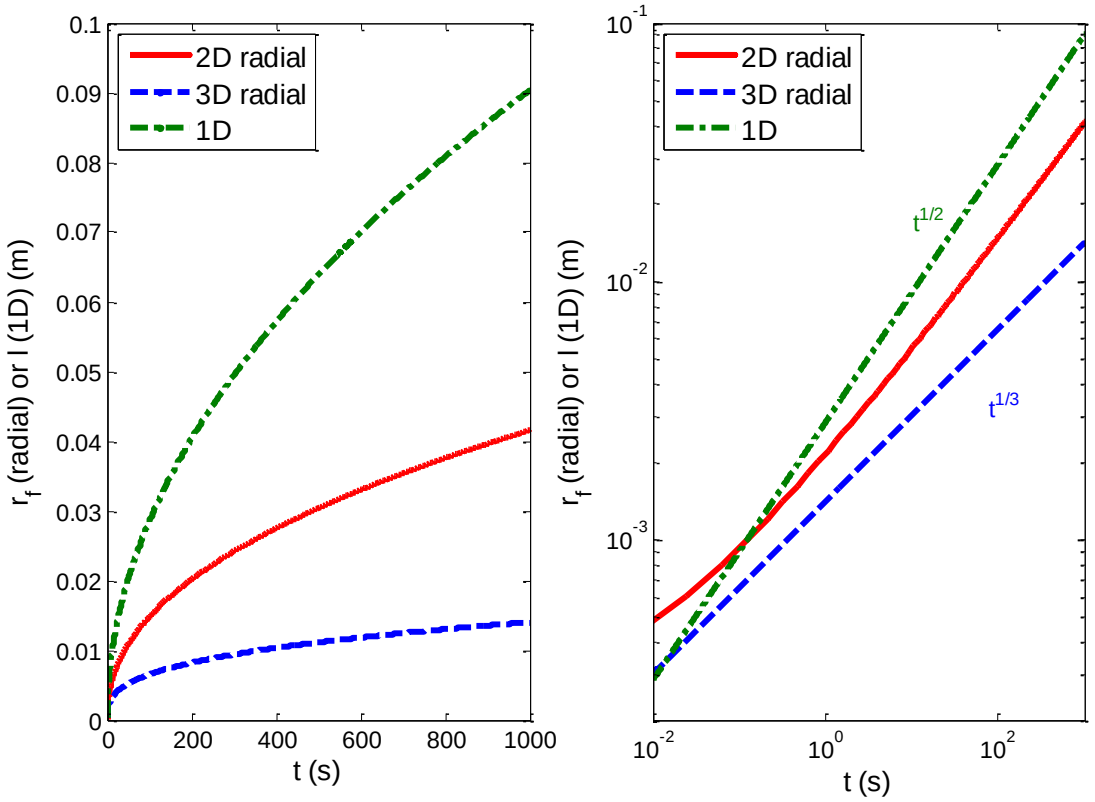

Figure 2.10 r_f or l of wetted area in terms of time in 1D, 2D radial and 3D radial imbibition. Left column is plotted in linear scale, right column is plotted in log scale.

In conclusion, the imbibition process from a point source into a porous material of semi-infinite extent has been studied theoretically, numerically and experimentally. These three approaches are in good agreement, and show that when gravity is negligible compared to the capillary pressure, the wetting front conserves a hemispherical shape with radius evolving with time as $r \sim t^{1/3}$. This result complements known one- and two-dimensional imbibition results. If we neglect the initial transitional stage, the flow rate of the imbibition process tends to be a time-independent constant, which is similar to the discoveries in literature [7]. This work also presents the long-time solution for a series of

PDEs in 3D spherical geometry, *i.e.* $\mathbf{v} = -D\nabla p$ and $\nabla^2 p = 0$. The equation states that velocity of the interface is proportional to the pressure gradient from interface to source. The pressure distribution, however, is governed by the Laplace equation. As the interface moving forward, the velocity of the interface decreases because the distance between interface and source increases, thus the gradient decreases. Darcy's law is essentially equivalent to Fick's law in diffusion, Fourier's law in thermal conduction and Ohm's law in electrical network, so the results could be expected to be applied to relevant problems.

Chapter 3.Buckling of Elastic Beam under Lateral Constraints

3.1 Introduction to beam buckling

A straight elastic beam can maintain its straightness under compressive stress until a critical value is reached, then the beam becomes sinuous undergoing a process called buckling. The buckling beam without lateral constraint has been analyzed systematically [34], and a brief review will be presented in this section.

At the small strain and moderate rotation which is usually the case at the onset of buckling, the deformation of beam can be explained by Euler beam theory:

$$EI\frac{\partial^4 y}{\partial x^4} + P\frac{\partial^2 y}{\partial x^2} = 0 \tag{3.1}$$

where y denotes the lateral displacement, x lies in the original beam direction (ranging from 0 to length L_0), P the applied compressive force, E Young's modulus and I second moment of area of beam. Equation (3.1) has the general solution in the following form:

$$y = A\sin kx + B\cos kx + Cx + D \tag{3.2}$$

with $k^2 = P/EI$. With appropriate boundary conditions, we can obtain the exact solutions for equation (3.1). The simplest boundary conditions are free-rotating ends:

$$\begin{aligned} y(0) = y"(0) = 0 \\ y(L) = y"(L_0) = 0 \end{aligned} \tag{3.3}$$

The solution will be:

$$B = C = D = 0, \qquad \sin kL_0 = 0 \tag{3.4}$$

Which means kL_0 has to be specific values:

$$kL_0 = n\pi \tag{3.5}$$

Therefore the buckling shape is:

$$y = A \sin \frac{n\pi}{L_0} x \tag{3.6}$$

Although the exact value of A is yet to be determined, equation (3.6) provides us useful information about the buckling shape. First few buckling modes from equation (3.6) corresponding to n = 1, 2, 3 are illustrated in the following figure:

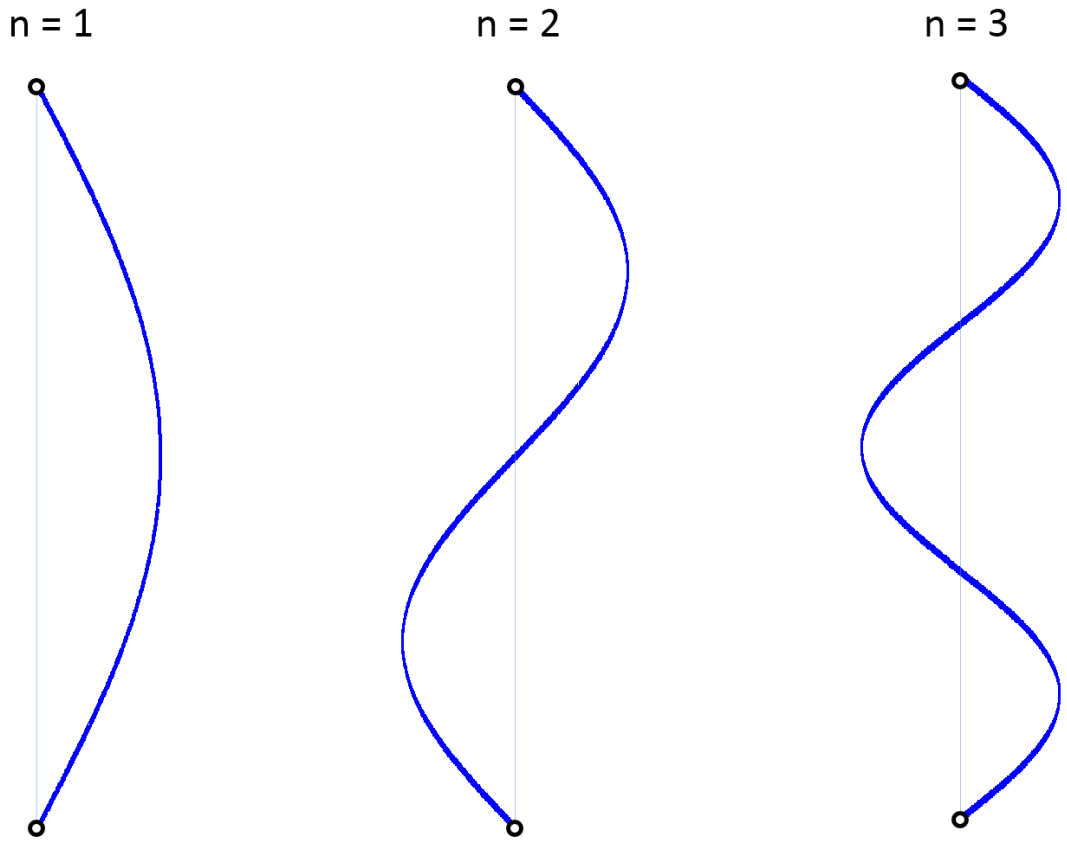

Figure 3.1 First, second and third buckling mode for hinged beam without lateral constraints

Each value of n is corresponding to compressive force $P = \frac{n^2\pi^2 EI}{{L_0}^2}$. The smallest n, *i.e.* 1, is corresponding to compressive force $P = \frac{\pi^2 EI}{{L_0}^2}$, which is usually called critical force P_{cr}. When compressive force is smaller than the critical force, the beam can maintain its original straightness. When the compressive force reaches the critical force, small perturbation can cause large lateral displacement as described by (3.6).

While buckling beams without lateral constraints have been analyzed systematically, Adan, *et al.* [35] have shown numerically and experimentally that buckling beams under a lateral constraint exhibit bifurcation modes that are distinct from that without lateral constraints. Under two parallel lateral constraints, Chai has shown that the buckling of a simple-supported beam exhibits new categories of buckling modes, as well as different transition behaviors between these modes, compared with the one-side constraint [36, 37]. Recently researchers have also explored the effects of elastic constraints on the buckling process of elastic beam. The normal forces exerted on the beam can be characterized using the stiffness of the elastic constraints K. Consequently an additional term is added to the equation (3.1) in order to account for the normal force from constraints:

$$EI\frac{\partial^4 y}{\partial s^4} + P\frac{\partial^2 y}{\partial s^2} + Ky = 0 \tag{3.7}$$

The shape of beam at the onset of buckling can be finely tuned into two dimensional shape or three dimensional shape by adjusting the value of K [38].

3.2 Two dimensional beam buckling under lateral constraints

Although beam buckling under lateral constraint appears to be a pure mechanics problem, it could also provide interesting insights for morphogenesis in natural and engineered systems [39, 40]. Recently, Marvi and Hu [41] showed that when a snake crawls between two parallel walls, its body takes an unique rectangular wave-like shape which also depends on the wall spacing.

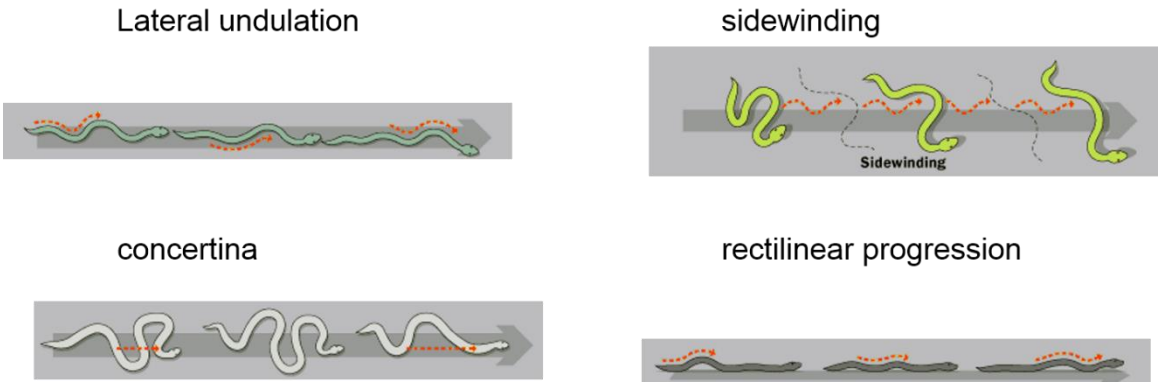

Figure 3.2 Four conventional modes for snake locomotion

In general, a snake usually moves forward in four ways: slithering by lateral undulation of the body, rectilinear progression by unilateral contraction/extension of their belly, concertina-like motion by folding the body as the pleats of an accordion and sidewinding motion by throwing the body into a series of helices [42, 43]. Lateral undulation is the most common way for snakes to move forward, in which the sinusoidal-like lateral bending of body is propagated from head to tail. If a snake is forced to crawl through crevices between rocks, its body may be required to conform to the shape of the narrow curvy “valley”. However, when the snake crawls through two parallel constraints,

the rectangular wave-like profile, such as the morphology in Figure 3.8, has not yet received a theoretical explanation although it has been documented for a long time.

Inspired by the fact that the sinusoidal morphology of a constrained crawling snake is analogous to a buckled beam, insights may be obtained by studying elastic beam buckling under two parallel lateral constraints, in particular the formation of rectangular wave upon contact. A theoretical framework is established in this section, and the transition between different modes is obtained as a function of axial strain and wall spacing. The theory is compared with finite element simulations. The buckling profiles from theory and simulation are then qualitatively related to the characteristics of the crawling snake.

3.2.1 Theoretical Model for buckling beam and transition between different buckling modes

The schematic of two-dimensional model with linear elastic response is shown in Figure 3.3, which is inspired by results of Chai [36, 37] and is used to represent the axial skeleton of a snake [44, 45]. An elastic beam of length L_0 and radius r is initially placed in the middle of two parallel walls. The beam and walls are placed on the same horizontal plane. Both ends are allowed to move freely in the y-direction, yet their rotational degree of freedom is constrained, which resembles the snake crawling behavior. To apply axial compression, the left end of beam is fixed in x direction and the right end is pushed inward by a displacement of ΔL. The wall is assumed rigid and kept fixed throughout, and contact

friction is neglected in this model.

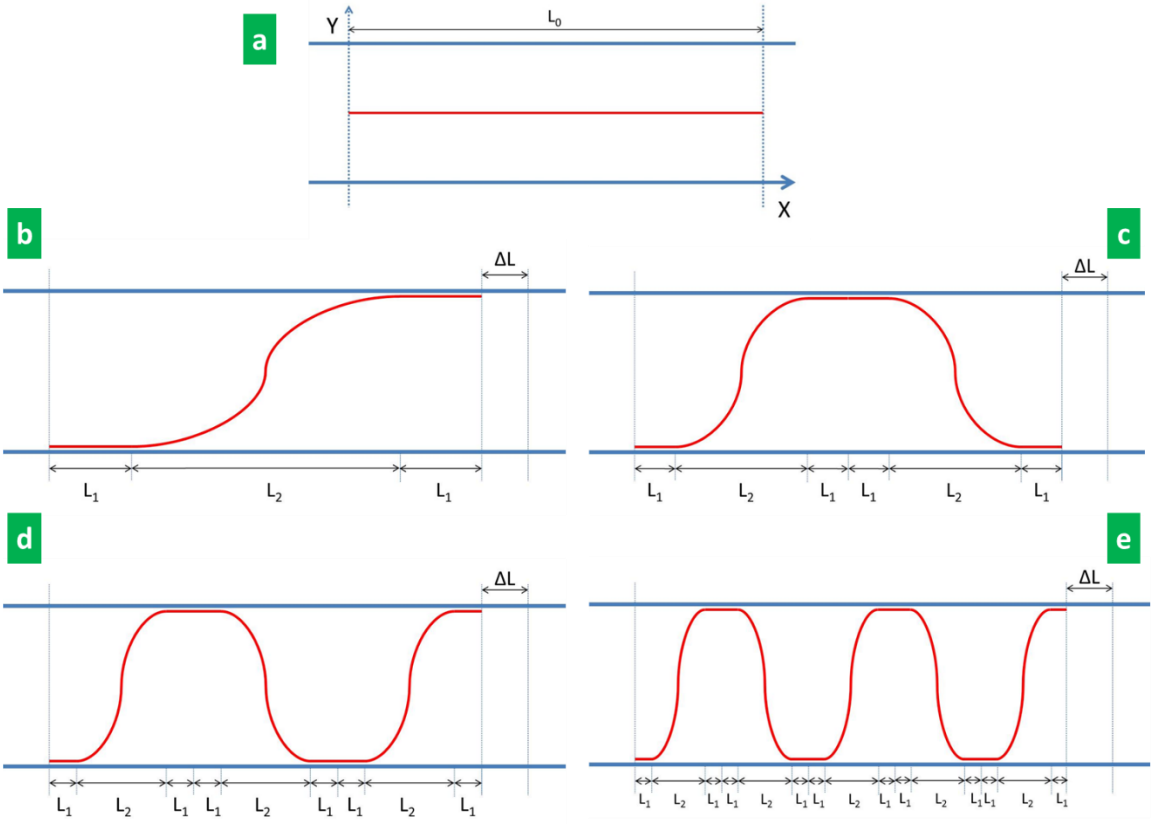

Figure 3.3 Schematic of the theoretical model and the first few buckling modes, with beam in red and wall in dark blue. (a) Shape of the undeformed beam; (b) buckling mode 1 of the deformed beam; (c) buckling mode 2 of the deformed beam; (d) buckling mode 3 of the deformed beam and (d) buckling mode 5 of the deformed beam.

When the compressive strain exceeds critical strain, the beam buckles and the buckling amplitude increases with ΔL, until the deformed beam makes contact with the wall. The deformed profile is assumed to be symmetric. This becomes the bifurcation mode 1, Figure 3.3(b). The shape of mode 1 consists of three parts [36, 37, 46]: straight section L_1, curved section (with projected length L_2) and straight section L_1. With the further increase of ΔL, the straight sections elongate and their length will be determined in the

following section through strain energy minimization. When the straight section becomes too long, it loses stability and then the entire beam bifurcates into the next mode, illustrated as mode 2 in Figure 3.3(c). Mode 2 consists of two curved sections with straight sections in between (length $2L_1$) and at the ends (length L_1 each). With continued compression, the straight section of mode 2 may become unstable and mode 2 bifurcates to mode 3, Figure 3.3(d), and so on to higher modes, Figure 3.3(e) and beyond, with subsequent compression. Note that as the modes shift, the beam ends may jump up or down, and such a boundary condition was not explored in previous studies.

To analyze different buckling shape, the exact shape should be solved first. Euler beam theory (equation (3.1)) is again the starting point. For beam in the narrow channels, the deflection and axial strain in the beam is relative small, so Euler beam equation is still valid in our cases for the curved sections since there is no contact between beam and constrains. Force and moment from contact are only exerted on the end point of curved section (shown in Figure 3.4). With straight parts of beam touching the constraints, a new set of boundary conditions should be used. Taking mode 1 in Figure 3.3 as an example, boundary conditions of curved section at two ends $x = L_1$ and $x = L_1 + L_2$ are (we only consider geometrical boundary conditions, force and moment at the boundaries are not considered):

$$y(L_1) = y'(L_1) = y''(L_1) = 0 \tag{3.8}$$

$$y(L_1 + L_2) = A, \qquad y'(L_1 + L_2) = y''(L_1 + L_2) = 0$$

Together with general solution (3.2), the contour shape of this curved section is:

$$y = 2A\frac{x - L_1}{L_2} - \frac{A}{\pi}\sin\left(\frac{2\pi}{L_2}(x - L_1)\right) \tag{3.9}$$

where A is denoted as the wave amplitude, and $2A = d$ is the wall spacing. The above shape is consistent with finite element simulation results. For this case, the constraint of coefficient k in equation (3.1) satisfies:

$$\frac{kL_2}{2\pi} = 1 \tag{3.10}$$

The shape of curved sections of other modes can be described in a similar way as equation (3.9), except that the value of L_2 is different in each mode. In other words, once L_1 and L_2 are determined (see below), the shape function of deformed beam is obtained.

The strain energy of the beam consists of two parts in this model: bending energy which is assumed to exist only in the curved sections and compressing energy which is assumed to be uniform along the beam, and consistent with finite element simulation. Based on displacement in equation (3.9), the bending energy of the curved segment is calculated as:

$$E_{bending} = \frac{EI}{2}\int_L \frac{|y''|^2}{(1 + y'^2)^3}\,dx \tag{3.11}$$

Denoting the total length of the deformed beam as L_{deformed} (which can be readily calculated using equation (3.9)), the axial strain ε is:

$$\varepsilon = \frac{L_{deformed} - L_0}{L_0} \tag{3.12}$$

And hence the compressing energy along the beam is:

$$E_{compression} = \frac{1}{2}\varepsilon^2 EaL_{deformed} \tag{3.13}$$

where a is the area of cross section for the beam.

With increasing load ΔL, the beam morphology varies. Within a particular buckling mode, the beam deforms according to minimization of the total strain energy ($E_{\text{bending}} + E_{\text{compression}}$). This principle, along with the geometrical constraint:

$$L_{projection} + \Delta L = L_0 \tag{3.14}$$

can be employed to deduce L_1 and L_2 for a given ΔL and known mode. The beam stays at the current buckling mode until one of straight sections gets buckled according to reference [36]:

$$\frac{kS}{2\pi} = 1 \tag{3.15}$$

where S in the equation above is the length of a straight section. This determines the transition point (critical ΔL) from one bifurcation mode to the next.

3.2.2 Numerical Analysis for the buckling beam under constraints

In order to verify the key assumptions employed in theoretical analysis as well as validate the model, a two dimensional finite element model is established to simulate the beam buckling process under parallel constraints, using commercial finite element package ABAQUS. Boundary conditions of walls and the beam are stated previously. We started this research with a three dimensional finite element model, which was found to be

consistent with the two dimensional model with these specific geometrical constraints. So two dimensional models were employed throughout the paper. The beam is meshed by 100 2D linear beam elements, and the wall is modelled by 2D linear discrete rigid elements. The mesh density is validated by mesh convergence studies.

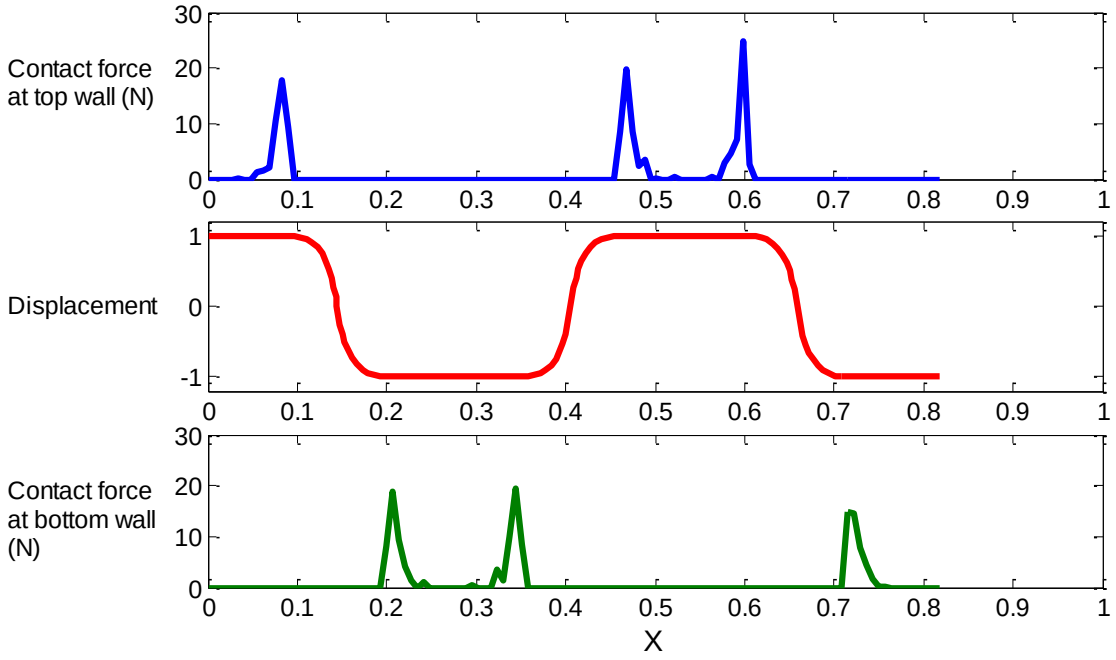

Figure 3.4 Shape of buckling beam in the FEM simulation at mode 3 (walls are not shown) and normal contact forces at top/bottom wall. The data are normalized by original length L_0 in x direction; displacements are normalized by amplitude A

According to the contact theory, when there is a line contact between beam and wall, normal contact forces do not distribute uniformly throughout the contact section, but rather concentrate on both ends of the contact section (seen in Figure 3.4). This phenomenon is used to differentiate the line contact section from curved section in the simulation results, and thus the values of L_1 and L_2 can be determined in the simulation results, and compared with the theoretical predictions.

3.2.3 Comparison between theoretical analysis and numerical analysis

According to our model, the projected length of the curved section, L_2, is an important parameter determining not only the shape of buckled beam, but also the bending energy of the system. We didn't calculate L_1 because once L_2 is determined, the total length of L_1 is L_0 - ΔL - nL_2 where n indicate the buckling mode, while values for individual L_1 vary along the beam because of the asymmetries described in following section. Values of L_2 from theoretic analysis and simulation are compared at different nominal strain values ($\Delta L/L_0$) in Figure 3.5, with representative geometrical values L_0/d = 10, d/r = 10. As illustrated in Figure 3.3, the beam undergoes different buckling modes as the compression proceeds (the modes are separated by vertical dot lines in Figure 3.5, according to our theoretic model). Within a given buckling mode, L_2 decreases as $\Delta L/L_0$ increases, implying that the strain energy of the beam increases with compression. Whereas when the mode transition occurs, L_2 suddenly increases as a result of relieving compressive energy.

It should be remarked that mode 4 is not sketched in Figure 3.3, and this mode is rarely observed in reality because when mode 3 reaches critical, it is more natural for its two straight sections to buckle simultaneously and become mode 5. This is confirmed by FEM simulation results in Figure 3.5.

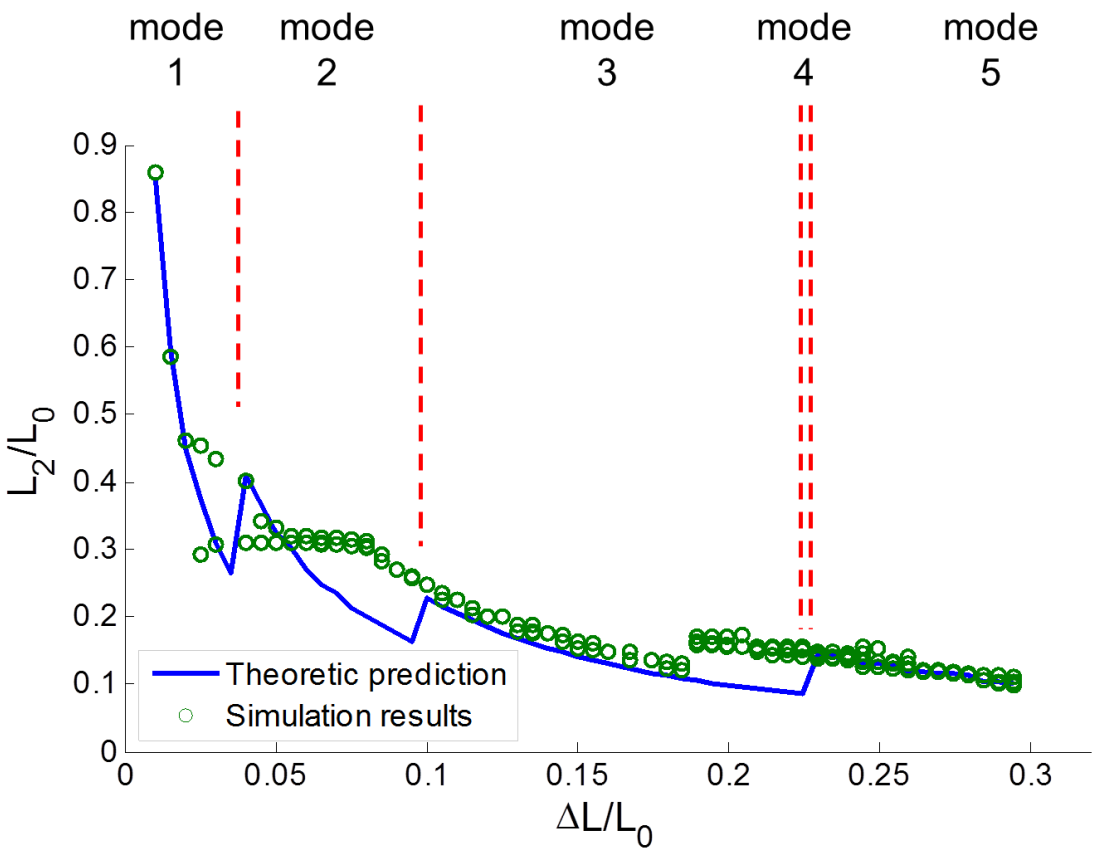

Figure 3.5 L_2 for different displacement ΔL, all data are normalized by original length L_0. Geometrical parameters are $L_0/d = 10$ and $d/r = 10$.

The comparison between theoretical model and simulation in Figure 3.5 shows that, while for the most parts the variation trend of L_2 is predicted by model agrees well with FEM simulation, the modal transition points are not consistent, especially for mode 2 and beginning part of mode 5. In FEM simulation, the mode transition (higher order bifurcation) occurs sooner than that in the model, whose reason is analyzed below.

Examination of FEM simulation results reveals that the deformed profiles are often not symmetric, in particular for mode 2 and beginning part of mode 5. As mentioned earlier, the theoretical model is based on the assumption that the buckled beam shape is

symmetric (Figure 3.3). However, when the straight section is redistributed along the beam (while keeping its length fixed) at the instant of modal transition, the total strain energy would remain the same. Using mode 2 as an illustrative example, the relocation of straight sections is illustrated in Figure 3.6, where the various sibling morphologies share identical bending and compressive strain energies.

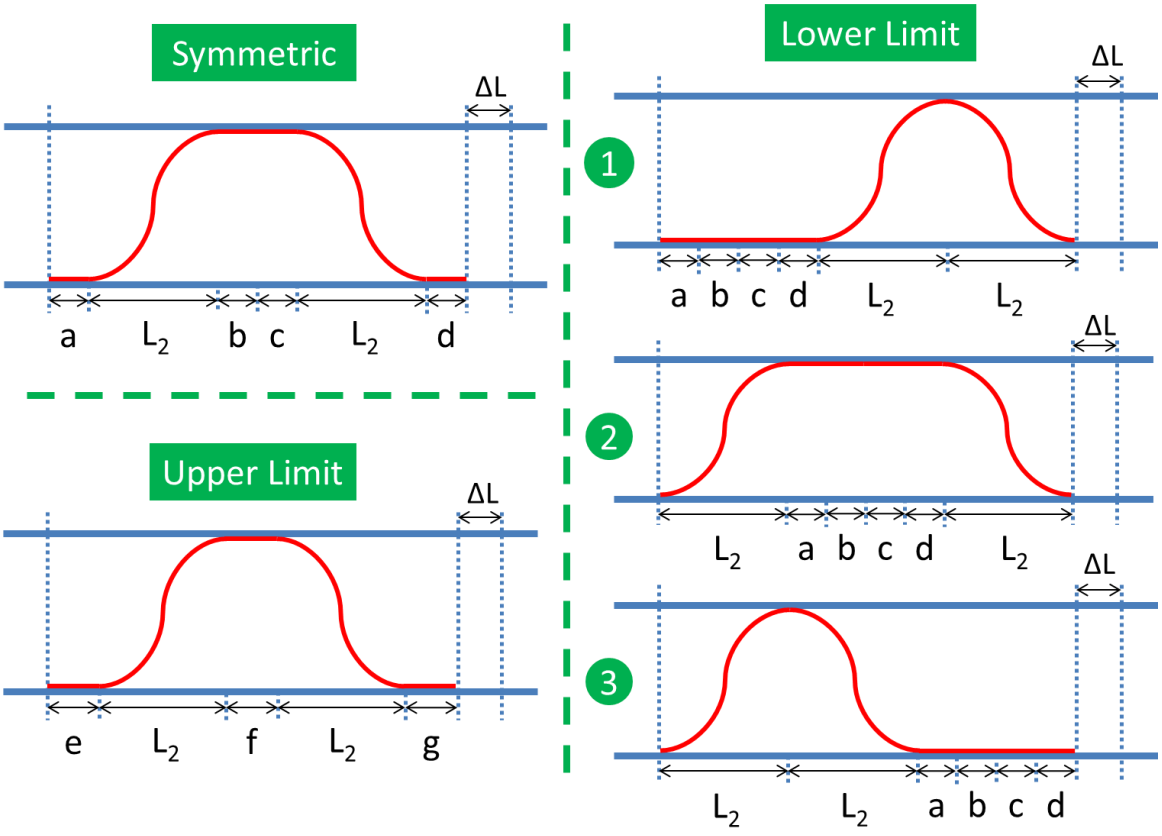

Figure 3.6 Different sibling morphologies for mode 2, symmetrical case, upper limit and lower limit, which affect its transition to the subsequent mode 3 with increasing load.

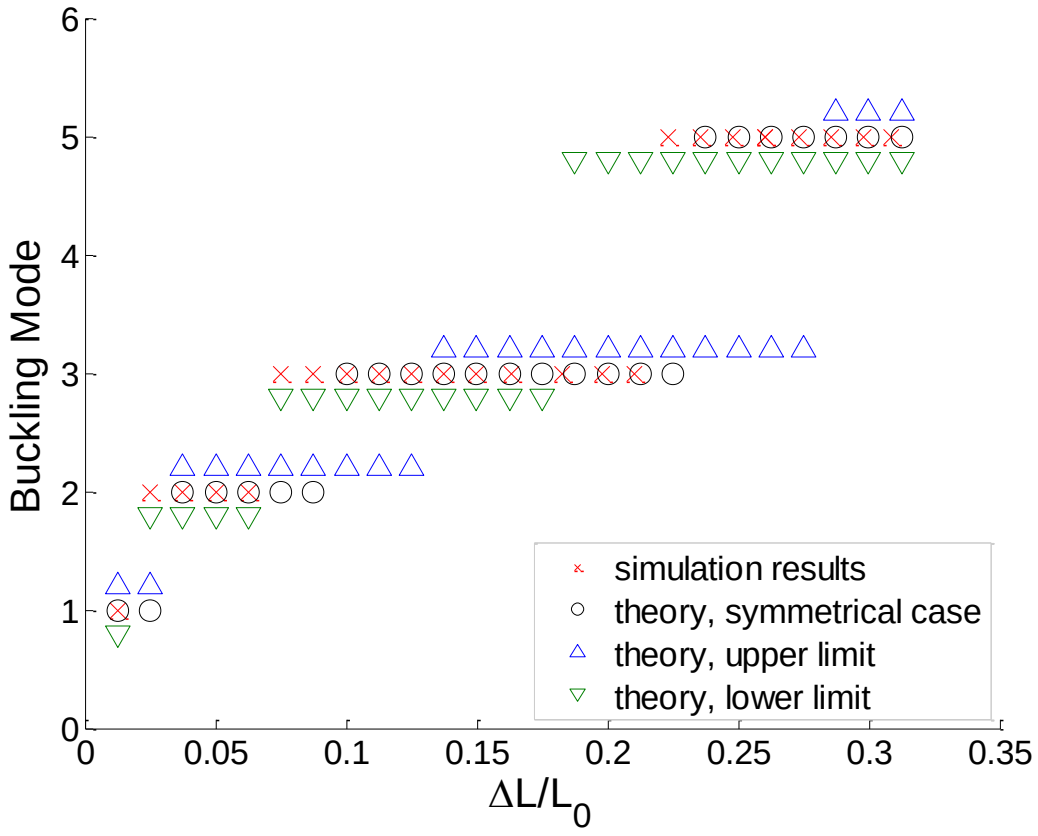

Figure 3.7 Buckling mode map for theoretical analysis and simulation with upper limit and lower limit. Geometrical parameters are $L_0/d = 10$ and $d/r = 10$.

The reshuffle of the straight sections, however, does affect the modal transition point which dictates the instability of the straight section. Such an effect of asymmetry on buckling mode transition was first noted by Chai [36] and then Pocheau and Roman [46], who provided the upper and lower limits for the modal transition. In the present study, Figure 3.6 illustrates the upper limit and lower limit for the transition from mode 2 to mode 3. At a given nominal strain ΔL, the total length of beam in the projection of x direction is $L_0 - \Delta L$, which means that $a + b + c + d + 2L_2 = e + f + g + 2L_2 = L_0 - \Delta L$ for all cases in Figure 3.6. In the symmetric case $a = b = c = d$. For the upper limit case $e = f = g$, so every

straight section is as short as possible which makes its instability the most difficult. For the lower limit, all straight sections merge into a single straight section (there are three possible shapes for lower limit at mode 2), which becomes the easiest to buckle. Although prior theoretical analysis is based on the symmetric model, similar analyses can be carried out for the upper and lower limit cases to obtain the bounds of modal transitions. One expects that the real solution (*e.g.* FEM simulation, which may be sensitive to defects) is within the upper and lower bounds.

Analogous to Chai [36], a buckling mode map (Figure 3.7) is established to predict the modal status at different $\Delta L/L_0$, which includes that from the upper and lower limits, as well as that based on the symmetric assumption. The data points for upper limit and lower limit are slightly shifted vertically in order to differentiate themselves from the data points for symmetric case. In general, the FEM simulation results is indeed bounded by the upper limits and lower limits.

3.2.4 Effect of geometrical parameters and implication for the crawling snake

For a flexible beam with a given nominal strain $\Delta L/L_0$, its morphological profile is determined by the geometrical parameters. For the crawling snake in Figure 3.8, its morphology is rather distinct when the wall spacing is changed. Assuming the snake employs the same nominal strain to crawl forward, Figure 3.9 illustrates the buckling

shapes of beams with different L_0/d at the same $\Delta L/L_0 = 0.2$. The data points are non-dimensionalized by amplitude d in the y direction, and L_0 in the x direction.

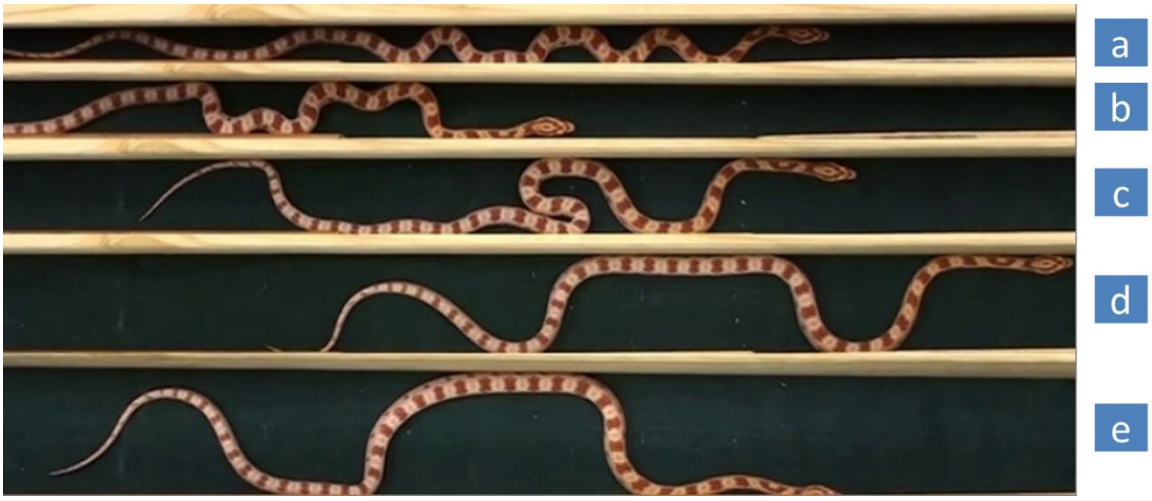

Figure 3.8 Wave-like shape of a snake under parallel lateral constraints on a horizontal plane. The length of the snakes is 61 ± 4 cm; the radius of the snake is 1 cm; the width between constraints is respectively 2, 3, 4, 5, 6 cm from (a–e).

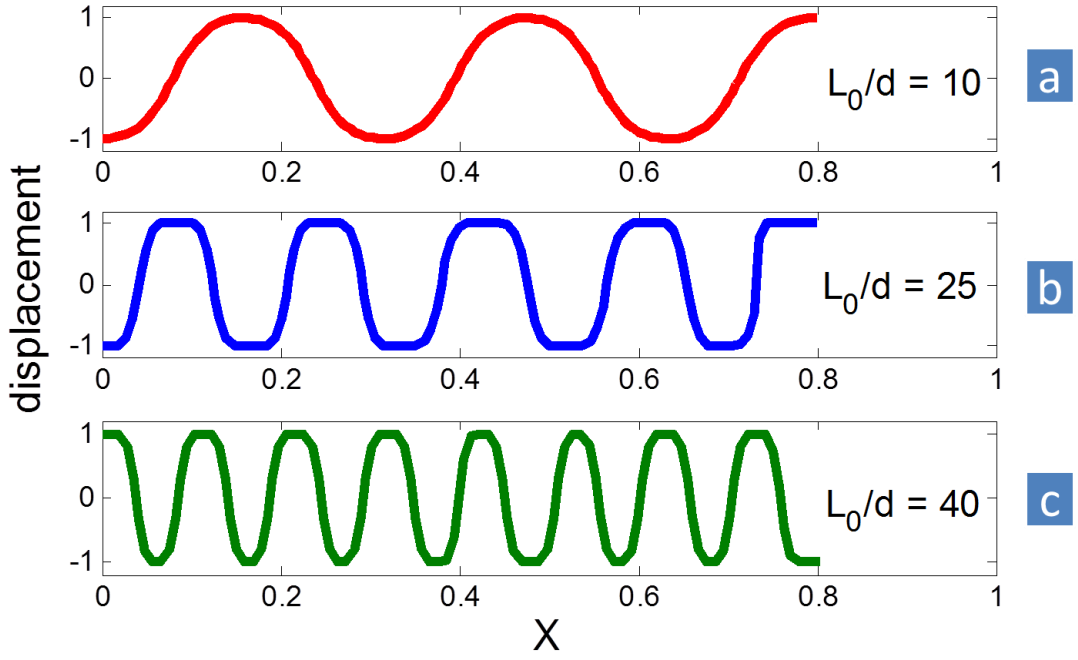

Figure 3.9 Buckling shape of beams with different L_0/d at the same $\Delta L/L_0 = 0.2$. (a, b) show the beam with the same length $L_0/r = 100$, but different $d/r = 10$ and $d/r = 4$; (c) shows the beam with length $L_0/r = 200$ and $d/r = 5$.

In general, as the wall spacing d becomes tighter, the number of curved section increases for beams with the same length at the same nominal strain. This trend is exemplified by 5 curved sections in Figure 3.9(a) and 9 curved sections in Figure 3.9(b), and it is qualitatively consistent with the shape of snake in Figure 3.8. Meanwhile, even with a larger d/r, the beam in Figure 3.9(c) shows more curved sections than Figure 3.9(b) does, because in this case the length of snake increases from L_0/r = 100 to L_0/r = 200. Therefore, the primary dimensionless geometry parameter governing the number of curved section (at a certain nominal strain) is L_0/d. For beams with the same L_0/d, larger d/r postpones the transition between buckling modes.

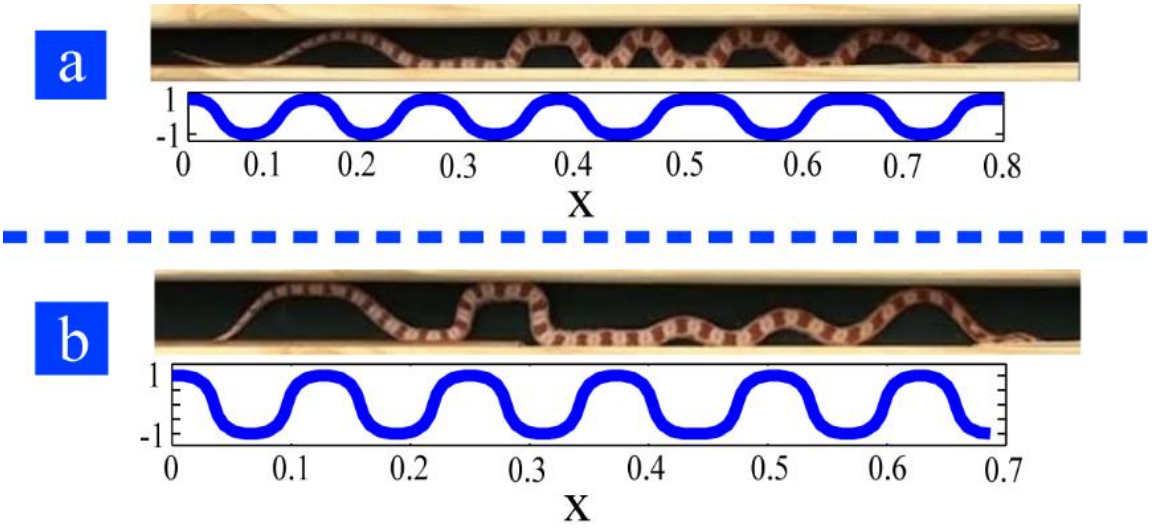

Figure 3.10 Comparison between real snake and simulation results. In (a), 12 curved sections are found in both experiments and simulations, geometrical parameters in simulations are L_0/r = 200, d/r = 7 and L_0/d = 28.6. In (b), 10 curved sections are found in the experiments, which corresponds to the simulation case of 11 curved sections. Geometrical parameters in simulations are L_0/r = 200, d/r = 10 and L_0/d = 20.

By observing the snake between parallel walls of width of 2 cm, *i.e.* snake shown in Figure 3.8(a), we found that the number of curved sections of snake consistently to be

12 during the crawling process (evidence can be seen in the supplement video). The snake between 2 cm walls is characterized by $L_0/d = 30.5$, and it is corresponding to the simulation case $L_0/r = 200$, $d/r = 7$, $L_0/d = 28.6$ in Figure 3.10(a). The head part of snake is not counted because it is much stiffer than its body, so we may take a smaller L_0/d in the simulation. The deformation shape of snake is not uniform because its movement (compressive strain) is not uniform throughout the snake body and the radius of snake varies from head to tail. Nevertheless, the overall number of curved sections is consistent with our theoretical analysis. In Figure 3.10(b), we also compare our model with snake in a channel of width of 3 cm, i.e. the snake shown in Figure 3.8(b). Snake under this circumstance is characterized by $L_0/d = 20.3$, which is analogous to the present model with $L_0/r = 200$, $d/r = 10$, and $L_0/d = 20$. The number of curved sections of snake is consistently 10 during the crawling process, and the present simulation results shows 11 curved sections. This small discrepancy comes from the fact that snake does not follow the concertina pattern strictly during the procession because the snake has more lateral room to employ their normal lateral undulation mode. Moreover, the body of the snake is not uniform. Due to this reason, a large part of snake does not touch the sidewall, as shown in Figure 3.10(b).

3.2.5 Discussion of the 2D confined buckling beam model

This section describes the buckling shape of a linear elastic beam under two lateral constraints. Due to the unique boundary conditions of the beam ends, intriguing buckling

shapes are observed which are different from that reported previously [36, 37]. Our results elucidate the effects of geometrical parameters, $\Delta L/L_0$, L_0/d and d/r, on the buckling shape of the beam. This study could also be of interest to the study of microtubules of cell cytoskeleton and related systems, whose buckling behaviors are constrained by surrounding structures [40, 47].

We then apply our theory to explain why crawling snakes confined in channels adapt the unique wave-like shape, and we explain qualitatively the effect of width between two constraints on the shape of snakes. Previous researches have documented the shape of crawling snakes in concertina mode, and they detected alternative activation of axial muscle on two sides of the snake body during the concertina motion [44, 45]. Unlike the smooth progression of snake in lateral undulation mode, the snake in concertina mode progresses in a two-stage approach (video in the electronic supplementary material): the snake compresses its posterior of body into several bends while keeping anterior fixed, then the snake uses the areas of contact in the posterior as anchor and extend its anterior part in the forward direction. The snake extends its anterior part in a mode similar to lateral undulation, while our theory may effectively apply to the compression stage. For narrow channels such as Figure 3.8(a) and Figure 3.8(b), contracting snake body has to undertake the wave-like buckling shape due to instabilities under lateral constraints as discussed in previous sections. For the wider channels such as Figure 3.8(d) and Figure 3.8(e), snakes have more freedom to employ their normal lateral undulation mode to crawl, even though

the amplitude of undulation is confined by parallel walls [41]. So the shape of crawling snakes between lateral constraints with large width is actually a variation of lateral undulation mode.

Our analysis is based on the assumption that the body of the snake is under compressive stress, which in reality is due to the muscle contraction along the snake body. The snake contracts its axial muscles on two sides of its body alternately in the concertina progression [45], so we take the distributive contractile muscle stress as the effective compressive stress in the snake body, which is consistent with our theoretical and numerical model. Our theory focuses on the linear elastic response of beam/snake, but snake occasionally exhibits interesting shapes shown in Figure 3.8(c) which is a spiral type buckling mode in the plastic regime [48]. We also observed this large deformation pattern in our simulation results, which requires future modeling effort. Furthermore, the friction is essential in the lateral undulation mode as well as in the concertina mode, which adds another complexity to our model. We hope to encompass the friction between snake and walls, as well the friction between snake and horizontal ground in the future studies. The model needs to be refined toward real snake behaviors.

3.3 Three dimensional beam buckling under lateral constraints

Section 3.2 discusses the buckling beam under lateral constraints confined in horizontal plane, and it exhibits buckling shape related to trigonometric functions (seen in

equation (3.2) and (3.9)). The exact solutions, however, are depending on the boundary conditions. Equation (3.3) and (3.8) show two examples of different boundary conditions. But if the elastic beam is not confined in two dimensional plane, a new series of deformation patterns develop as a results of the relaxation of constraints and introduction of new freedom in extra dimension. Buckling beam surrounded by cylindrical constraints in 3D space is usually studied in comparison to two parallel constraints in 2D case, and this configuration is widely used in directional drilling in petroleum industry, where the drilling bit is guided by the surrounding pipe. The most prominent deformation pattern under cylindrical constraints is the spiral shape, or coiled shape, or helical shape, and this shape is described wildly in literature [38, 39, 49-51]. The spiral shape is even observed in the beam embedded in elastic material, and is used to explain the biological shape in cells [40, 47]. Researchers also employed the this model to explain the formation of DNA helix strand [52, 53].

One major difference between the 2D beam and 3D beam is torsion, as there is no torsion in 2D cases while torsion itself is an important source for deformations of 3D beam. And the beam with large torsion is also referred as rod in literatures. When served at both ends of a straight beam as boundary conditions (Figure 3.11), torsion can induce various buckling and post buckling shape, such as spiral shape and localized alpha shape [54, 55] both of which will be discussed in the following chapters.

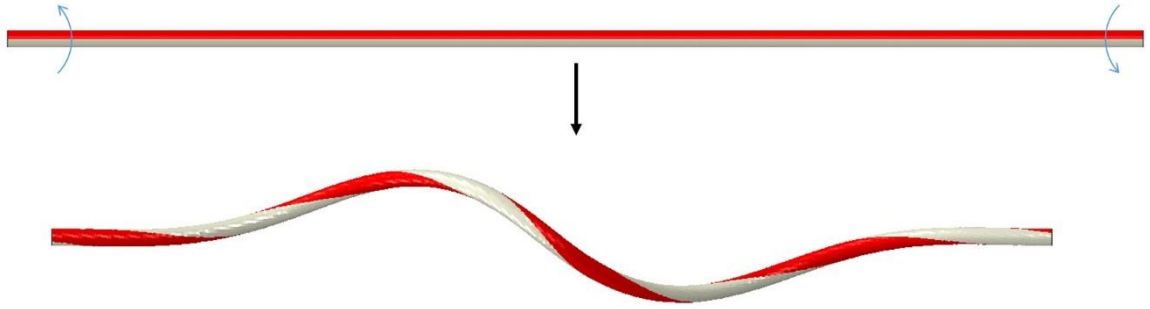

Figure 3.11The deformation of 3D beam due to the application of torsion at both ends. Beam is divided into two strips with different color for better visualization.

Equation (3.1) for 2D and its derivation equation (3.7) don't consider torsion in the beam, so they are not appropriate to describe the 3D deformation therefore. Under this circumstance, Kirchhoff equations are introduced to the solve for the exact shape of beams whose length is much larger than their lateral dimensions. But before that, basic geometrical parameters have to be introduced [53, 56].

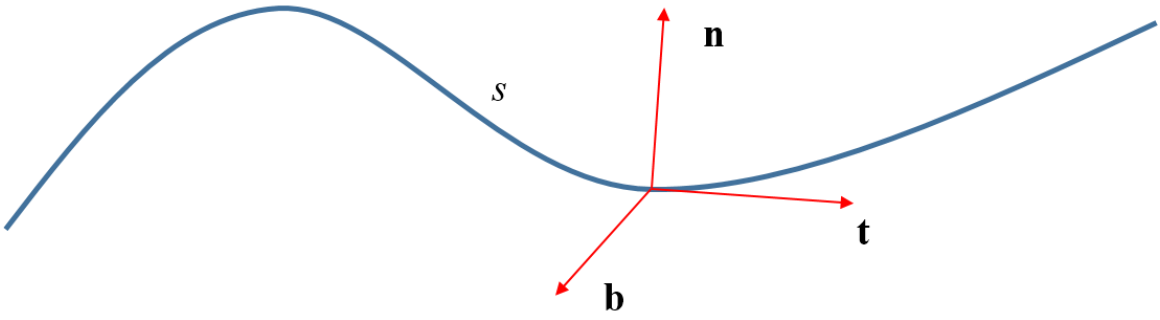

Figure 3.12 Frenet basis at *s* on a curve

A space curve $\mathbf{R}(s, t)$ is defined as the central line of 3D beam, with arc length as *s* and time as *t*. At a certain point *s* on the curve, the Frenet basis (**n**, **b**, **t**) is defined to be the normal, binormal and tangent vectors to the curve as illustrated in Figure 3.12, within which tangent vector is calculated as $\mathbf{t}(s) = \frac{\partial \mathbf{R}}{\partial s}$ and binormal vector defined as $\mathbf{b} = \mathbf{t} \times \mathbf{n}$.

In the Frenet basis, curvature κ at point s is given as $\kappa(s) = \left|\frac{\partial \mathbf{t}}{\partial s}\right|$ without sign.

The Frenet triad forms a right handed orthonormal basis on the space curve **R**. In this system, the unit vectors are related as

$$\begin{aligned} \frac{\partial \mathbf{t}}{\partial s} &= \kappa \mathbf{n} \\ \frac{\partial \mathbf{n}}{\partial \mathrm{s}} &= \tau \mathbf{b} - \kappa \mathbf{t} \\ \frac{\partial \mathbf{b}}{\partial s} &= -\tau \mathbf{n} \end{aligned} \tag{3.16}$$

within which τ represents torsion, the amount of rotation around the tangent **t**. This set of coupled equations are called as Frenet-Serret equations. We observe that once torsion τ and curvature κ are determined, the Frenet triad (**n**, **b**, **t**) can be obtained uniquely in the Frenet-Serret equation, and the curve **R** could be reconstructed by integrating the tangent vector **t** along curve *s*.

The local basis vectors ($\mathbf{e}_1$, $\mathbf{e}_2$, $\mathbf{e}_3$) on the curve is defined on the cross section of one point. Unit tangent vector **t** coincides with vector $\mathbf{e}_3$. The derivatives of triad ($\mathbf{e}_1$, $\mathbf{e}_2$, $\mathbf{e}_3$) with respect to arc length *s* and time *t* in local basis form twist vector $\boldsymbol{\omega}(s,t) = \omega_1 \mathbf{e}_1 + \omega_2 \mathbf{e}_2 + \omega_3 \mathbf{e}_3$ and spin vector $\boldsymbol{\eta}(s,t) = \eta_1 \mathbf{e}_1 + \eta_2 \mathbf{e}_2 + \eta_3 \mathbf{e}_3$, defined as:

$$\begin{aligned} \frac{\partial \mathbf{e}_i}{\partial s} &= \boldsymbol{\omega} \times \mathbf{e}_i \\ \frac{\partial \mathbf{e}_i}{\partial t} &= \boldsymbol{\eta} \times \mathbf{e}_i \end{aligned} \tag{3.17}$$

Under static cases where derivatives with respect to time, *i.e.* η, are neglected, Kirchhoff equations state the conservation of linear and angular momentum for the central line of beam in the absence of external body force:

$$\frac{\partial \mathbf{F}}{\partial s} = 0 \tag{3.18}$$

$$\frac{\partial \mathbf{M}}{\partial s} + \mathbf{e}_3 \times \mathbf{F} = 0 \tag{3.19}$$

where **F** and **M** indicate the total force and total moment exerted on the beam respectively. Torque **M** is related to twist vector **ω** in the following equation:

$$\mathbf{M} = EI_1\omega_1\mathbf{e}_1 + EI_2\omega_2\mathbf{e}_2 + GJ\omega_3\mathbf{e}_3 \tag{3.20}$$

where E represents Young's modulus, G shear modulus, I_1, I_2 and J area moments of inertia for the beam cross section. For the circular cross section, I_1 is equal to I_2,

$$I = I_1 = I_2 = \frac{J}{2} = \frac{\pi r^4}{4} \tag{3.21}$$

with r being the radius of the cross section. Equation (3.18), (3.19) and (3.20) are called Kirchhoff equations for the elastic long beams. Once solved, the solution provides the locations and postures for the whole beam. Kirchhoff equation is equivalent to Euler equation for the motion of rigid body about a fixed point under gravity as many researchers realized long time ago [53, 56].

Closed analytical solutions for the vector equation system are generally troublesome to obtain, but some useful observations from Kirchhoff equations can be made with insights from Euler equations. Some first integrals of the Kirchhoff equations can be derived, first of which states that the torsion is constant along the beam. This is an important implication for the calculation of strain energy in the following content [53, 56, 57].

$$M_3' = 0 \tag{3.22}$$

The strain energy in the three dimensional beam consists of four components:

bending energy, torsion energy, stretching energy and shear energy.

$$E_{total} = E_{bending} + E_{torsion} + E_{stretching} + E_{shear} \tag{3.23}$$

For long and slender elastic beam in the linear deformation regime, the shear energy and stretching energy can be neglected compared to bending energy and torsion energy [58]. Actually for two dimensional beam, the stretching/compressing energy is also a minor part compared to the bending energy. The three dimensional bending energy is a natural extension from the two dimensional case, given the fact that there is extra dimension in the shape. The torsion, however, was never considered in the two dimensional shape as there is no freedom for torsion on a beam constrained in a plane. The calculation of bending energy and torsion energy will be detailed in the following section considering the specific shape at each stage.

3.3.1 Transition from 2D shape to 3D shape

Similar to the two dimensional model in section 3.2, a three dimensional FEM model was constructed in ABAQUS with beam (initial straight length L_0, radius r, diameter d_b) on the central axis of cylinder with diameter d_t. One end of the beam is fixed without any displacement or rotation; the other end is pressed with displacement ΔL in the original beam direction without any rotation. The friction between beam and constraints is not considered in our simulation. The beam is meshed by 100 2-node three dimensional linear beam elements, and the wall is model by linear discrete rigid elements. The mesh density

is validated by mesh convergence studies.

As the axial displacement ΔL increases from 0, the morphology of the deformed beam undergoes three major stages: initial 2D shape, 3D helix/spiral shape, 3D alpha/foldup shape. In section 3.3.1, we will characterize the initial 2D shape and address the question not answered by literature [38], which starts from the assumption that spiral buckling has already come into shape. The question is how the buckling shape transits from initial 2D shape to eventual 3D shape, since the original buckling shape deviating from straight beam remains in a 2D plane before the middle point touches lateral constraints, as shown in Figure 3.13.

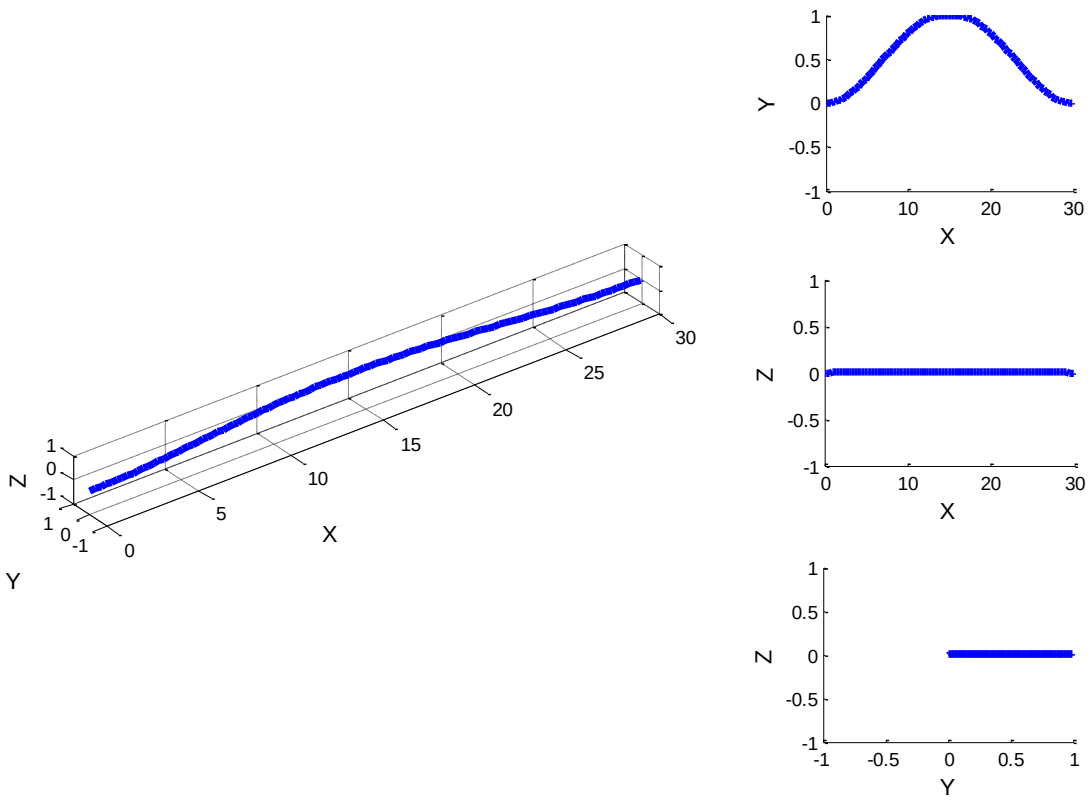

Figure 3.13 Two dimensional buckling shape before contact between beam and constraints. Geometrical

parameters in simulations are $L_0/r = 300$ and $d_t/r = 20$, displacement $\Delta L/L_0 = 0.003$. Lateral constraints are omitted.

To study the 3D buckling shape, Su *et al.* [38] used a smart way to model the general lateral displacement with respect to arc length in equation (3.7), instead of lateral displacement in two separate directions. So the displacement in orthogonal direction can be described in single function, which is still a variation of Euler beam theory nevertheless. Stemming from this idea, the governing equation for the beam at the onset of buckling is written as:

$$EI\frac{\partial^4 y}{\partial s^4} + P\frac{\partial^2 y}{\partial s^2} = 0 \tag{3.24}$$

where y denotes the lateral displacement, s the arc length of the beam (ranging from 0 to beam length L), P the applied compressive force, E Young's modulus and I second moment of area of beam. The boundary conditions at two ends are fixed without rotations:

$$\begin{aligned} y(0) = y'(0) = 0 \\ y(L) = y'(L) = 0 \end{aligned} \tag{3.25}$$

Before the middle point touches the constraints, the deformation remains in a two dimensional plane (although the direction of plane could be arbitrary), equation (3.24) is actually equivalent to equation (3.1) with the following general solution (with $k^2 = P/EI$):

$$y = A\sin ks + B\cos ks + Cs + D \tag{3.26}$$

The coefficients A, B, C and D in equation (3.26) can be determined by boundary conditions [34] described in (3.25) [34]:

$$
\begin{aligned}
B + D &= 0 \\
Ak + C &= 0 \\
A\ \sin kL + B\ \cos kL + CL + D &= 0 \\
Ak\ \cos kL - Bk\ \sin kL + C &= 0
\end{aligned}
\tag{3.27}
$$

In order to have a nontrivial solution for coefficients, the determinant of (3.27) should be zero:

$$
\begin{vmatrix}
0 & 1 & 0 & 1 \\
k & 0 & 1 & 0 \\
\sin kL & \cos kL & L & 1 \\
k\cos kL & -k\sin kL & 1 & 0
\end{vmatrix} = 0 \tag{3.28}
$$

Thus

$$
\sin\frac{kL}{2}\left(\frac{kL}{2}\cos\frac{kL}{2} - \sin\frac{kL}{2}\right) = 0 \tag{3.29}
$$

One solution for equation (3.29) is:

$$
\sin\frac{kL}{2} = 0 \tag{3.30}
$$

That indicates

$$
kL = 2n\pi \tag{3.31}
$$

and

$$
P_{cr} = \frac{4n^2\pi^2 EI}{L^2} \tag{3.32}
$$

So with value of *kL* determined, we can proceed to determine the value of coefficients:

$$
A = C = 0, \quad B = -D \tag{3.33}
$$

Therefore the buckling beam before the contact in corresponding to $n = 1$, and the

shape is:

$$y = B\left(\cos\frac{2\pi s}{L} - 1\right) \tag{3.34}$$

Coefficient B can be determined by extra geometrical constraints, but the general cosine shape can be discerned in XY projection of Figure 3.13. The smallest critical force is corresponding to $P_{cr} = 4\pi^2 EI/L^2$.

Upon beam's touching the lateral constraints, another boundary condition is added to the beam in equation (3.25):

$$y(L/2) = H, \quad y'(L) = 0 \tag{3.35}$$

with H being the radius of the cylindrical constraints. Therefore the coefficient B in equation (3.34) can be determined using the geometrical constraints:

$$y = \frac{H}{2}\left(1 - \cos\frac{2\pi s}{L}\right) \tag{3.36}$$

Equation (3.29) has another solution in addition to (3.30):

$$\tan\frac{kL}{2} = \frac{kL}{2} \tag{3.37}$$

For this scenario, $kL/2$ is approximately equal to 1.43π, 2.45π, 3.47π, 4.48π, *et al*. Therefore we can combine the two series of solution in equation (3.30) and (3.37), and the consequential critical forces P_{cr} in ascending order are obtained in the following series:

$$P_{cr} = \frac{4\pi^2 EI}{L^2}, \frac{8.18\pi^2 EI}{L^2}, \frac{16\pi^2 EI}{L^2}, \frac{24.01\pi^2 EI}{L^2}, \frac{36\pi^2 EI}{L^2} \cdots\cdots \tag{3.38}$$

The first two critical forces, *i.e.* first solutions of (3.30) and (3.37), are corresponding to first two buckling shapes in Figure 3.14. Immediate observation of simulation results reveals that first buckling modes are embodied in XY and XZ projection

in the initial stage of 3D buckling at Figure 3.15.

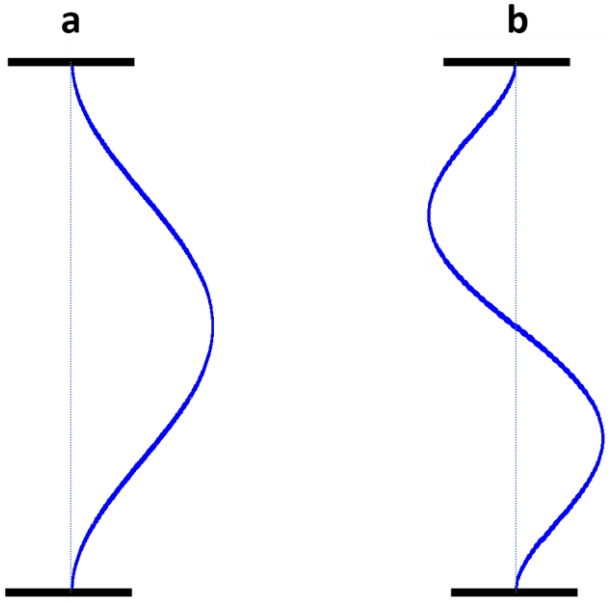

Figure 3.14 Buckling Mode of three dimensional beam with clamped boundary conditions under lateral constraints: a) first buckling mode, b) second buckling mode. Lateral constraints are omitted.

After comparison between 2D buckling shape in Figure 3.13 and 3D buckling shape in Figure 3.15, we could observe that 2D buckling begins to transit to 3D buckling after point contact between the middle point of beam and lateral constrains. While maintaining first buckling mode as illustrated in Figure 3.14a and XY projection in Figure 3.15, second buckling mode (Figure 3.14b and XZ projection in Figure 3.15) in perpendicular to first buckling mode develops as the compression proceeds. So the inception of 3D buckling shape is a superposition of two buckling shape in orthogonal direction, and the compressive force at the instant of 2D-3D transition is predicted theoretically to be $P_{cr} = 8.18\pi^2 EI/L^2$.

Even though the above theoretical analysis is a simplified estimation, it catches

the essentials when compressed beam transits from planar shape to spatial shape. The estimated value of $8.18\pi^2$ (≈ 80) is found to be consistent with the value of 79 at the 2D-3D transition with the middle point as anchor in literature [59, 60].

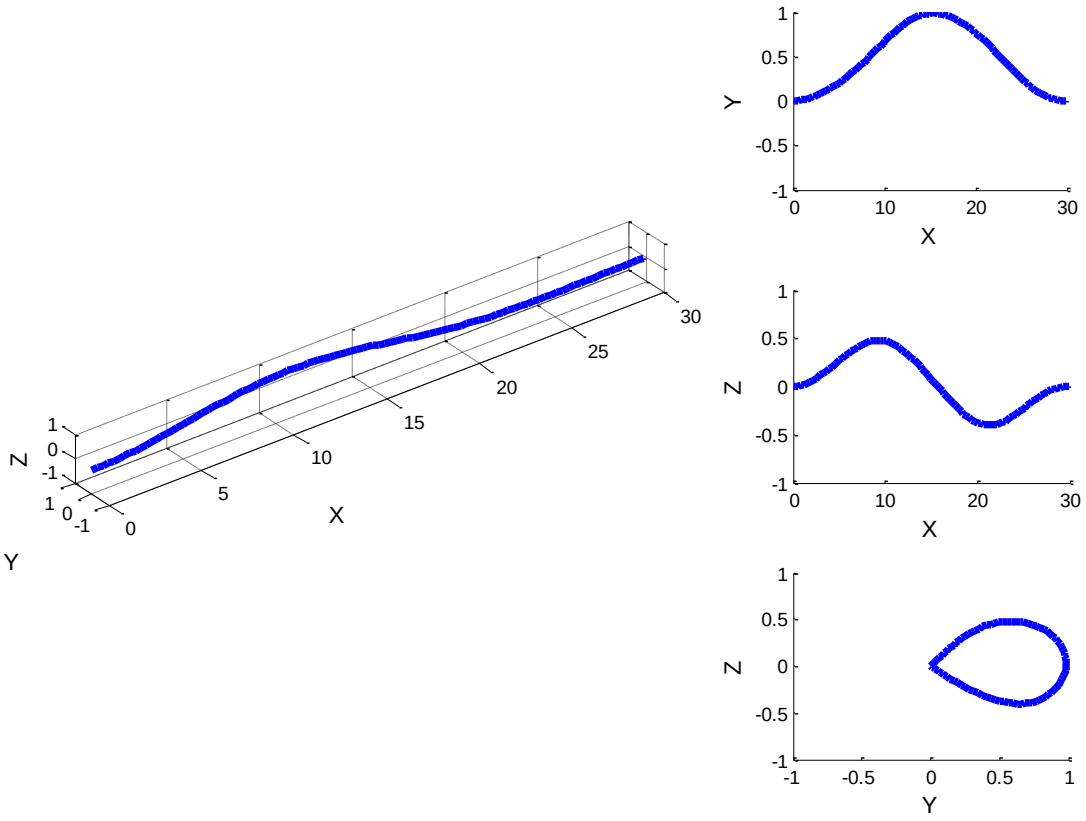

Figure 3.15 Three dimensional buckling beam after contact between beam and constraints. Geometrical parameters in simulations are $L_0/r = 300$ and $d_r/r = 20$, displacement $\Delta L/L_0 = 0.005$. Lateral constraints are omitted.

The initial lateral amplitude of buckling mode 2 (Figure 3.14b and XZ projection in Figure 3.15) is small at the transition point. But the lateral amplitude keeps on increasing as the compression continues, until the beam comes into contact with lateral constraints in the second direction (orthogonal to the initial direction). After these second contacts, the spiral shape comes into full bloom which is the presumption of literature [38], and the half

circle in YZ projection of Figure 3.15 evolves to full circle in YZ projection of Figure 3.16. Therefore, the contact part between beam and constraints increase from initial point contact to subsequent line contact.

3.3.2 The spiral/helix shape

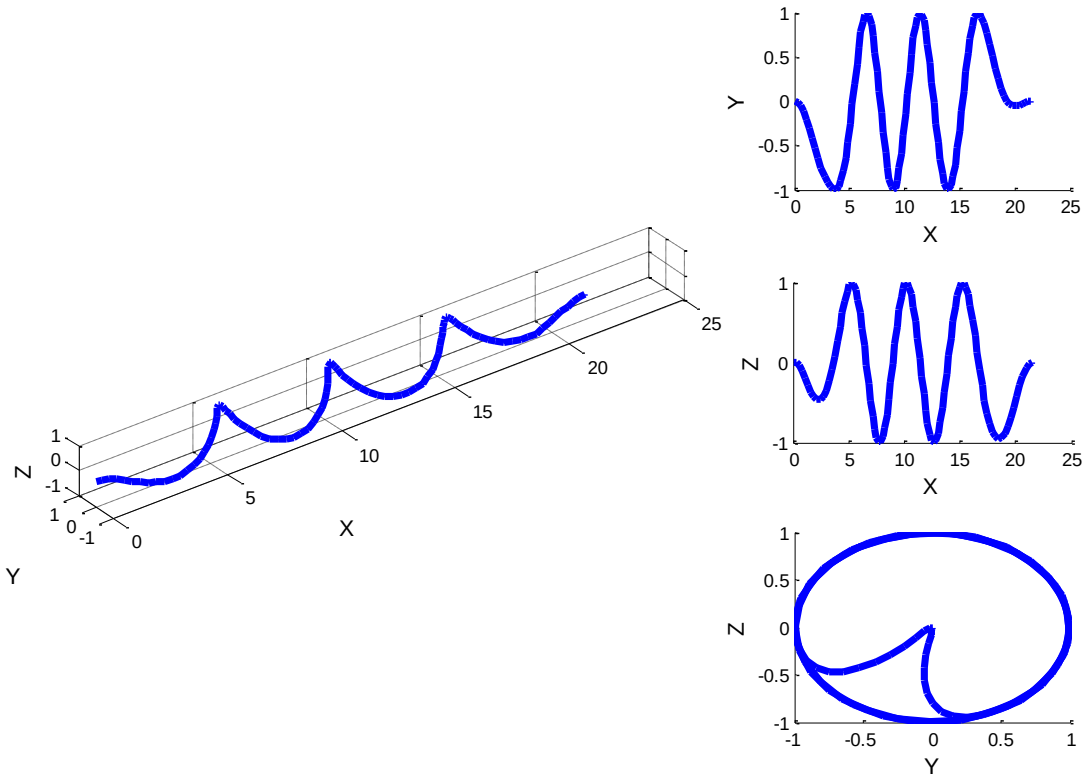

Figure 3.16 Spiral shape of buckled beam in cylindrical constraints. Geometrical parameters in simulations are $L_0/r = 300$ and $d_t/r = 20$, displacement $\Delta L/L_0 = 0.3$. Lateral constraints are omitted.

At moderate displacement $\Delta L/L_0 = 0.3$, the post-buckling spiral shape is illustrated in Figure 3.16. The distinct feature in the spiral shape is that almost all of the beam section except sections near two ends come into contact with the surrounding cylindrical constraints, as seen in the shape in YZ projection. This is in contrast to the 2D post-buckling

shape, where only a small portion of beam, *i.e.* straight section in Figure 3.3 and Figure 3.6, is touching the lateral constraints.

Despite the full contact between beam and constraints, sinusoidal shape can still be observed in lateral projections, *i.e.* XY projection and XZ projection in Figure 3.16. Su *et al.* [38] proposed that the onset of 3D spiral shape is the superposition of buckled shape in two perpendicular direction, which occur simultaneously at the same compressive stress. We can observe in Figure 3.16 that post-buckling spiral shape is indeed the superposition in orthogonal directions.

As explained in section 3.3.1, point contact develops into line contact in spiral shape. And the contact length of the beam is also increasing as the axial displacement ΔL increased in the helix stage, as illustrated in Figure 3.17.

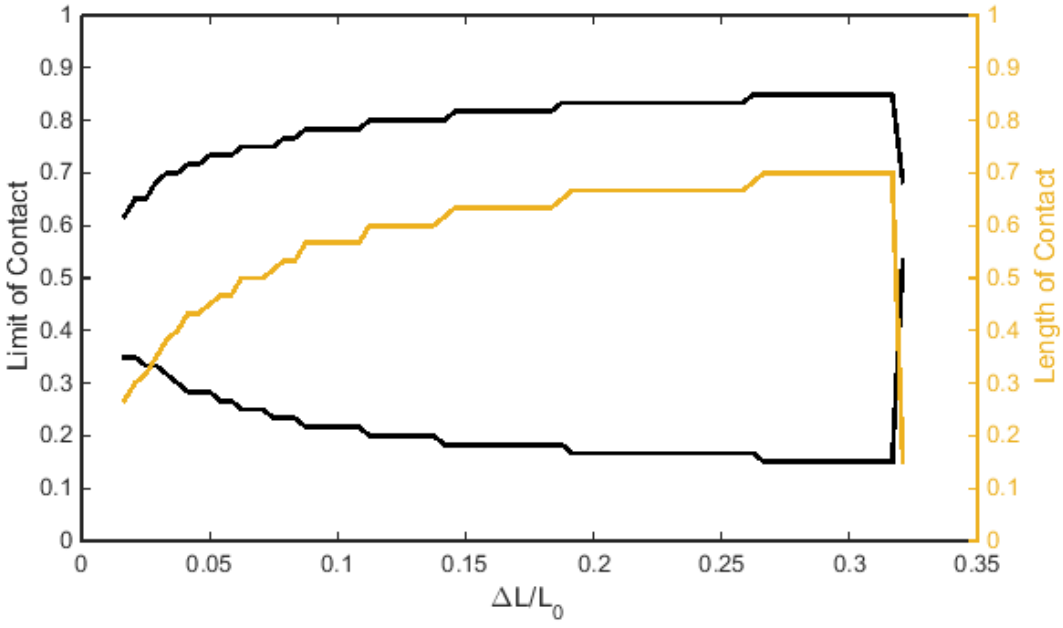

Figure 3.17 Limit and length of line contact in spiral shape for simulations case $L_0/r = 600$ and $d_t/r = 50$

In order to better describe the shape of spiral/helical stage, Euler angles (ϕ, θ, ψ) for local basis ($\mathbf{e}_1$, $\mathbf{e}_2$, $\mathbf{e}_3$) need to be introduced beforehand. As illustrate in Figure 3.18, Euler angles are defined through a first rotation about Z axis by angle ϕ, a second rotation about X axis by angle θ, and finally a rotation about Z axis by angle ψ.

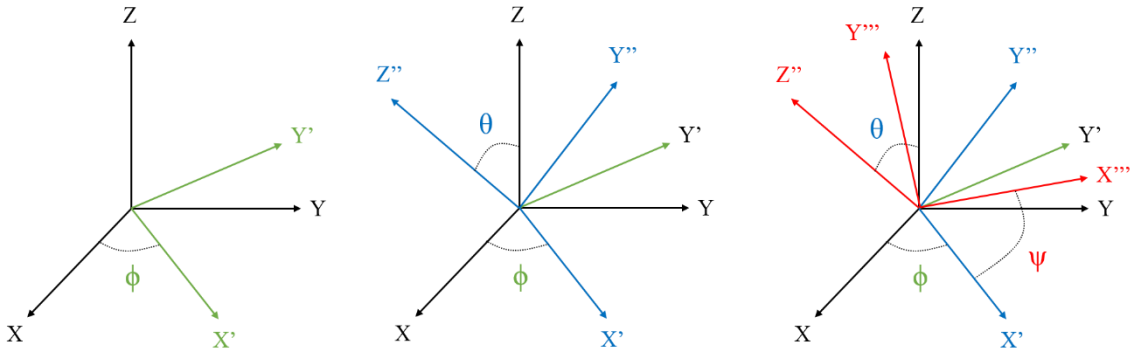

Figure 3.18 Euler angles (ϕ, θ, ψ) at local basis

Using the newly defined rotation angels, torsion equation (3.22) can be derived further into the following [53, 55-57]:

$$\tau = w_3 = \frac{d\psi}{ds} + \frac{d\phi}{ds}\cos\theta = constant \tag{3.39}$$

Equation (3.39) indicates that torsion τ consists of two parts: internal twist $\frac{d\psi}{ds}$, and tortuosity $\frac{d\phi}{ds}\cos\theta$ which is determined by the general shape of the centerline of curve. The internal twist can be best visualized by the colored strip near the two ends in Figure 3.11, since tortuosity or curvature is zero towards two ends.

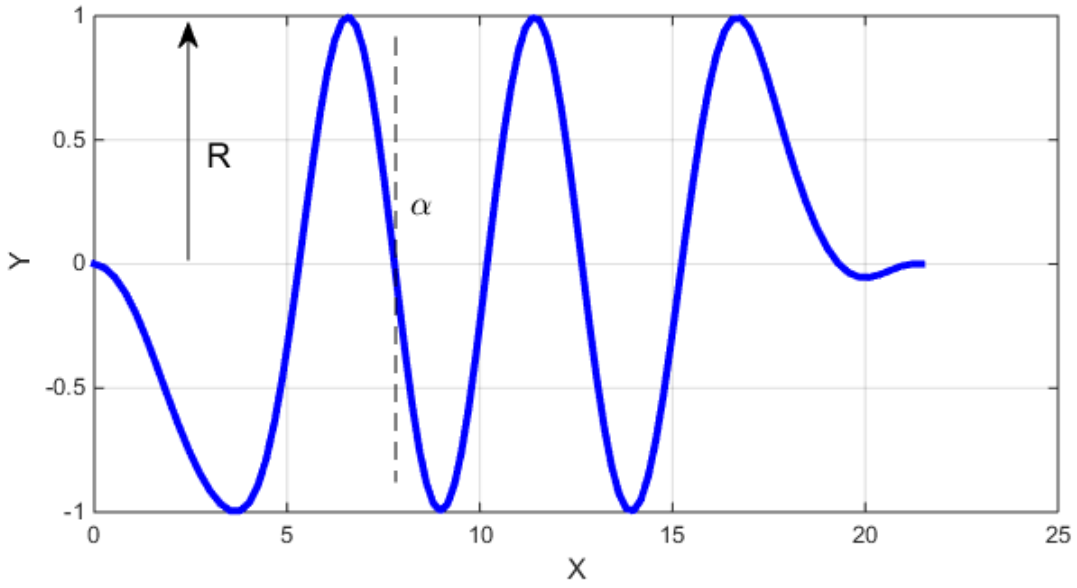

Figure 3.19 Helix shape in the XY projection with illustration of Euler angle $\theta = \pi/2 - \alpha$ and radius of constraint R

Employing the Euler angles in the spiral shape, $\theta = \pi/2 - \alpha$ is illustrated in Figure 3.19 where α is the tilt angle between helix and cross section of circular constraint. Angle θ or α is uniform in the helix section. And the tortuosity can be further derived to:

$$\frac{d\phi}{ds}\cos\theta = \frac{\sin\theta\cos\theta}{R} \tag{3.40}$$

The internal twist $\frac{d\psi}{ds}$ is usually determined from boundary condition, but literature [61] proved experimentally that the internal twist is $2(1+\nu)$ per period of helix right before the transition from helix shape to alpha shape.

Bending energy is a function of curvature for the centerline and bending stiffness of beam. The curvature for a standard helix shape is determined by the tilt angle α and radius of helix/constraints R:

$$\kappa = \frac{\sin\theta \sin\theta}{R} \tag{3.41}$$

Therefore, the bending energy and torsion energy for unit arc length in the helical shape can be expressed as a function of θ since curvature κ and torsion τ are both functions of θ, if we assume the segments close to the two ends are in uniform helical shape:

$$E_{total} = E_{bending} + E_{torsion} = \frac{1}{2}EI\kappa^2 + \frac{1}{2}GJ\tau^2 \tag{3.42}$$

Angle θ or α is then related to displacement ΔL for the two ends under the assumption that the total arc length L_0 for the beam is constant through the deformation process (we have discussed that the axial strain of beam is negligible)

$$\alpha = \sin^{-1}\left(1 - \frac{\Delta L}{L_0}\right) \tag{3.43}$$

Number of periods for the helix can then be calculated as

$$n = \frac{L_0 \cos\alpha}{2\pi R} \tag{3.44}$$

Therefore, the total shape and total strain energy for the helix shape at a certain axial displacement ΔL can be determined.

3.3.3 Foldup/alpha stage in the 3D post-buckling shape

At moderate compression, the post-buckling beam exhibits spiral shape as depicted in Figure 3.16. If the compression continues, the spiral shape becomes unstable again at certain point, and a new state called foldup or alpha shape comes into being as illustrated in Figure 3.20. After the transition, the monotonous shape in XY projection and XZ projection becomes tangled up and the beam no longer touches the lateral constraints

perfectly in the YZ projection. Literatures [59, 60] describes the schemes for touching and non-touching parts which is drawn from their simulation results, and they also confirmed the detachment between the beam and lateral constraints in alpha shape. Therefore, there are two criteria indicating the transition from helix shape to alpha shape: first the contact length decrease as illustrate in Figure 3.17; second the certain part of beam is detaching from constraints compared with perfect contact in helix shape.

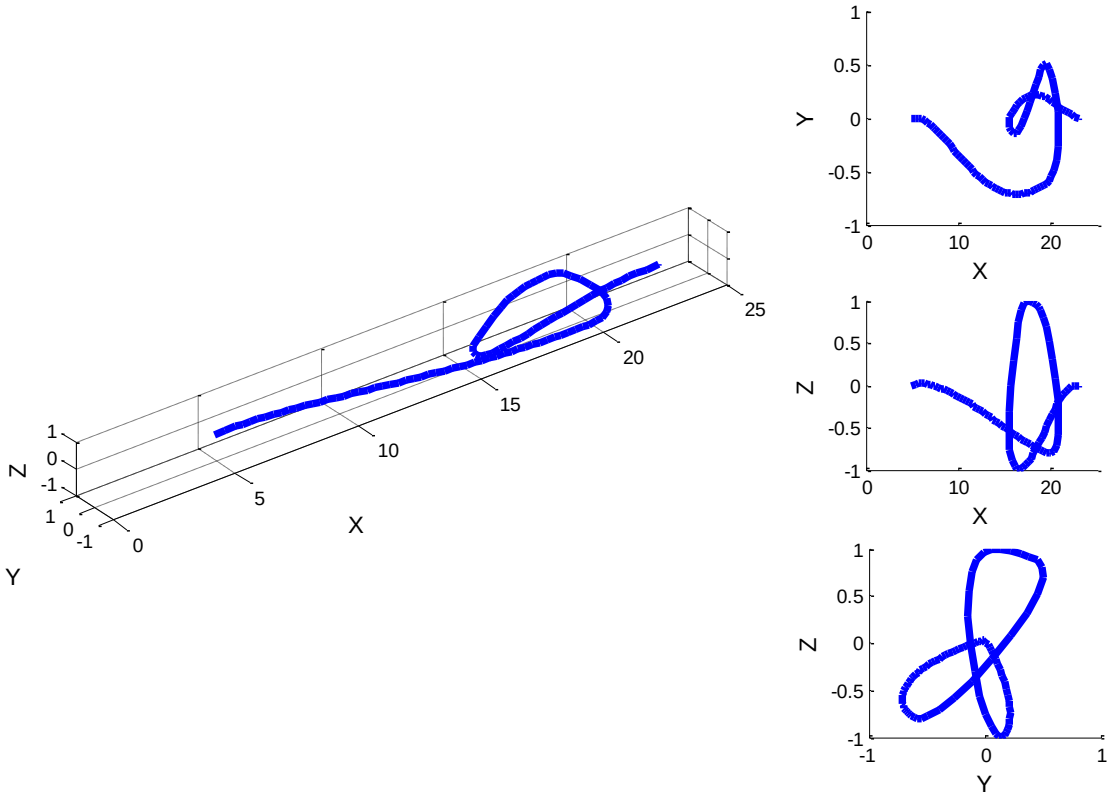

Figure 3.20 Foldup shape for the post buckling beam. Geometrical parameters in simulations are $L_0/r = 300$ and $d_t/r = 20$, displacement $\Delta L/L_0 = 0.36$. Lateral constraints are omitted.

This foldup stage is comparable to the post buckling stage of compressive beam in 2D plane studied in reference [48], a typical non-linear behavior which cannot be

described by the linear Euler beam equation. The transition from structured spiral shape to messy foldup shape dissipates energy stored in the beam, and it is an abrupt event. Therefore this transition can also be exemplified by the internal energy of the whole beam. As seen in Figure 3.21, the internal energy of the whole beam keeps on increasing smoothly from initial 2D shape into the 3D spiral shape, then it undergoes a sudden decrease at the transition point into a relatively stable foldup stage.

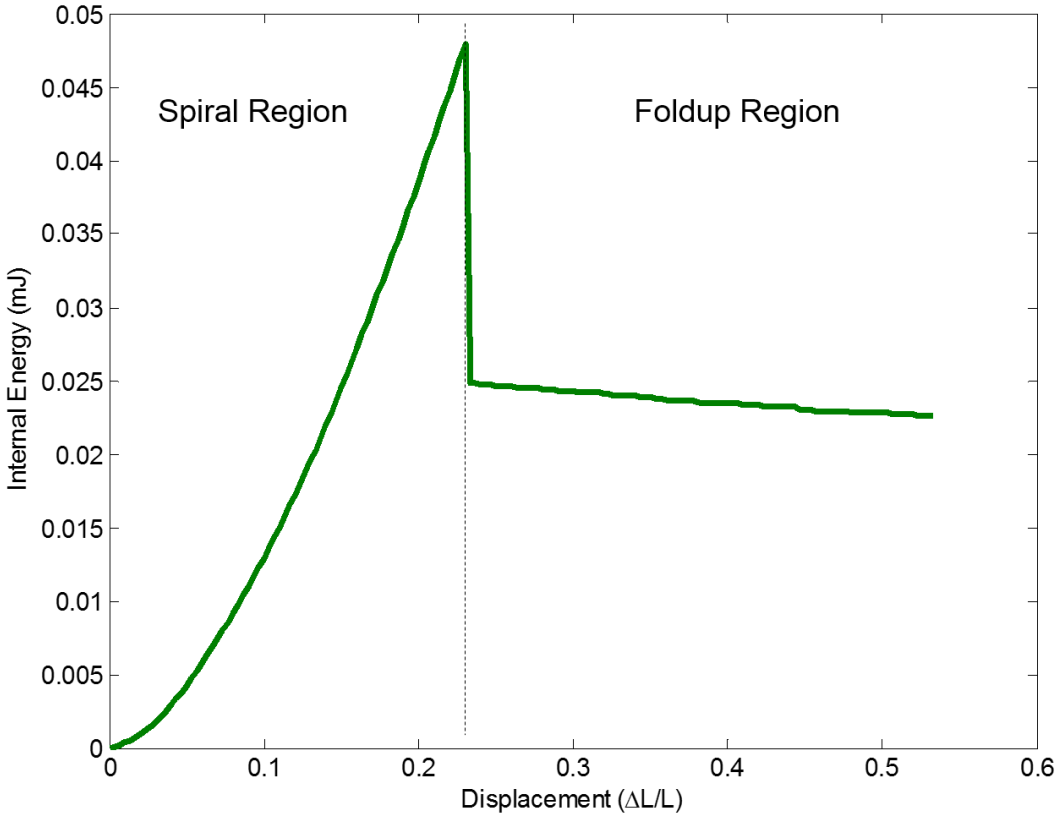

Figure 3.21 Internal energy of the three dimensional buckling beam under cylindrical constraints at different compression rate, from simulation. Spiral shape and subsequent foldup shape can be distinguished by the abrupt change of internal energy.

Since the transition point can be pinpointed by observing the change of strain

energy, this leads us to believe that we can propose a theoretical solution for transition point by comparing the elastic energy between helix shape and alpha shape. The bending energy and torsion energy for helix shape is already calculated using equation (3.42) as we assume that the whole beam takes uniform helix shape without end segments. Helix shape is easier to process since it assumes an ordered pattern, while the alpha shape possesses more difficulties since the its shape can't be expressed in a simple analytical way. However, we can utilize the solutions from established literatures [55], and insert the solution as a template to our current theoretical framework.

The curvature for the alpha shape through L can be expressed as

$$\kappa^2 = \frac{4P}{EI} sin^2\left(\frac{\theta}{2}\right) \tag{3.45}$$

where P denotes the force at both ends

$$P = \frac{EI}{\lambda^2} \tag{3.46}$$

λ represents the characteristic length

$$\lambda = \frac{\Delta}{8A} \tag{3.47}$$

Where A is nondimensionlized parameter depending on the general shape at alpha stage with A = 1 corresponding to zero gap (self-touch on the beam) and A = 0.3 corresponding to wide gap in the side view. In our case, we take A = 0.8 by comparing the shape in our simulation and that in literature [55].

θ is no longer a constant as the helix shape, and there is a maximum value at the center of beam. $\sin\frac{\theta}{2}$ in equation (3.45) can be calculated as

$$\sin\frac{\theta}{2} = \frac{A}{cosh(Al/\lambda)} \tag{3.48}$$

There are two points which are key to ensure compatibility between helix shape and alpha shape when using the solution template: firstly the axial displacement $\Delta L/L_0$ is consistent before and after transition; secondly the torsion decreases by a certain amount $\Delta\tau$ which can be calculated using the following equation from literature [55]:

$$\Delta\tau = \tau_{helix} - \frac{4}{L}\sin^{-1}\left(\frac{B}{4\lambda}\right) \tag{3.49}$$

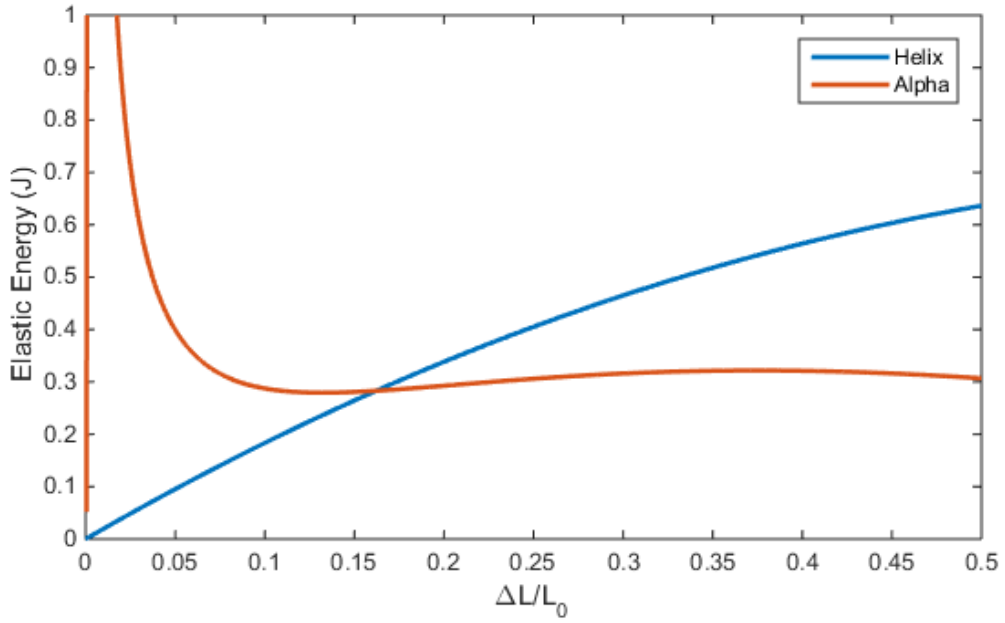

Figure 3.22 Strain energy between helical shape and alpha shape at different axial displacement, calculated from theoretical model in section 3.3.3

We then can insert the calculated curvature and torsion in to equation (3.23) to obtain total strain energy for alpha shape. Furthermore, the strain energy for alpha shape can be compare to that in helix shape at a certain displacement $\Delta L/L_0$. As illustrated in Figure 3.22, the strain energy in the helix shape increase together with displacement $\Delta L/L_0$

while the strain energy in the alpha shape decreases together with $\Delta L/L_0$. When the axial displacement is small, strain energy for helix shape is larger than that for alpha shape. Once the axial displacement reaches a critical point, alpha shape serves as better energy efficient alternative to the helix shape, and we would expect the transition happens at this displacement.

In our theoretical model we don't consider the boundary effect of the beam, so we choose long beam with $L_0/d_t > 300$ to minimize the effect from two ends. Actually in literatures [53, 57], they also neglect the two end and the found consistent trend in relevant parameters. The boundary effect can be exemplified by the contact length in Figure 3.17, as in that case contact length is always smaller that 70% of the whole beam. We only wish to demonstrate the general trend of strain energy in helix shape and alpha, the exact shape of buckled beam should be calculated with the inclusion of boundary parts.

We survey the number of period at the transition point with respect to geometrical parameter L_0/d_t in Figure 3.23. The number of period can be measured in YZ projection of Figure 3.16. Critical number of periods is in a very good linear relation with L_0/d_t, which means that the beam/rod assumes a constant shape at the transition point. We can also infer from the linear correlation that the ratio bending energy over torsion energy is a constant value because of the self-similar phenomenon. When the critical period number is smaller than 1, we could observe a smooth transition of strain energy from helix shape alpha shape, *i.e.* α1 in Figure 3.23. When the critical period number is larger than 1, we could observe a

sharp decrease of strain energy from helix shape alpha shape, *i.e.* α2 in Figure 3.23.

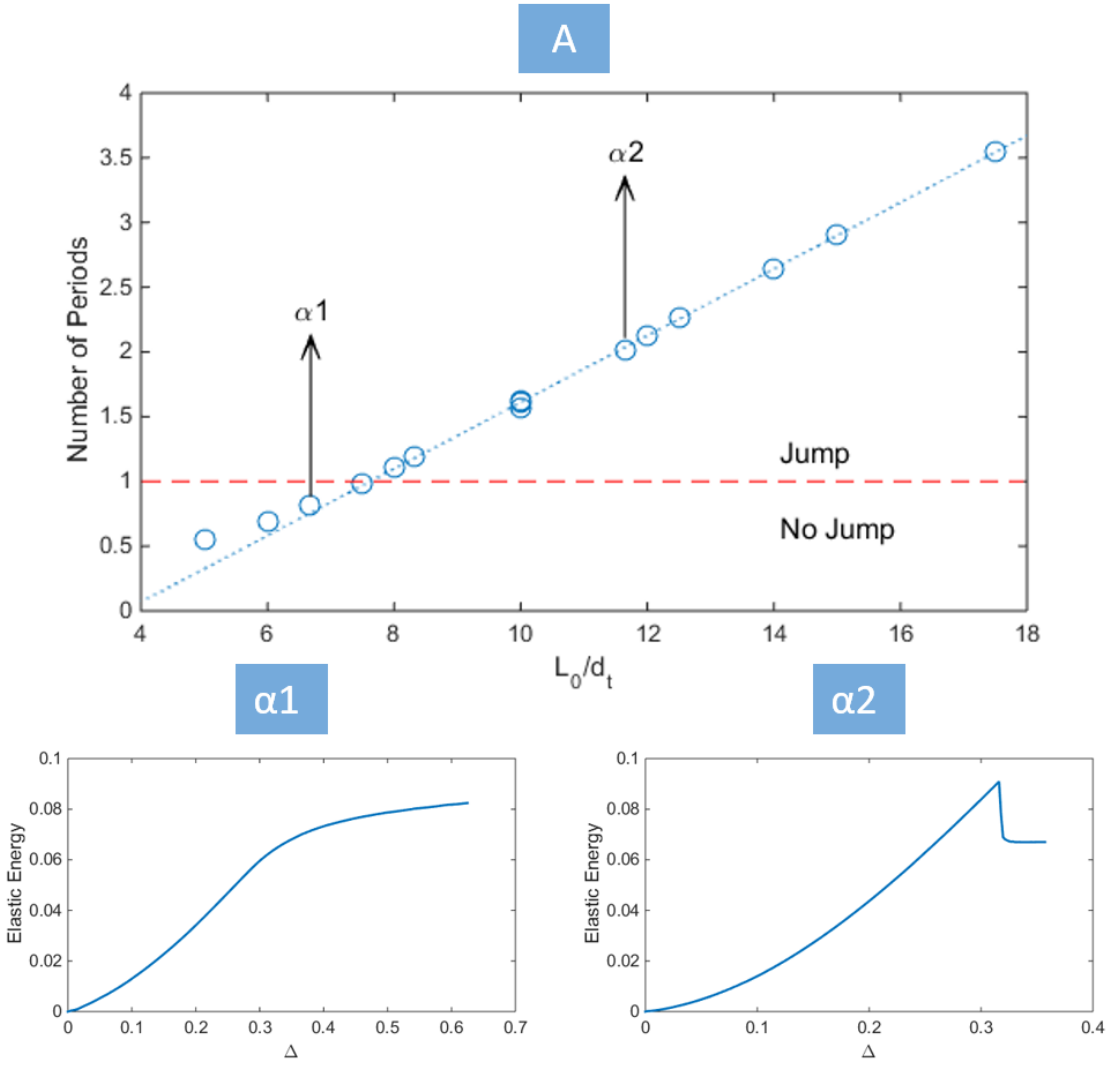

Figure 3.23 A: number of period at the transition point from helix shape to alpha shape VS L_0/d_t. The simulation case corresponding to sudden decrease of strain energy is noted as α1, the simulation case corresponding to smooth transition of strain energy is noted as α2

We then compile in Figure 3.24 the transition point $\Delta L/L_0$ from helix shape to alpha shape under different circumstances extracted from FEM simulations, and we can examine the effect of geometrical parameters L_0/d_t and d_t/d_b on transition, just as what we did in chapter 3.2 for two dimensional beam buckling. Longer beams tend to possess larger

critical displacement due to larger strain energy stored in beam and therefore larger inertia. On the other hand, wider constraints can promote the transition from helix shape to alpha shape since wider constraints induce smaller bending energy.

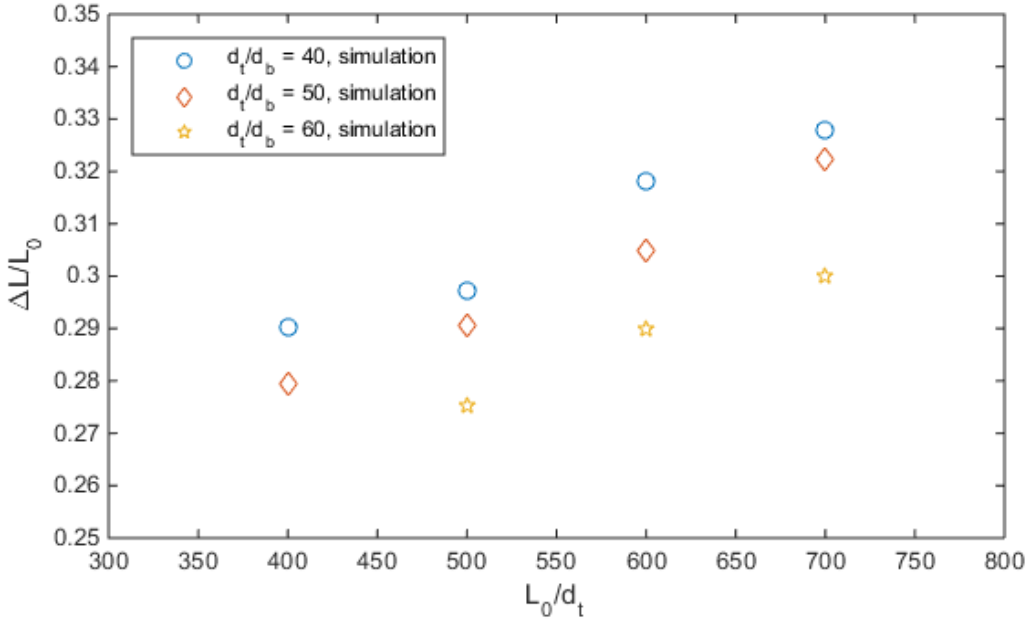

Figure 3.24 Critical displacement from helix shape to alpha shape as a function of L_0/d_t and d_t/d_b from FEM simulations

3.4 Conclusion and further discussions

In this chapter we have demonstrated analytically and numerically the buckling shape and post-buckling shape of elastic beam under lateral constraints in 2D plane as well as in 3D space. We have also studied the transition between different buckling and post buckling modes in both of the cases. In 2D buckling beam with lateral constraints, the beam can be divided into curved segments not touching constraints and straight segments contacting constraints. On the contrary, the beam in 3D shape has more freedom to move

close to lateral constraints, so in the spiral stage almost every section of beam is touching the constraints. Despite its complexity, the 3D buckling shape can be decomposed into trigonometric curves in perpendicular planes, which is reminiscent of the basic buckling shape in 2D plane.

We also studied preliminarily different shape of cross section for lateral constraints in the 3D case, especially constraints with square cross section instead of circular cross section. The spiral buckling shape basically remains, although the line contact between beam and constraint in circular constraints becomes point contact between beam and constraints in square constraints. We then proceeded to design a specific experiment to examine the role of lateral constraints on the spiral shape of buckling beam. We used a cardboard as the square constraints since it is easy to flip one side of the cardboard. First the beam was compressed to the mentioned spiral state, and then we flipped one side of the constraints. We observed that the buckled beam immediately pop out of the constraints, even though the friction between beam and constraints acts to refrain the popping-out. This indicates that all of the four sides of constraints are necessary to maintain the spiral buckling shape, the spiral shape is not stable under three sided constraints. A Finite Element Analysis using ABAQUS also confirms that buckling beam can’t even form spiral shape with three sided constraints, adding to the understanding that four sided constraints are essential to the spiral buckling shape. Other details of square lateral constraints need to be explored numerically and experimentally in future study.

In addition to the study of morphology, we can utilize this buckling mechanism to collect and reuse energy. Kinect energy of the environment can be converted into strain energy in the spiral beam using the compression process. Meanwhile, the stored energy can be reused if the compressing end is released, and this end will bounce back to its original position and release strain energy. The beam should not be compressed into alpha shape, since the reaction forces at the ends in alpha shape reverse direction from helix shape. Therefore, the critical displacement in Figure 3.24 can guide the design of device. There is also another way to release the buckled beam by flipping one part of the lateral constraints. The buckled beam will pop out of constraints in lateral direction, which is discussed in the above paragraph.

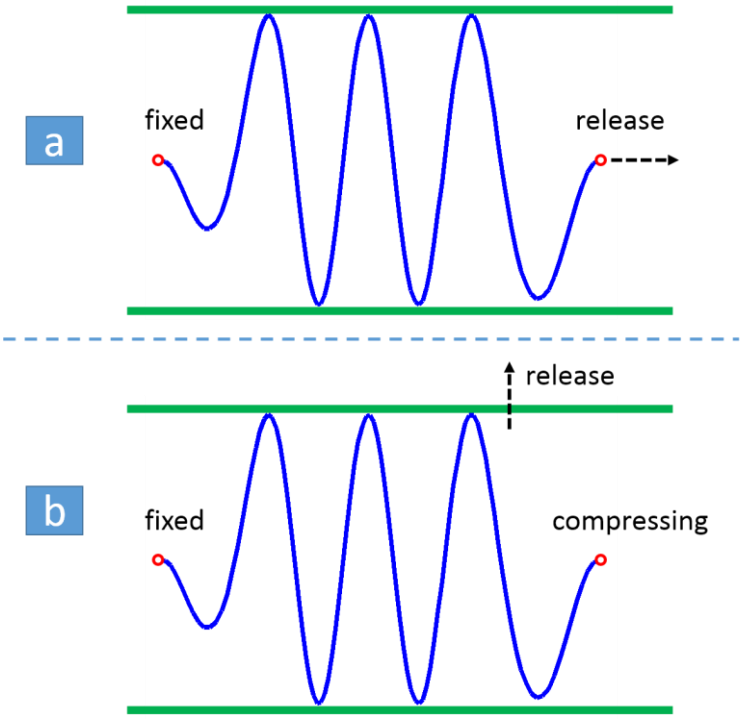

Figure 3.25 Different release mechanism: *a*, release one end of the buckled beam; *b*, flip one side of the lateral constraints.

In all of the cases, friction plays an important role in the buckling process. Friction acts to prevent the relative motion between beam and constraints, so transition between different buckling modes would be delayed if friction is to be considered. Conceivably, the friction will dissipate strain energy stored in the buckling beam. We covered surface of beam and constraints with oil to minimize the friction in experiments and we don't consider friction in all of the simulation and theoretic analysis. When the friction is large enough that it can prevent the sliding of beam on the surface of constraints, which is the reason behind lockup shape in the drilling bit [39]. Nevertheless, friction does exist in reality, and it should be studied in future research.

Finally, our study in buckling beam under lateral constraints can contribute to the belief that some intriguing behaviors in nature, be it morphology of plants [62, 63] or morphology of animals, can be explained from the perspective of solid mechanics, especially buckling phenomena. As a possible extension in future, understanding this could also lead to advance of design of snake robots [64] or mechanical self-assembly [5].

Chapter 4.Buckling of Solid Shell/Liquid Core Structure

4.1 Buckling of elastic film on planer compliant substrate

Since the pioneer work of buckling film on a compliant substrate published in 1998 [65], in which nanoscale metal film deposited on thick elastomer substrate is under compression and then losses its stability to alleviate stress, researches on this topic has undergone substantial growth during the past two decades [66, 67]. The amplitude of initial buckling shape of one dimension, *i.e.* wrinkling, might increases eventually into a state where deep valley emerges, *i.e.* folding [68-70]. For soft substrate without hard skin, the amplitude of buckling increases until self-contact happens, *i.e.* creasing state [71, 72]. While for equi-biaxial compression, Chen discovered that among several competing buckling modes herringbone shape possess the lowest energy and is the most effective way to alleviate biaxial compressive stress [73, 74]. Other soft substrates have been studied, such as liquid as substrate [75-81], and these system exhibit unique deformation shape since surface tension comes into interact with the system.

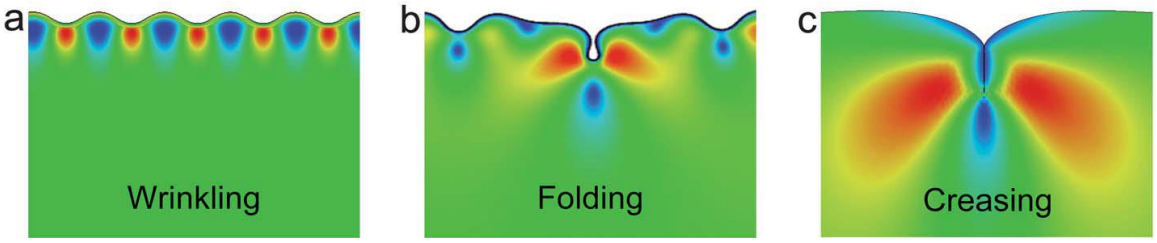

Figure 4.1 Three stages of buckling film on compliant substrate in one dimension: a), wrinkling; b) folding;

c) creasing [68].

Although buckling has been historically viewed as malfunction and undesirable, researchers recently has proposed to utilize the buckling shape of bonded film-substrate structure to achieve flexible electronic devices, since the whole system can be stretched or compressed without breaking the working structure [82]. Furthermore, researchers have design partially bonded film-substrate structure to achieve even greater flexibility, of which the films or beams are designed to pop up from the substrate [83, 84].

4.2 Buckling of elastic film on substrate with curvature

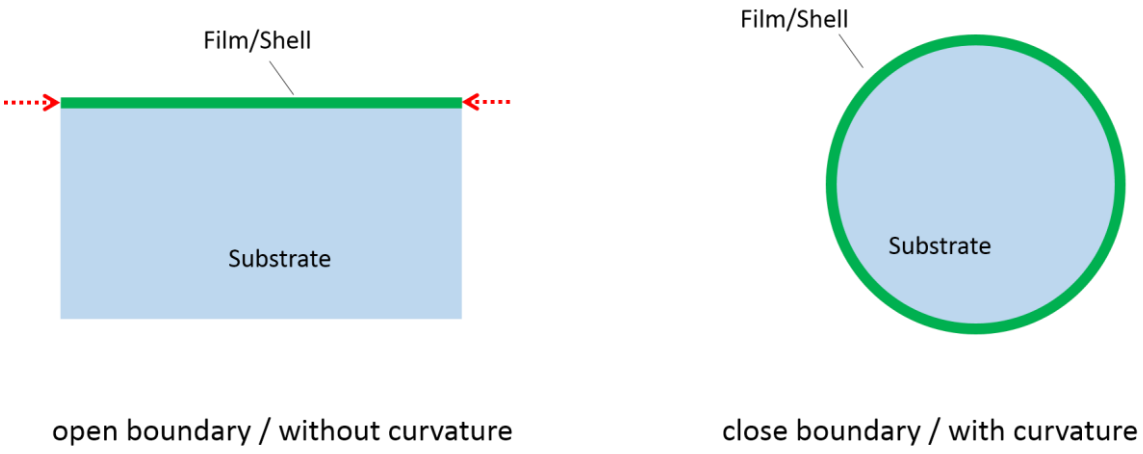

Figure 4.2 Substrate without or with curvature. Open boundary and closed boundary are also compared.

Previous section briefly summarized the buckling film on planar substrate, but the film buckling is also greatly affected by the curvature of the substrate. Researcher has already demonstrated that curvature could alter the stiffness of shell structure [85, 86]. Also, the buckling of a closed system is different from that of system with open boundary, as new geometrical constraints have been introduced. Cao *et al.* demonstrated that triangular and

labyrinth patterns appear as a result of biaxial compressive stress in spherical shell [87]. For post buckling analysis, the core/shell structure also exhibits similar wrinkling-to-folding transition as open system does [88]. Instead of imposing global compressive stress, Vella *et al.* use a point force to introduce localized compressive stress, and they showed interesting wrinkles patterns [89-91] not seen on a solid substrate. In addition to liquid core, researchers also explored the solid shell filled with air, a compressible fluid, and the system shows unique deformation patterns due to the compressibility of air [92, 93].

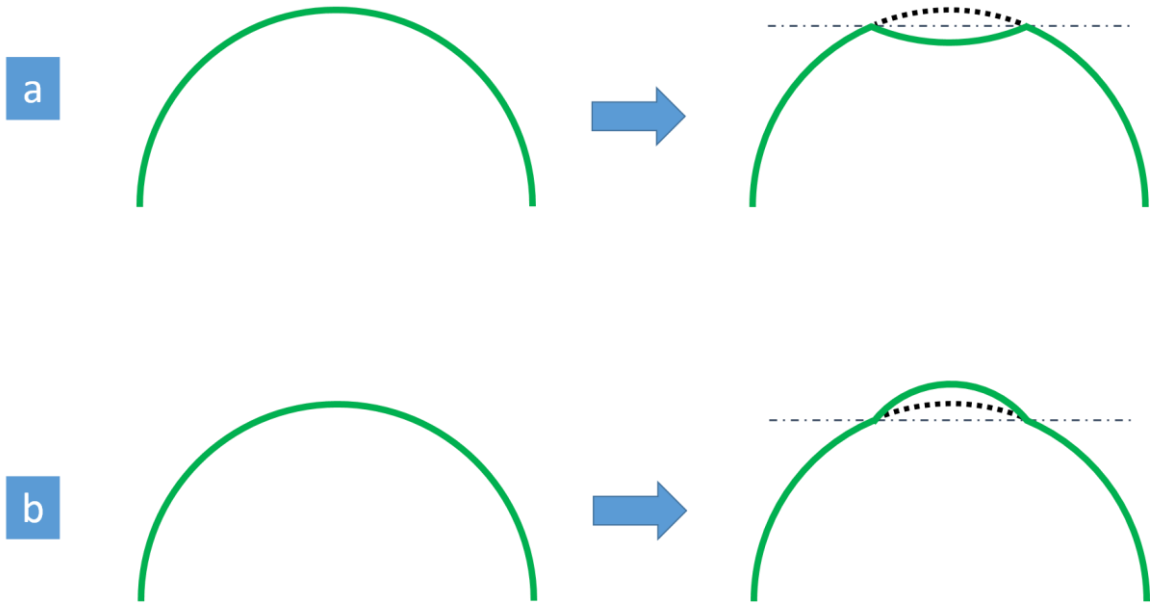

Figure 4.3 a) Mirror reflection (concave shape) as the buckling shape for thin shell structure; b) protruding shape of buckled shell.

The typical buckling shape for a convex shell structure will be the mirror reflection which forms a concave shape on the original convex structure (see Figure 4.3a). As Pogorelov explained in his book [94] using geometrical arguments, shell structure tends to maintain its original length by adapting the mirror-reflected shape, even though it incurs

large local curvature in consequently bending. That's because the bending stiffness for thin shell structure is much smaller than of stretching ability, so bending is easily accomplished than stretching. Previous researches have also confirm this trend of deformation [62, 87], and our simulation results generally follow this rule.

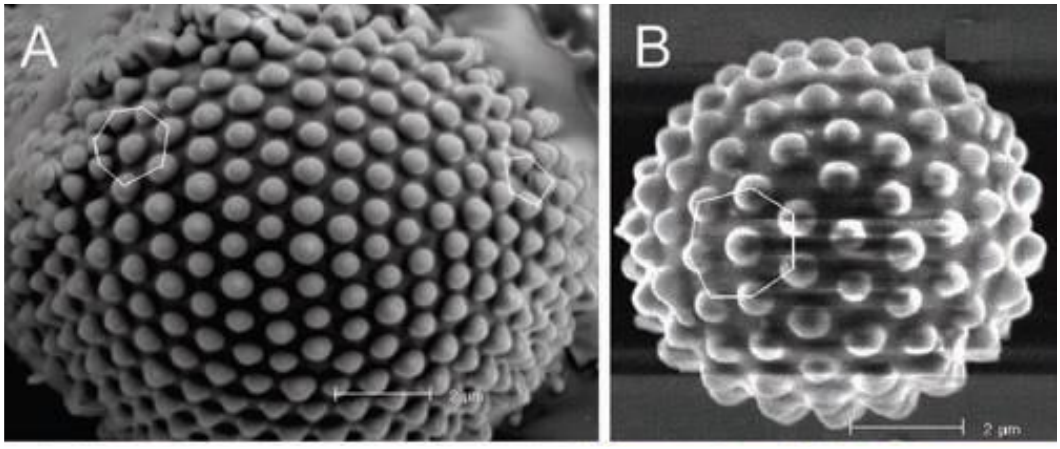

Figure 4.4 Convex deformation on silicon dioxide shell filled with silver core [95].

Nevertheless, Researcher reported that solid shell/liquid core structure can generate protruding deformation [95] illustrated in Figure 4.3b. It is an intrigue problem which falls out of general theoretic predictions. In Figure 4.4, the protruding deformation occurs on the system with very thin SiO_2 film encompassing the Ag core. The whole system was cooled from temperature of 1535 K when the Ag core is melted. As the temperature decreases, the thermal expansion coefficient of SiO_2 is larger than that of Ag, which means the solid shell shrinks more than the liquid core does. At the same time, the solid shell and liquid core remain bonded, which renders SiO_2 shell under compressive stress. We will try to identify how and when the concave deformation comes into shape in the future

discussion section 5.2.3.

On the application side, Yin *et al.* utilized the soft core / hard shell model to successfully explain the intrigue wavy shape found on a lot of vegetables and fruits [5, 62, 96], and they further proposed to employ this mechanical self-assembly to fabricate micro/nano scale gears.

What we are going to explore in this chapter will be a new model with elastic solid shell encompassing liquid core. Although researchers showed different buckling shape of liquid droplet coated by nanoparticles in which the particle layer is deemed to be a continuum solid phase [97-103], a systematically study still lacks. By building this model, we plan to explain the morphologies of cell and cell nucleus [104-107] and relate the morphologies to diseased cell at different stage and to the stress or pressure applied on the surface of cells [108-113].

4.3 The modeling of liquid core

Typical fluid mechanics is formulated under the Eulerian coordinates, *i.e.* fluid flowing past specific fixed locations and we are studying the fluid properties at these specific locations as time lapses. But our study object, *i.e.* a closed liquid domain, should be formulated under Lagrangian coordinates, *i.e.* we are travelling together with fluid domain through space and time. Researchers have done relevant studies using Lagrangian formulation, such as the evolution of liquid droplet [114, 115]. At low Reynolds number,

Navier-Stokes equation are reduced to Stokes equation with continuity equation (body forces are negligible):

$$\mu\nabla^2\mathbf{u} = \nabla p$$
$$\nabla \cdot \mathbf{u} = 0 \tag{4.1}$$

where $\mathbf{u}$ is the velocity of fluid, p the pressure and μ dynamic viscosity. However, the coupling between liquid core and solid shell has to be considered if this liquid model is to be used, and the Fluid-Solid Interaction (FSI) is usually computationally expensive. Therefore, we proposed to model the fluid core under the framework of solid mechanics to ensure the compatibility and convenience of computation.

For the liquid core (a Newtonian fluid), the shear stress is equal to viscosity multiplying shear strain rate in the liquid. In the cases where deformation is a quasi-static process, the viscosity can be neglected. When both the strain rate and viscosity are prominent to generate shear stress comparable to pressure, the deviatoric behavior can't be omitted. We utilize the Equation of State (EOS) model to simulate the liquid core region. The EOS model relates the pressure to the volume of liquid domain in Linear USUP Hugoniot form described in equation (4.2), where the relation is governed by the bulk modulus that can be configured.

$$p = \frac{\rho_0 c_0^2 \eta}{(1 - s\eta)^2}\left(1 - \frac{\Gamma_0 \eta}{2}\right) + \Gamma_0 \rho_0 E_m \tag{4.2}$$

where p is the pressure, $\rho_0 c_0^2$ is the equivalent to the elastic bulk modulus K at small nominal strains (ρ_0 indicates the initial density and c_0 wave propagation speed), Γ_0 is a

material constant. c_0 and s define the linear relationship between the linear shock velocity, U_s, and the particle velocity, U_p, as $U_s = c_0 + sU_p$. s and Γ_0 are set to be 0 in the simulation. So the pressure is correlated to the nominal volumetric compressive strain η. The definition for the nominal volumetric compressive strain is stated as:

$$\eta = 1 - \frac{\rho_0}{\rho} \tag{4.3}$$

The EOS region as fluid core shall be first verified before put to use. As illustrated in Figure 4.5, the typical pressure and shear stress are extracted from 2D FEM test cases with small viscosity at different locations with the application of temperature field. Stress on the center is consistent with the stress on the fluid/solid interface, showing that fluid region exhibit uniform pressure and shear stress everywhere. The viscosity in the test cases is small (same as water), so we could observe that the shear stress is zero in around the liquid domain. We have also verified the stresses in 3D EOS models, and stresses comply with the results from 2D EOS models.

We have also tested another solid model using zero shear modulus and finite bulk modulus (referred as no-shear model) to describe the liquid core, but the no-shear solid failed to give results of uniform pressure and consistent shear stress. As a results, the no-shear model generally generates nonsymmetrical deformations and is then discarded in favor of EOS model.

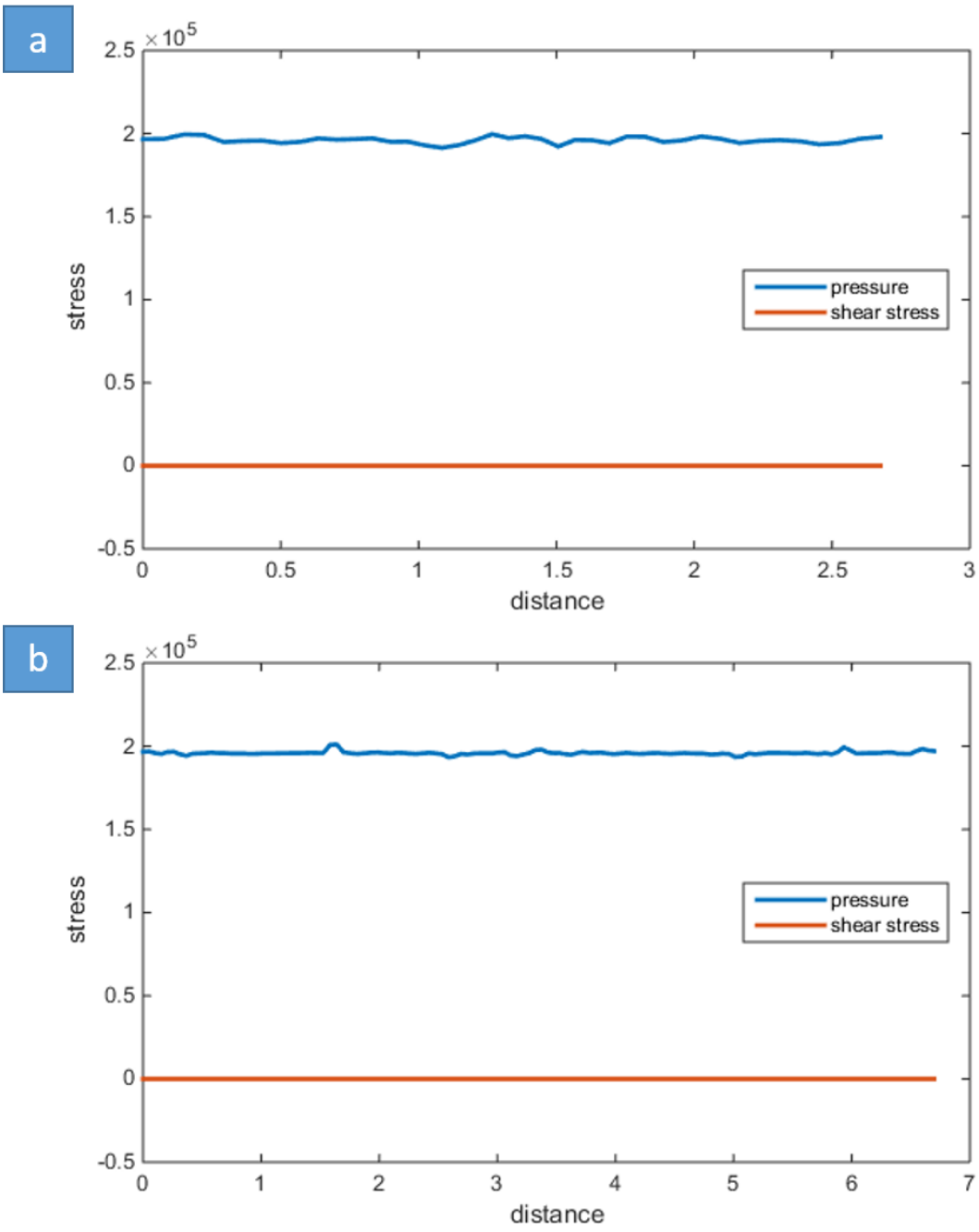

Figure 4.5 Typical pressure and shear stress in the 2D EOS liquid domain with small viscosity. a, stresses on the centerline; b, stresses on the solid/liquid interface

One thing to be noted is that when the viscosity is larger or the time scale is small, we could observe large shear stress which is comparable to pressure, and pressure is no longer uniform. Figure 4.5 only serves as an example under small viscosity circumstances.

4.4 Two dimensional solid shell/liquid core structure

4.4.1 Theoretical linear analysis of 2D solid shell/liquid core

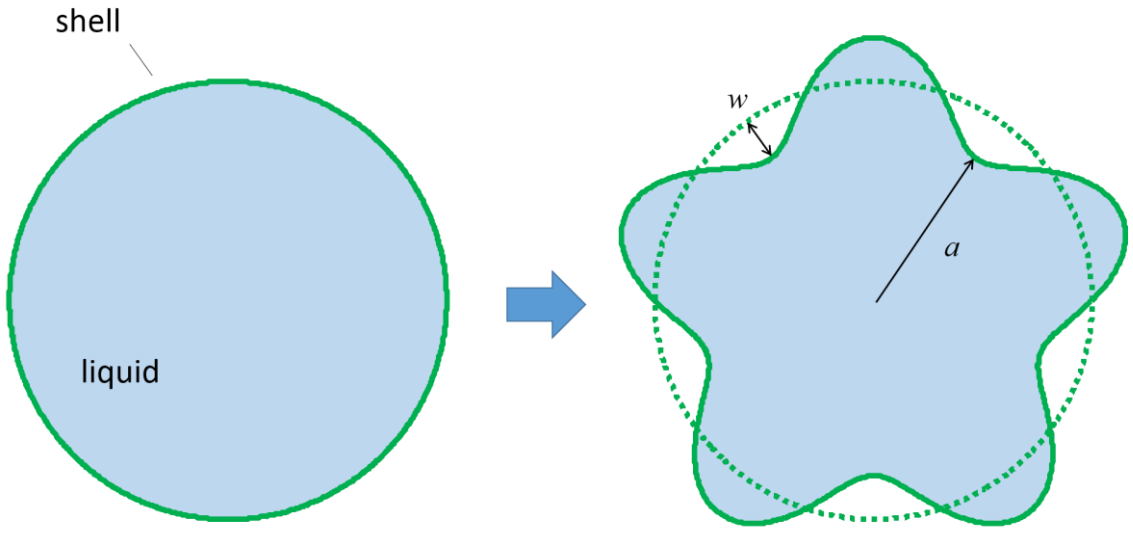

Figure 4.6 Original shape and deformed shape of 2D solid shell/liquid core model, radial displacement are notated as w, initial radius a.

For the sake of simplicity, we will start our linear analysis from 2D solid shell/liquid core system and expand the analysis to 3D system in following section. Researchers have stated that for spherical core/shell structure with very large radius, the results converge to corresponding planar structure [87]. So this two dimensional model is illustrative for the following three dimensional model, and can provide some parallel and inspirational information for the onset of buckling processes.

A representative two dimensional core shell model is illustrated in Figure 4.6. There are two components of shell displacement in cylindrical coordinates: radial displacement w, taken positive toward the center, and circumferential displacement v, taken

positive in the direction of increasing θ. These displacements are detailed in Figure 4.7 with the angles and arc length that will be used in the following analysis.

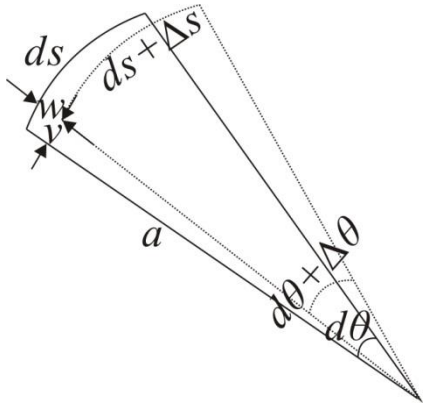

Figure 4.7 An infinitesimal radial section with opening angle $d\theta$, the radial displacement is w, circumferential displacement v, ds the arc length of solid shell.

For the buckling of liquid filled cylindrical shell there are three components of total energy E in the linear buckling analysis, the bending energy of shell U_b, the circumferential tensile/compressive energy of shell U_t, and the volumetric deformation energy of liquid domain U_v. The third term should have been the elastic energy from substrate [96] as compared to solid substrate. Since there is no shear stress in the liquid, elastic energy consists only of volumetric deformation energy.

$$E = U_b + U_t + U_v \tag{4.4}$$

The bending energy can be calculated as

$$U_b = \frac{1}{2D}\int M^2 ds \tag{4.5}$$

where D represents the bending stiffness of solid shell:

$$D = \frac{Eh^3}{12(1-v^2)} \tag{4.6}$$

Bending momentum M in (4.5) is proportional to the change of curvature:

$$M = D\left(\kappa - \frac{1}{a}\right) \tag{4.7}$$

where κ is the curvature of the cylindrical shell after deformation and $1/a$ the original curvature of solid shell with a denoting the initial radius. The curvature κ after buckling is:

$$\kappa = \frac{\varphi}{ds + \Delta s} \tag{4.8}$$

Here φ is the radial angle of the shell in the natural plane between distance ds after deformation, which consists of two components: the circumferential displacement v (rotation) and deflection displacement w (the change of tangent of arc).

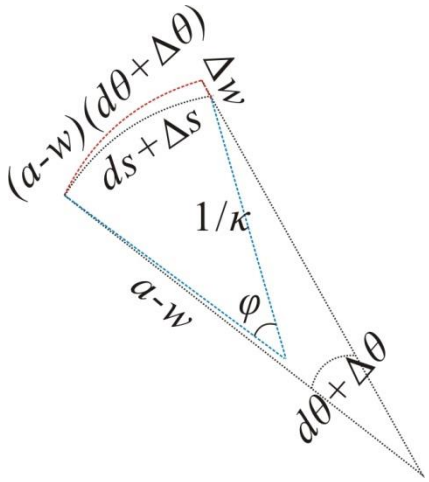

Figure 4.8 Illustration on how to calculate curvature of solid shell in 2D polar coordinates

The arc length after deformation is

$$ds + \Delta s = \sqrt{[(a - w)(d\theta + \Delta\theta)]^2 + \Delta w^2} \tag{4.9}$$

with

$$\Delta w = \frac{dw}{ds} ds \tag{4.10}$$

and

$$\Delta\theta = \frac{dv}{(a-w)ds}ds \tag{4.11}$$

So φ can be expressed as:

$$\varphi = d\theta + \Delta\theta + \frac{d^2w}{ds^2}ds = d\theta + \frac{dv}{(a-w)ds}ds + \frac{d^2w}{ds^2}ds \tag{4.12}$$

and then

$$\varphi = \left(1 + \frac{av'}{a-w} + aw''\right)d\theta \tag{4.13}$$

Note that

$$ds = ad\theta \tag{4.14}$$

Square root in equation (4.9) can be approximated in the following way:

$$ds + \Delta s \approx \left(a - w + av' + \frac{(w'a)^2}{2(a-w+av')}\right)d\theta \tag{4.15}$$

The circumferential tensile energy can be described as

$$U_t = \frac{Eh}{2(1-v^2)}\int \varepsilon^2 ds \tag{4.16}$$

in which the circumferential tensile strain ε can be calculate from (4.15):

$$\varepsilon = \frac{\Delta s}{ds} \approx -\frac{w}{a} + v' + \frac{aw'^2}{2(a-w+av')} \tag{4.17}$$

The volumetric deformation energy of the liquid domain is

$$\begin{aligned} U_v &= \frac{KV}{2}\left(\frac{\int \frac{(a-w)^2}{2}(d\theta + \Delta\theta) - V}{V} - \varepsilon_0\right)^2 \\ &= \frac{KV}{2}\left(\frac{\int \frac{(a-w)^2}{2}\left(1 + \frac{av'}{a-w}\right)d\theta - V}{V} - \varepsilon_0\right)^2 \end{aligned} \tag{4.18}$$

where $V = \frac{4}{3}\pi a^3$ is the original liquid volume and K is the bulk modulus of the liquid. ε_0 is the shrinking ratio of liquid due to leakage or evaporation.

We define the dimensionless displacement as $w_1 = w/a$ $(w_1 < 1)$, $v_1 = v/a$ and $dw/ds = dw_1/d\theta$, $dv/ds = dv_1/d\theta$. So the bending energy can be rewritten as:

$$U_b = \frac{D}{2}\int(\kappa - 1/a)^2 ds = \frac{D}{2a}\int\left(\frac{1+\frac{{v_1}'}{1-w_1}+{w_1}''}{1-w_1+v_1'+\frac{({w_1}')^2}{2(1-w_1+v_1')}}-1\right)^2 d\theta \tag{4.19}$$

where the derivations are defined as $w_1' = dw_1/d\theta$ and $v_1' = dv_1/d\theta$.

Also the circumferential tensile energy is:

$$\begin{aligned} U_t &= \frac{Eh}{2(1-v^2)}\int \varepsilon^2 ds = \frac{Eh}{2(1-v^2)}\int\left(-\frac{w}{a}+v'+\frac{aw'^2}{2(a-w+av')}\right)^2 ds \\ &= \frac{Eha}{2(1-v^2)}\int\left(-w_1+v_1'+\frac{({w_1}')^2}{2(1-w_1+v_1')}\right)^2 d\theta \end{aligned} \tag{4.20}$$

The volumetric deformation energy of liquid domain is

$$\begin{aligned} U_v &= \frac{K\pi a^2}{2}\left(\frac{\int\frac{(a-w)^2}{2}\left(1+\frac{av'}{a-w}\right)d\theta-\pi a^2}{\pi a^2}-\varepsilon_0\right)^2 \\ &= \frac{K\pi a^2}{2}\left(\frac{\int\frac{(1-w_1)^2}{2}\left(1+\frac{{v_1}'}{1-w_1}\right)d\theta-\pi}{\pi}-\varepsilon_0\right)^2 \end{aligned} \tag{4.21}$$

In order to simplify the notation, we can define two nondimensionalized coefficients:

$$\begin{aligned} A &= \frac{Eha/(1-v^2)}{D/a} = \frac{12a^2}{h^2} \\ B &= \frac{a^2K}{D/a} = \frac{12(1-v^2)Ka^3}{Eh^3} \end{aligned} \tag{4.22}$$

Therefore, the total energy *E* can be expressed as:

$$E = \frac{D}{2a}\left\{\int\left(\frac{1+\frac{{v_1}'}{1-w_1}+{w_1}''}{1-w_1+v_1'+\frac{({w_1}')^2}{2(1-w_1+v_1')}}-1\right)^2 d\theta\right.$$
$$+A\int\left(-w_1+v_1'+\frac{({w_1}')^2}{2(1-w_1+v_1')}\right)^2 d\theta \qquad (4.23)$$
$$\left.+B\pi\left(\frac{\int\frac{(1-w_1)^2}{2}\left(1+\frac{{v_1}'}{1-w_1}\right)d\theta-\pi}{\pi}-\varepsilon_0\right)^2\right\}$$

As seen in (4.23), the variation of E is correlated to w_1 and v_1. Starting from this, we can obtain the equilibrium equations for the liquid filled solid shell. For a typical sample in our study the thickness is very small compared to the radius, *i.e.* $a/h \sim 100$ in our case. A very small bending stiffness means the shell tends to bend rather than stretch [75], other literatures also state the principle of inextensionality when studying the buckling of empty solid shell [34]. As the stretching energy (4.20) becomes zero, the term in the parenthesis should be zero;

$$-w_1+v_1'+\frac{({w_1}')^2}{2(1-w_1+v_1')}=0 \qquad (4.24)$$

We assume the radial displacement w_1 takes the form described in [34] which is consistent with the perturbation technique [96]:

$$w_1 = w_0 + a_n\cos n\theta$$
$$(4.25)$$
$${v_1}' = b_n\cos n\theta$$

With the linear buckling analysis, we assume small perturbation with $w_1 << 1$. Substitute (4.25) back into (4.24) and take θ as 0, we obtain the relation between parameters:

$$w_0 + a_n = b_n \tag{4.26}$$

Using equation (4.24), (4.25) and (4.26), the total energy in (4.23) could be deduced to:

$$\begin{aligned} E = \frac{D}{2a}\Big\{&\pi[w_0^2 + 2(1-n^2)w_0 a_n + (1-n^2)^2 a_n^2] \\ &+ B\pi\left(4w_0^2 - 4w_0^3 + 2w_0^2 a_n + 4w_0\varepsilon_0 + w_0^4 - w_0^3 a_n - 2w_0^2\varepsilon_0\right. \\ &\left.+ \frac{1}{4}w_0^2 a_n^2 + w_0\varepsilon_0 a_n + \varepsilon_0^2\right)\Big\} \end{aligned} \tag{4.27}$$

According to the minimization of total energy, we have two derivatives equal to zero $\partial E/\partial a_n = 0$ and $\partial E/\partial w_0 = 0$. Therefore, we arrive at:

$$2a_n(1-n^2)^2 + 2(1-n^2)w_0 + 2Bw_0^2 - Bw_0^3 + \frac{B}{2}w_0^2 a_n + Bw_0\varepsilon_0 = 0 \tag{4.28}$$

and

$$\begin{aligned} &2w_0 + 2(1-n^2)a_n + 8Bw_0 - 12Bw_0^2 + 4Ba_n w_0 + 4B\varepsilon_0 + 4Bw_0^3 \\ &- 3Ba_n w_0^2 - 4Bw_0\varepsilon_0 + \frac{B}{2}w_0 a_n^2 + Ba_n\varepsilon_0 = 0 \end{aligned} \tag{4.29}$$

Neglect the higher order terms with $w_1 \ll 1$, equation (4.28) and (4.29) can be approximated into the following equation:

$$a_n = \left(\frac{1}{n^2-1} - \frac{B\varepsilon_0}{2(1-n^2)^2}\right)w_0 \tag{4.30}$$

and

$$w_0 = \frac{8(1-n^2)^2\varepsilon_0}{B\varepsilon_0^2 + 2\varepsilon_0(1-n^2) - 16(1-n^2)^2 + 8(1-n^2)^2\varepsilon_0} \tag{4.31}$$

We could observe from equation (4.27) that $n = 2$ is corresponding to the minimum total energy ($n = 1$ represents the translation of the total structure as a rigid body). And we could also deduce the critical shrinking ratio when the solid ring becomes unstable from

the original circular shape: $\varepsilon_0 = 2(n^2 - 1)/B$.

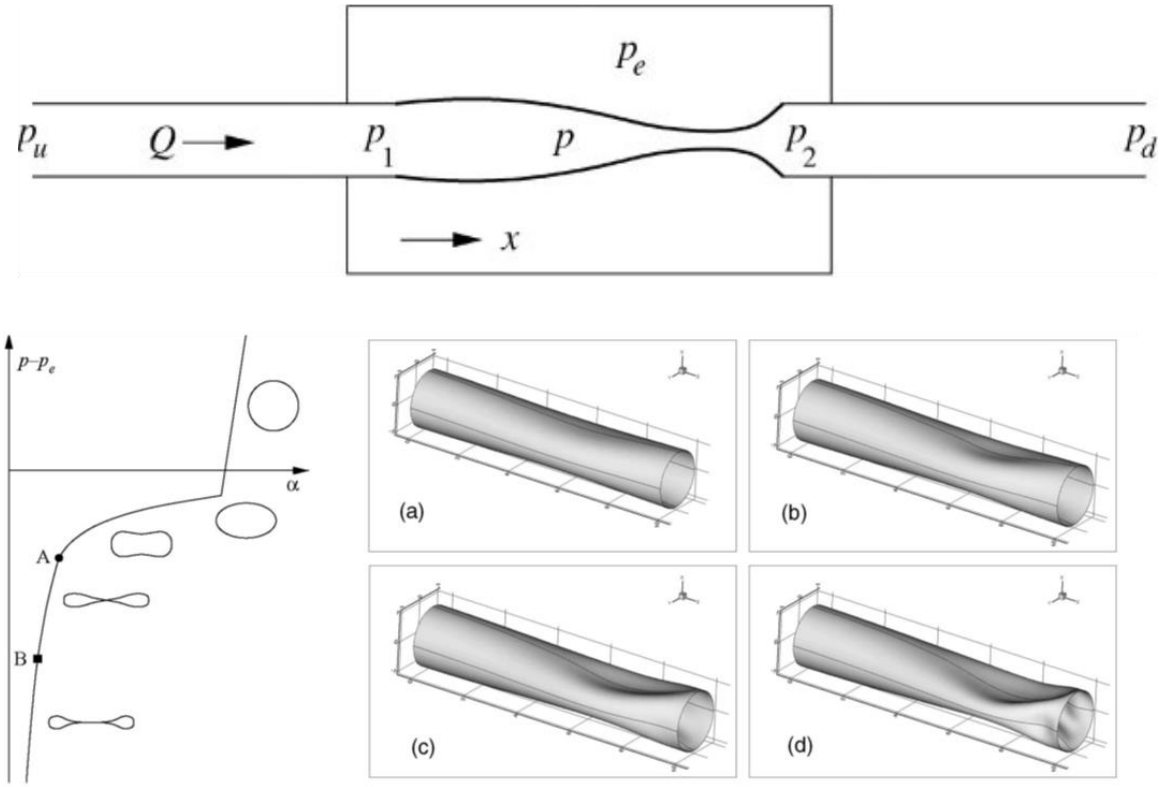

Figure 4.9 The buckling of flexible tube filled with liquid under compression, from reference [116]. The system configuration is explained in the top plot with indication of pressure at different location. The XY plots on the left shows the deformation pattern for the cross section. External pressure increases from (a) to (d) on the right four panels

Our theory is also in accordance with the previous study of flexible tube filled with liquid such as human veins [116], depicted in Figure 4.9. The positive pressure difference between the outside and the inside P_e - P causes the collapse of the elastic tube, and cross section at the onset of buckling is the same with the shape of $n = 2$ in theoretical analysis. The post buckling shape indicates that there is point contact and line contact for the solid shell for very large pressure difference, but this behavior is out of our research category for now.

4.4.2 Finite element simulation of two dimensional solid shell liquid core structure

We have shown analytically that minimum energy state is associated with $n = 2$ using the linear perturbation theory, consequently the deformed shapes under different circumstances would converge to $n = 2$ scenario. Linear theory is proven effective on predicting the onset of buckling which is elliptical shape, but the following deformation processes enter the nonlinear regime which is difficult for the theoretical analysis. Therefore, FEM models are setup to determine the nonlinear deformation.

By employing the liquid model described in section 4.3, the 2D solid shell/liquid core system is simulated in the FEM software ABAQUS. The substrate is meshed by over 1600 linear quadrilateral plane strain elements (EOS can be represented by regular solid elements) and the shell is represented by 4 layers of more than 500 linear quadrilateral plain strain elements with reduced integration to account for large rotation. In all cases, the mesh density is validated from mesh convergence studies. When using EOS model, the meshes in liquid domain get distorted easily when the viscosity is small as nodes at the interior of liquid have little constraints compared to the bonded liquid boundaries, so Arbitrary Lagrangian Eulerian (ALE) remeshing scheme in the ABAQUS solver is needed regularly to ensure the good condition of meshes. Generally speaking, remeshing are necessary for the Lagrangian FEM simulation for liquid domain. (ABAQUS automatically assume sliding boundary condition for the ALE remeshing scheme).

A temperature field is imposed on the shell as well as core to simulate the loading process. The thermal expanding coefficient of solid shell is much larger than that of core (thermal expansion coefficient of core is set to be 0 in the simulations), while the shell and core remain perfectly bonded. Therefore, the solid shell undergoes compressive stress and eventually buckles to release the compressive stress. The shrinking of liquid domain as the activating force is not easily implemented in ABAQUS, so expanding of solid shell is used instead which is proved to be equivalent with the liquid shrinking scheme [68].

Since we impose the load on the 2D core/shell structure by applying temperature field on it, we need to calculate the compressive stress in the solid shell at certain temperature through the following equation assuming there is no actual deformation on the core shell structure:

$$\sigma_{\phi\phi} = -\frac{E\alpha T}{1-2\nu} \tag{4.32}$$

Where $\sigma_{\phi\phi}$ represents hoop stress in solid shell, E Young's modulus of solid shell, α thermal expansion coefficient of shell, ν Poisson's ratio and T the temperature. So we can examine the evolution history of 2D solid shell liquid core system at different stress level.

Based on the experience of solids core solid shell structures [96], a series of models with different geometry parameter R/t and material parameter E_f/E_s are studied, where R indicates the radius of liquid core, t the thickness of solid shell, E_f the Young's modulus of solid shell and E_s bulk modulus of water explained in equation (4.2). We find that they all exhibit similar deformation pattern of peanut shape in Figure 4.10 as the

compressive stress/strain in solid shell increases. As a result, we choose a representative model with $R/t = 10$ and $E_f/E_s = 1$ as our main studying object in this section.

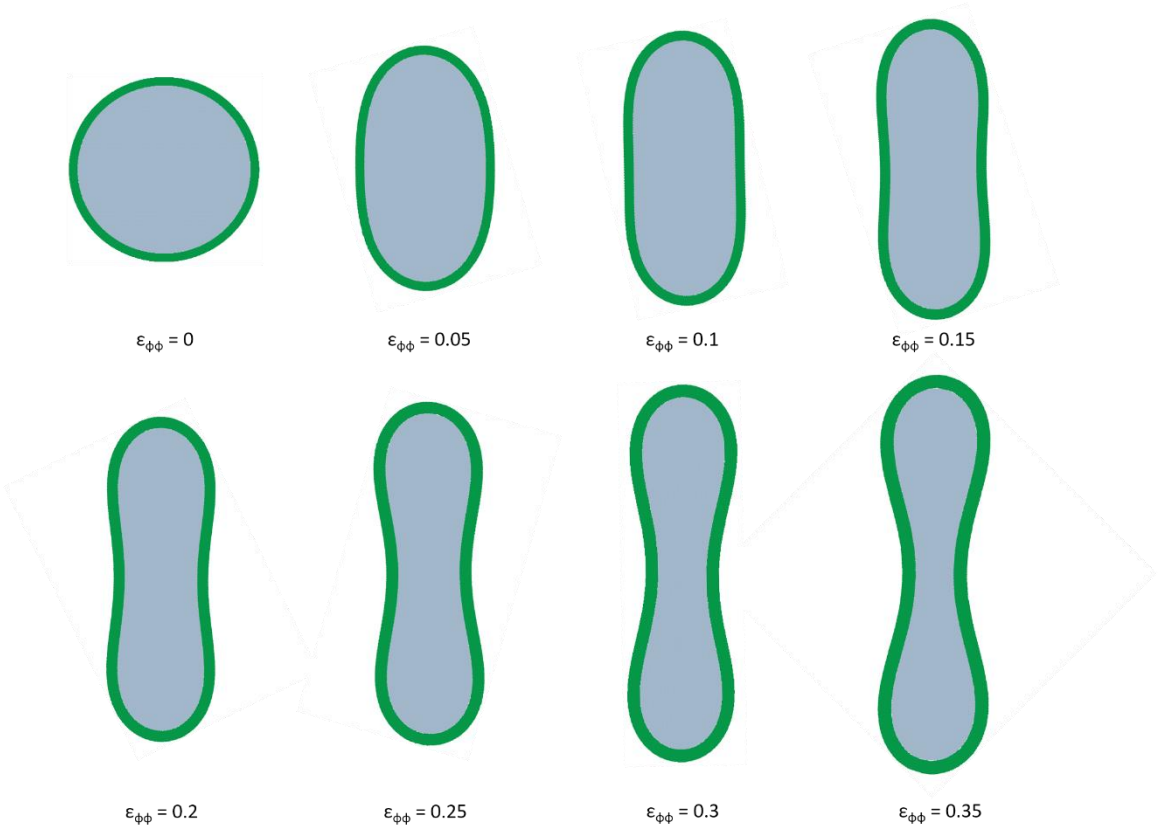

Figure 4.10 The evolution of 2D solid shell liquid core structure with viscosity of 10^{-3} Pa·s, radius of core 0.01 m, density of core 10^3 kg/m^3 and time scale 1 s. The hoop strain in solid shell is given under each shape.

The evolution of a typical peanut shape is documented in Figure 4.10. These shape are developed from original buckling shape of $n = 2$ as indicated as $\sigma_{\phi\phi} = 0.05$. The critical compressive hoop stress for the model is around 0.13×10^8 Pa (corresponding to hoop strain of 0.0026), so we are observing the shapes which are well beyond the buckling threshold, while in the solid shell solid core system only shapes slightly above buckling threshold are reported [62, 96]. The peanut shape can be characterized by the ratio of long axis to original

diameter d_0 and the ratio of short axis to original diameter d_0. The overall trend for the structure is that the peanut shape becomes flatter as the compressive stress in solid shell increases, seen in Figure 4.11. The volume of the liquid region is almost constant since the bulk modulus is much larger than the bending stiffness of solid shell, and we impose the loading on solid shell instead of liquid core.

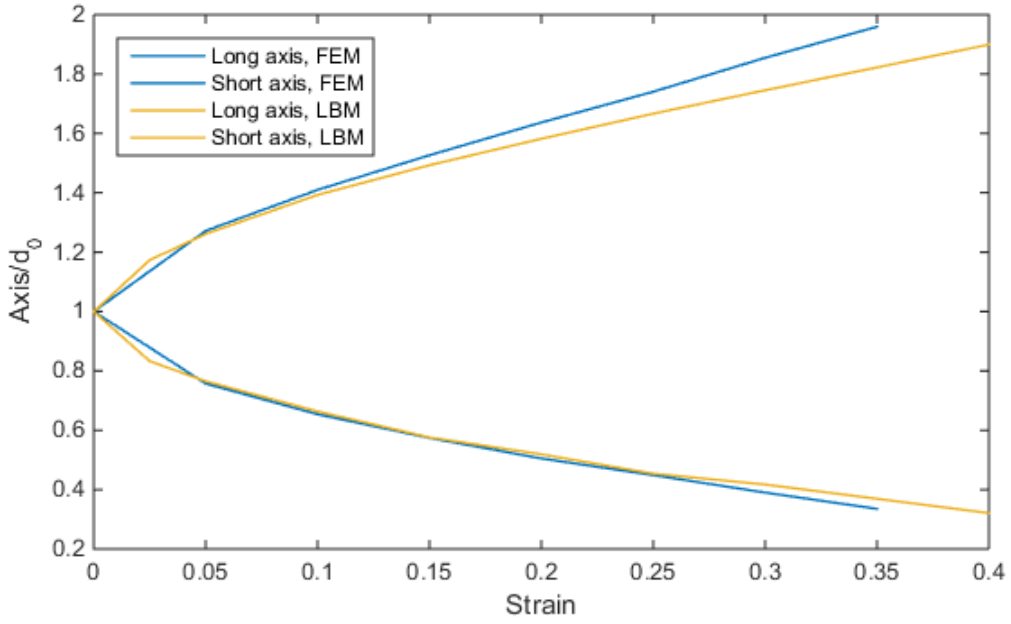

Figure 4.11 Long axis / d0 and short axis / d0 in the deformation process of Figure 4.10, compared with simulation results from Lattice Boltzmann Method simulations

In addition to the models represented in Figure 4.10, we also observe another series of deformation where intermediate irregular shape appears before eventual advent of peanut shape, as depicted in Figure 4.12. We call this intermediate shape amorphous shape since the shape lacks symmetry compared to peanut shape in Figure 4.10, and it is difficult to characterize using wave number and wave length as the ordered shape.

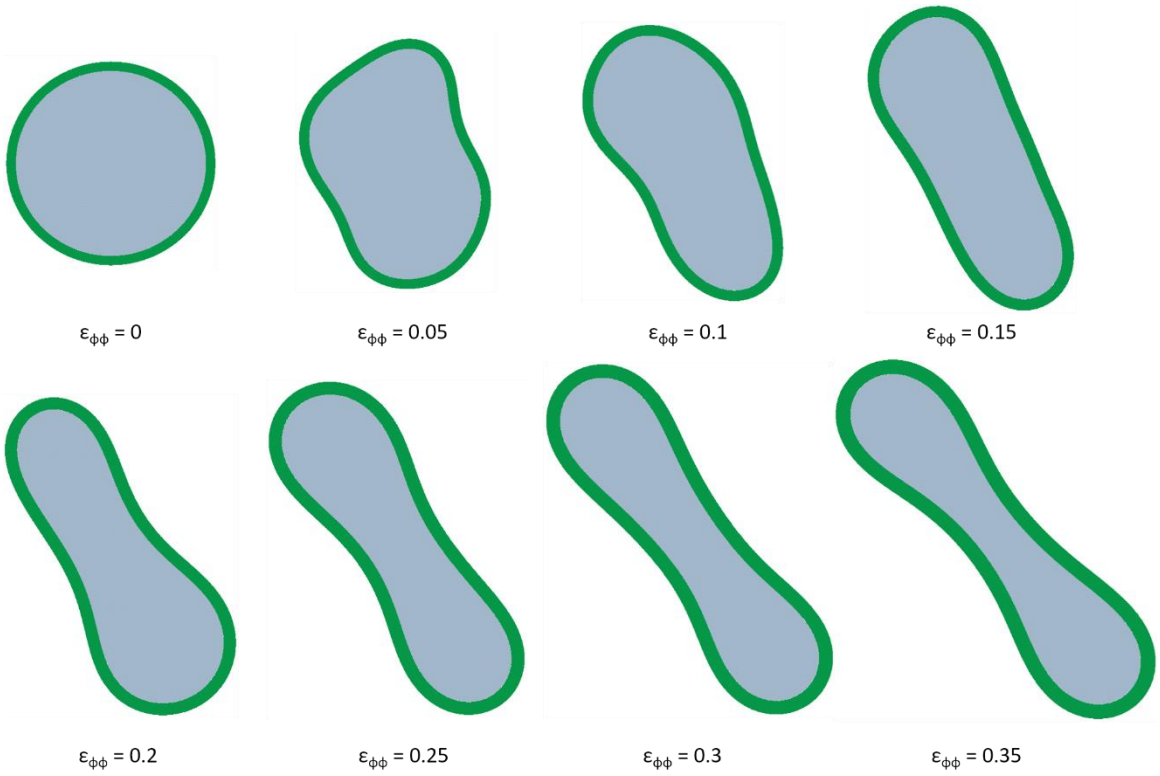

Figure 4.12 The evolution of 2D solid shell liquid core structure with viscosity of 10^{-3} Pa·s, radius of core 0.1 m, density of core 10^4 kg/m^3 and time scale 1 s. The hoop strain in solid shell is given under each shape.

One stark contrast between liquid core system and solid core system is that liquid core system (including peanut shape and amorphous shape) can't generate ordered gear-like deformation as the solid core system does. According to literature [62, 96], the buckling wave number for solid core solid shell system can be predicted by the relation $n_r \approx \left(\frac{R}{t}\right)^{3/4}\left(\frac{12\overline{E_s}}{\overline{E_f}}\right)^{1/4}$, where R represents radius of solid core, t thickness of solid shell, $\overline{E_f}$ and $\overline{E_s}$ the equivalent Young's moduli of shell and core respectively. The small scale deformations on the solid shell for gear-like deformation induce large curvature and consequent large bending energy, which requires large compatible strain energy in the core domain. Liquid domain can't produce large strain energy since the energy only comes from

volumetric change, and the small shear stress has little contribution to the total strain energy.

In an attempt to generate gear-like structure for the liquid core system, we resort to increase the shear stress in the liquid domain. Shear stress can be adjusted by changing viscosity and time scale, since shear stress is the produce of viscosity and shear strain rate. We use the ratio between shear stress and pressure to represent the process changing from liquid core to solid-like core. As shown in Figure 4.13, viscosity increases from a tiny portion of pressure to a value compared to pressure by using a larger viscosity and small time scale.

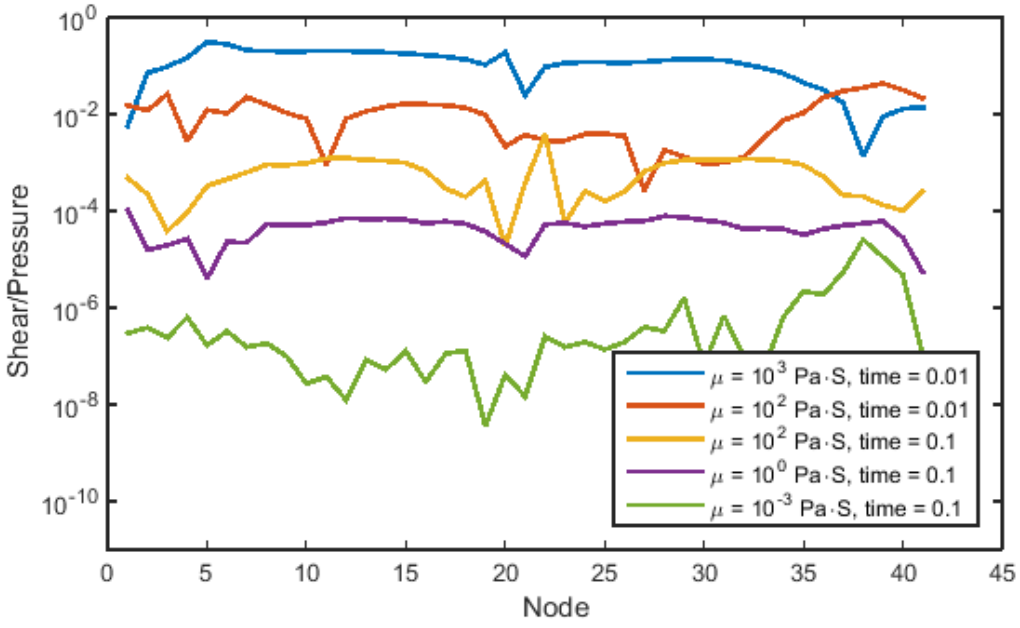

Figure 4.13 Increasing the shear stress in liquid region by increasing viscosity and decreasing time scale

In order to characterize the increase of pressure relative to shear stress, we propose a dimensionless parameter $K\tau/\mu$ for the liquid core, where K indicates the bulk modulus, τ time scale and μ dynamical viscosity for liquid. Increasing viscosity μ and decreasing time

scale τ in Figure 4.13 corresponds to a smaller $K\tau/\mu$. Figure 4.14 shows the pattern evolution with increasing hoop strain for different $K\tau/\mu$. Therefore, larger value of $K\tau/\mu$ implies cases with smaller shear stress compared to pressure, the shapes converge to peanut shape at early stage of evolution. Smaller value of $K\tau/\mu$ implied an intermediate state between solid and liquid. Although the shapes eventually transit to peanut shape, we could observe some amorphous shapes before the final transition. What's more interesting is we can even observe ordered gear-like pattern in a small window (highlighted in red rectangle) in the left low side of Figure 4.14. This gear-like state exists shortly before entering the amorphous state and later peanut state.

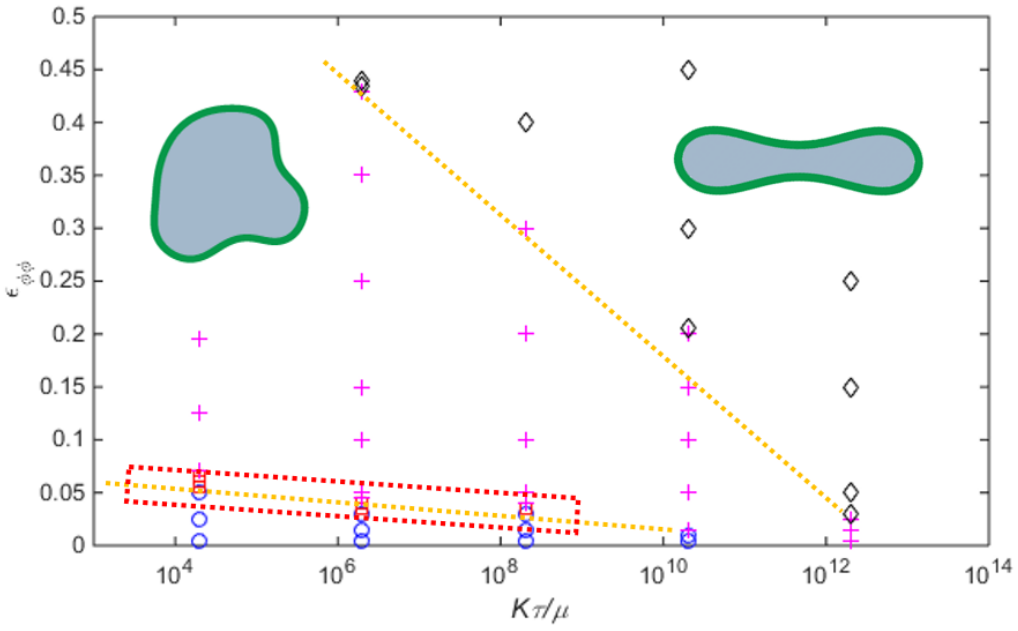

Figure 4.14 Deformation map for 2D liquid core solid shell structure with varying $K\tau/\mu$ and $\varepsilon_{\phi\phi}$, with ◊ indicating peanut shape, □ indicating the ordered gear-like shape (highlighted in read rectangle), + indicating amorphous shape, ○ indicating steady circular shape

Since we increase the shear stress in liquid core by decreasing the time scale, we

are encountering a problem that the simulation is no longer a quasi-static process, and the dynamic effect has to be considered, inertia also plays important role at this regime. Similar to Reynolds number in fluid mechanics, we propose a similar dimensionless parameter $\rho R^2/\mu\tau$ to describe the ratio between inertia and shear in liquid core, where ρ is the density and R is the radius of liquid core. Therefore, increasing density and size of liquid induces a larger inertia compared to shear.

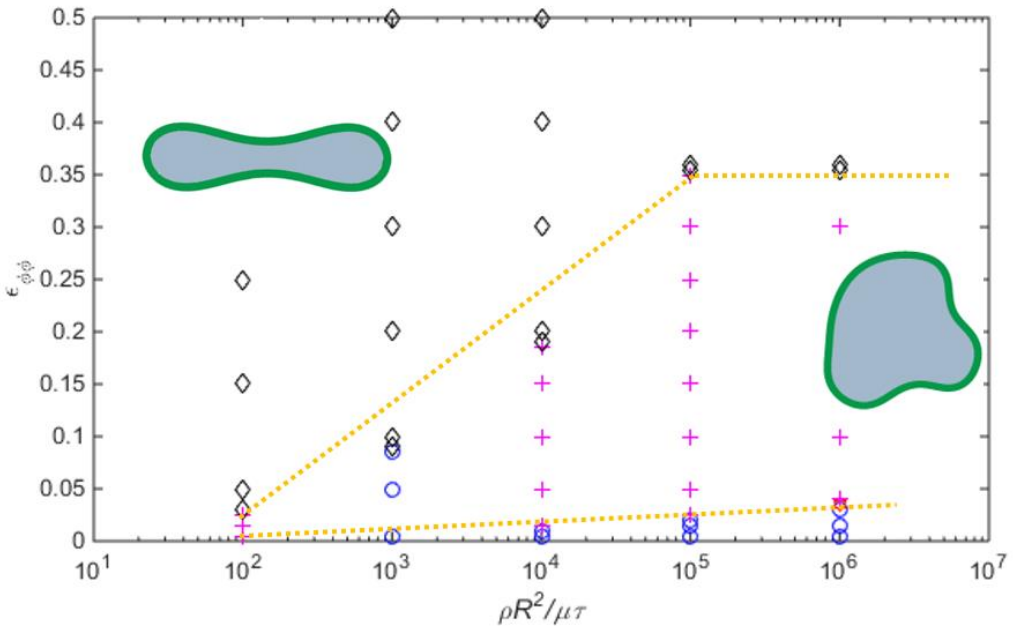

Figure 4.15 Deformation map for 2D liquid core solid shell structure with varying $\rho R^2/\mu\tau$ and $\varepsilon_{\phi\phi}$, with ◊ indicating peanut shape, □ indicating the ordered gear-like shape, + indicating amorphous shape, ○ indicating steady circular shape

Figure 4.15 shows the pattern evolution with increasing hoop strain $\varepsilon_{\phi\phi}$ for different $\rho R^2/\mu\tau$. When the inertia is small, core shell structure transit to peanut shape immediately, skipping the amorphous stage. When the inertia is large, amorphous shape stays before peanut shape, and the window for amorphous state expands as the inertia

increases. Amorphous state is more prominent for larger inertia because inertia in solid shell will introduce dynamic effects and consequential asymmetries in the model. The dynamic effects will damp out eventually, and the core shell structure will settle down to the final peanut shape.

For the theoretical analyses in section 4.4.1 about static or quasi-static process, they are corresponding to regions where time scale is large enough, *i.e.* far right in Figure 4.14 and far left in Figure 4.15. Large time scale means that deformations always converge to peanut shape regardless of other parameters, which is also consistent with theoretical analysis.

In summary, we analysis the 2D solid shell liquid core structure theoretically and numerically in this section. We observe that liquid core system can't generate ordered gear-like deformation pattern as the solid core system does, instead the liquid core system converges to peanut shape as the loading process proceeds. An intermediate amorphous shape is observed between the initial circular shape and final peanut shape, and the shear stress together with inertia will affect the transition between initial circular state and final peanut state.

4.5 Three dimensional solid shell liquid core structure

The theoretical analysis for 3D solid shell liquid core structure is more difficult compared to 2D structure, so we only study the problem through simulations in FEM

software ABAQUS. Again, the liquid core is simulated by the EOS model as described in last section. The substrate is meshed by over 260,000 hexahedron solid elements (EOS can be represented by regular solid elements) and the shell is represented by over 270,000 hexahedron solid elements with reduced integration to account for large rotation. There are a least four layers of element in the solid shell to ensure the accuracy. In all cases, the mesh density is validated from mesh convergence studies.

Using the same loading method and the same remeshing scheme for EOS region as what we did in 2D model, we have built a series of 3D solid shell liquid core models with different material properties and geometrical properties. We can use the same equation (4.32) to estimate the hoop stress in the solid shell. Since we are dealing with initial spherical shape, the longitudinal stress is equal to hoop stress [62].

Because we are dealing with liquid model of viscosity, dynamic effect should be considered at small time scale as discussed in 2D cases. Therefore, deformation shape shows different pattern at different time scale. Deformation shapes for model with R/t =10 and E_f/E_s = 1 under different strain loading rate are illustrated in Figure 4.16, all of the shapes are plotted at the same hoop stress. Large strain loading rate 0.5/0.01s induces small scale protruding hills on the shell surface, which looks similar to convex pattern in Figure 4.4. However, small hills in Figure 4.4 are separated from each other while hills are interconnected in Figure 4.16. We will make another efforts to explain the intrigue pattern in Figure 4.4 in section 5.2.3 using another set of theory and simulations. On the contrary,

the small loading rate induces concave patterns that are like punched sandbag. Deformation pattern for strain loading rate 0.5/1s seems interchangeable with that of 0.5/10s, which means 0.5/1s case already enters quasi-static regime. Therefore, we will study 0.5/1s case as a representation in the following analysis. For all of the model with different loading rate, only the fastest loading cases show convex pattern, which is maybe due to the inertia in the solid shell and increase of shear stress in the liquid core as discussed in 2D cases.

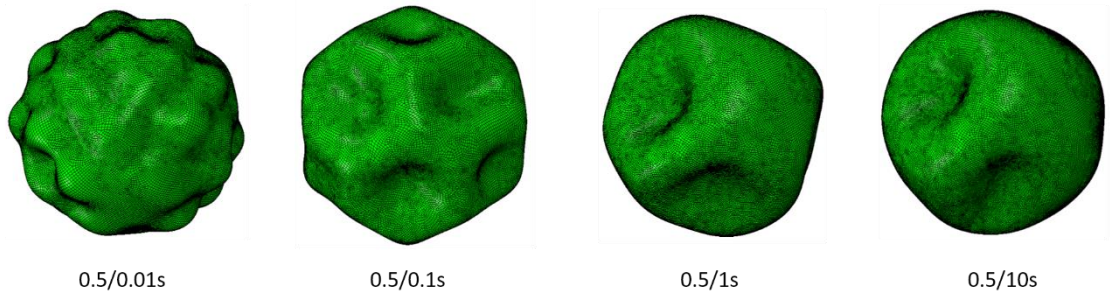

Figure 4.16 Deformation pattern for different strain loading rate for 3D solid shell liquid core model of R/t =10 and E_f/E_s =1

At the same hoop stress in the solid shell, we compile the deformation patterns for different E_f/E_s and R/t at two strain loading rates, 0.5/0.01s as the large loading rate and 0.5/1s as the small loading rate. Figure 4.17 illustrates the pattern map for large loading rate. Models with smaller R/t have larger critical buckling strain, so we choose deformation shapes at different strain in Figure 4.17, *i.e.* strain of 0.25 for $R/t = 10$, strain of 0.15 for $R/t = 20$ and strain of 0.1 for $R/t = 40$ & $R/t = 50$. The thinnest solid shell we have tested is $R/t = 100$, but the model is not stable with nonsymmetrical deformation, so $R/t = 100$ is not include in the following study.

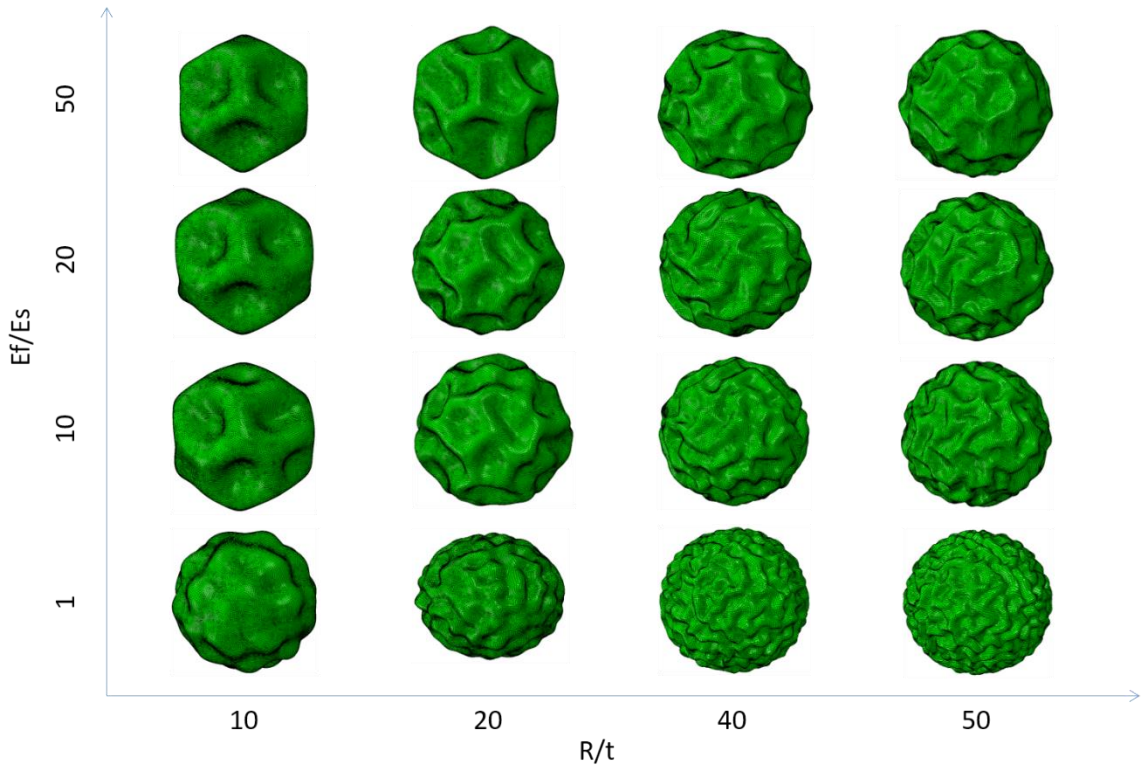

Figure 4.17 Deformation patterns for varying R/t and E_f/E_s at strain of 0.25 for R/t = 10, strain of 0.15 for R/t = 20 and strain of 0.1 for R/t = 40 & R/t = 50. Large strain loading rate 0.5/0.01s

The length scale of the deformed structure is related to the bending stiffness of solid shell $D = \frac{Eh^3}{12(1-\nu^2)}$ in equation (4.6) and its consequent bending energy in equation (4.5), which is dependent on Young's modulus as well as thickness of shell. Therefore, models with smaller bending stiffness, *i.e.* right lower region in Figure 4.17 such as model of R/t = 50 and E_f/E_s = 1, can generate finer structure compared to models with larger bending stiffness, *i.e.* left upper region in Figure 4.17 such as model of R/t = 20 and E_f/E_s = 50. Smaller bending energy also means smaller energy penalty for deformation, so shell is easier to bend at right lower region. The deformation pattern for smaller bending stiffness, however, resemble the herringbone shape for the solid shell solid core system in planer

structure as well as in spherical structure [74, 87]. As explained in last section, smaller time scale introduces considerable shear stress to the liquid core, so the liquid core exhibits solid-like behaviors. For thin solid shell models with R/t = 40 and R/t =50, the wave length of herringbone pattern increase as the Young's modulus increases, similar to the trend in literature [62, 87]. On the contrary, larger bending stiffness region shows the concave pattern similar to that in Figure 4.3a, although it shows more solid-like properties compared to shapes in Figure 4.18.

In contrast to Figure 4.17, Figure 4.18 summarize the deformation pattern for varying R/t and E_f/E_s at small loading rate, which can be considered as static or quasi-static loading cases. The prominent deformation shape is the single concave region on the spherical surface, similar to theoretical predication of empty solid shell in book [94]. When the bending stiffness is small, such as the model of R/t = 50 and E_f/E_s = 10, we could observe very sharp edge and transition points on the periphery of concave shape. On the contrary, there is only round edge on the periphery of concave shape for relative larger bending stiffness such as the model of R/t = 20 and E_f/E_s = 50. Even smaller bending stiffness, such as model of R/t = 50 and E_f/E_s = 1 and model of R/t = 40 and E_f/E_s = 1, can generate two major concave shapes on the whole spherical surface. Models with large bending stiffness, such as the models in the column of R/t = 10, generate several small scale concave patterns.

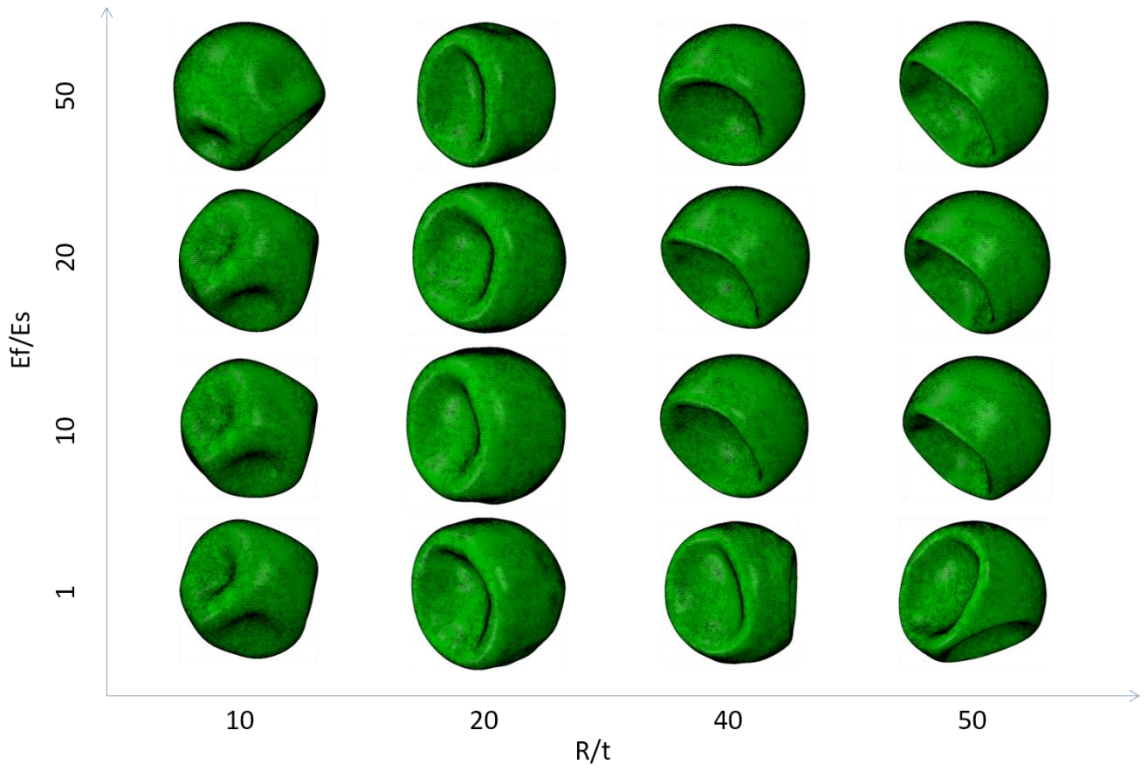

Figure 4.18 Deformation patterns for varying R/t and E_f/E_s at strain of 0.08. Small strain loading rate 0.5/1s

Upon close observation, the concave shape shows polygonal edges, a secondary buckling phenomena after the initial symmetrical pattern, similar to deflating beach ball [92] and beach ball on which a point force is applied [91]. The concave shape induces compressive stress on the inside of the rim, but tensile stress on the outside of the rim. The initial circular edge then losses it stability as the compressive stress exceed the critical stress for the circular rim. Our 5 edges in the polygonal pattern is close the prediction in literature [92] which states that number of edge is approximately $\sqrt{R/t} \approx 6$.

4.6 Conclusion and further discussion

In this chapter, we studied the buckling and post buckling deformation of solid

shell filled with liquid core both in two dimension and three dimension. We proposed a new material model to simulate liquid core, which can be fully integrated to the framework of solid mechanics. We then proceeded with this new model in the FEM software ABAQUS and obtained qualitative and quantitative results for the buckling process of solid shell liquid core system. A series of parameters are examined to reveal their effects on the buckling process, such as the strain in solid core, thickness of solid shell, the shear stress and inertia in liquid core, the modulus of liquid core.

We first perform a linear stability analysis for the 2D solid shell liquid core system. After calculating the elastic energy of the core shell structure, we determine that $n = 2$ is corresponding to the lowest energy among other value of n. Therefore, the initial circular 2D structure will transit to elliptical shape at the moment of buckling. Then subsequent post-bulking shapes are studied using FEM simulation. Different 2D solid shell liquid core models converge to peanut shape eventually, as Figure 4.10 and Figure 4.12 shows. But based on two dimensionless parameters $K\tau/\mu$ and $\rho R^2/\mu\tau$, models at different loading strain may exhibit amorphous asymmetrical shape before the final peanut shape, as summarized in Figure 4.14 and Figure 4.15. Models with large shear stress and large inertia will show amorphous shape and even temporary ordered gear-like shape.

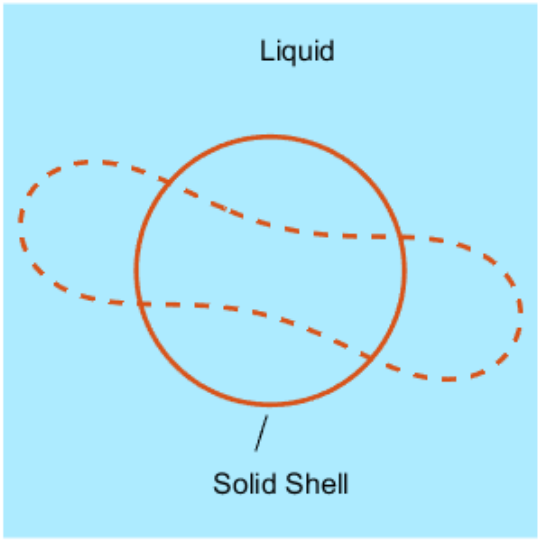

Figure 4.19 Solid shell liquid core model for Lattice Boltzmann Method simulation with immersed boundary method. Light blue region represents liquid region, and solid orange line represents initial circular solid shell, dashed orange line presents deformed solid shell

The 2D peanut shape is compared to results calculated from Lattice Boltzmann Method (LBM) simulation which is a collaboration with another colleague in our lab. As illustrated in Figure 4.19, the whole computational domain (light blue region) is marked as liquid, with only the red circle are marked as solid. The liquid domain is calculated using standard LBM formulation, while the velocity on the solid shell is set to be the same with surround liquid both in the shell and out of the shell. The solid shell is essentially a curve without thickness in the liquid environment, but the elastic energy for the solid shell is calculated by summering bending energy and tensile energy using the same parameters in FEM simulations. Total length and curvature for the solid shell shall be monitored for the calculation of elastic energy. The whole system is then evolving based on the principle of

energy minimization, after a certain initial strain is introduced to the solid shell as activating mechanism. Therefore, the LBM simulation represents the shape at equilibrium state. This scheme is called immersed boundary method [117, 118], and it is extremely useful for the Fluid Solid Interaction simulations.

Axis lengths for the 2D peanut shape from LBM simulation are compared with that from FEM simulation in Figure 4.11. We could observe that general trend for the peanut shape evolution in FEM agrees well with the trend in LBM, especially for the short axis. However, a discrepancy on the long axis between the two simulations, and the discrepancy is increasing as the strain in solid shell increases. The discrepancy indicates that there is certain degree of dynamic effect in the FEM simulations, so it is reasonable to check the inertia in simulation for 2D cases as well as 3D cases.

We then employ the same method in FEM simulations of 3D solid shell liquid core structure as 2D cases. Similar to 2D models, the deformation patterns are dependent on the loading rate and consequently inertia. For large strain loading rate of 0.5/0.01s shown in Figure 4.17, the liquid core model generates deformations similar to solid core structure, *i.e.* herringbone pattern for small bending stiffness of solid shell which is determine by equation $\frac{Eh^3}{12(1-v^2)}$. For the small strain loading rate of 0.5/1s shown in Figure 4.18, the liquid core model generate deformation similar to empty solid shell, *i.e.* large concave pattern on the spherical surface. The 3D LBM case are still under studying, and the results from LBM should be compared to that from FEM in 3D.

As we have demonstrated both in 2D cases and 3D cases, liquid core system can't generate ordered structures as the solid core system does, *i.e.* gear-like pattern in 2D and herringbone pattern in 3D. It is due to the fact that liquid core only poses bulk modulus but no shear modulus when it is a static or quasi-static process. Therefore, by increasing the loading rate or viscosity and consequent large shear stress, we can manage to generate ordered structure of liquid core system as the solid core system does in literature.

For solid shell solid core structure [96], the plain strain 2D model has been proved effective in predicting the critical buckling wave length and critical stress for 3D cylindrical model and prolate spheroidal system, serving as the cross section of long 3D structure. In our cases, we only consider the spherical shape in 3D geometry, so the peanut shape in 2D cases can't serve as a basis when considering 3D spherical shape.

Our simulations can also find verification in literatures, as researchers have done relevant experiments with solid shell filled with water in the surrounding liquid environment [99]. Due to osmosis from the core to the surrounding liquid, the amount of water decreases and initiates buckling process as illustrate in Figure 4.20. The major concave pattern has been capture by that in Figure 4.18, although the simulations fail to reach the final exhausted stage on the right most of Figure 4.20 due to the extremely large deformation.

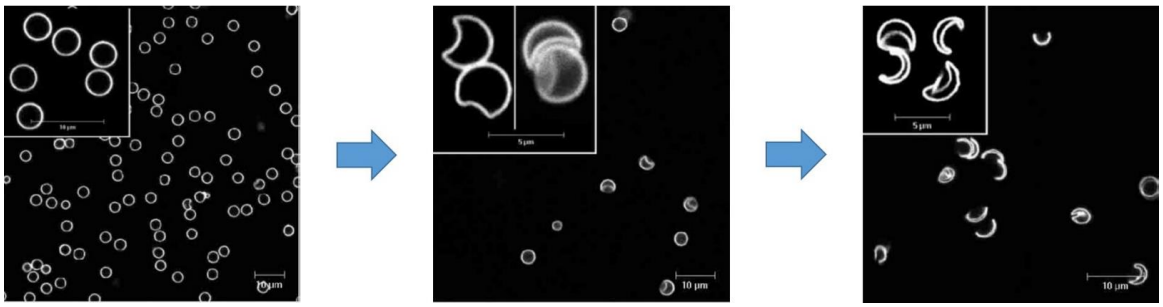

Figure 4.20 Buckling of 3D solid shell liquid core structure, due to osmosis from liquid core through solid shell to surrounding liquid [99]

Researcher have long simulated cells [119, 120], as well as cell nucleus [104, 106, 107], using liquid core model. Viscosity can also be added to the liquid core since cell usually possess a cytoskeleton protein network which provides shear resistance, and nucleoplasm also shows viscosity during the experiments. So our model can be useful by relating the cell morphology to the age or disease of cell, with the further inclusion of parameters that are relevant in real biological experiments.

Chapter 5.Conclusion and Prospect

5.1 Concluding remarks

We have studied three small subjects in the realm of continuum mechanics: imbibition in fluid mechanics, beam/rod buckling in solid mechanics and shell buckling at the solid/liquid interface.

In chapter 2, we examined the radial imbibition into a homogenous semi-infinite porous material from a point source with infinite liquid supply. We proved that in the absence of gravity (or in the regime while gravity is negligible compared to surface tension), the shape of the wet area is a hemisphere, and the radius of the wet area is related to time $r \sim t^{1/3}$ (equation (2.12) to be exactly). This new law with respect to time has been verified by FEM simulation in software COMSOL and a series of carefully designed experiments using packed glass microsphere as the porous media. We also found that as the imbibition slows down, the flow rate through the point source remains constant which is predicted by equation (2.13). This new result for three dimensional radial imbibition complements the classic Lucas-Washburn law in one dimension (equation (2.4)) and two dimensional radial imbibition in one plane (equation (2.23)).

In chapter 3, we studied the elastic beam/rod buckling under lateral constraints in two dimension as well as in three dimension. For the two dimensional case with unique boundary condition at both ends, the buckled beam can be divided into sections with

alternate curved section and straight section. The curved section can be solved by the Euler beam equation.The straight sections, however, are key to the transition between different buckling modes, and the straight sections set the upper limit and lower limit for the transition. We compared our theoretical model and FEM simulation in software ABAQUS with good agreement. We then applied this model to explain the crawling snake in horizontal plane between parallel walls which shows unique shape like square wave. For the three dimensional buckling rod confined in cylindrical constraints, three stages are found for the buckling and post buckling process: initial 2D shape, 3D spiral shape and final foldup shape. We characterize the shape at each stage, and then we calculate the transition points between the three stages using geometrical arguments for energy arguments. The theoretical analysis for three dimensional beam/rod are also complemented with FEM simulations from ABAQUS.

In chapter 4, we investigated the buckling shape of solid shell filled with liquid core in two dimension and three dimension. A material model for liquid is first described that can be readily incorporated in the framework of solid mechanics. We then applied this material model in two dimensional and three dimensional Finite Element Method simulation using software ABAQUS. For the two dimensional liquid core solid shell model, a linear analysis is first performed to find out ellipse corresponds to lowest order of buckling with smallest elastic energy. FEM simulation is then performed to determine the nonlinear post-buckling process. We discover that 2D liquid core solid shell structure

converge to peanut shape eventually while the evolution process is determined by two dimensionless parameters $K\tau/\mu$ and $\rho R^2/\mu\tau$. Amorphous shape exists before final peanut shape for certain models with specific $K\tau/\mu$ and $\rho R^2/\mu\tau$. For the three dimensional liquid core solid shell model, the post buckling shape is studied from FEM simulations in ABAQUS. Depending on the strain loading rate, the deformations show distinctive patterns. Large loading rate induces herringbone pattern on the surface of solid shell which resembles solid core solid shell structure, while small loading rate induces major concave pattern which resemble empty solid shell structure. For both two dimensional and three dimensional liquid core system, small scale ordered deformation pattern can be generated by increasing the shear stress in liquid core.

In each of the three subjects in this thesis, we have showcased that geometry is playing a huge role. In chapter 2, the size of wetted area in one dimensional imbibition, two dimensional radial imbibition and three dimensional imbibition all show different trends with respect to time. In chapter 3, straight line contact between beam and constraints are found in the two dimensional case, but no straight line contact exists in the three dimensional case. And the transition between different buckling mode for two dimensional cases and three dimensional cases exhibit huge contrast. In chapter 4, the post buckling two dimensional peanut shape can't be expanded to three dimensional major concave pattern. And the curvature in three dimensional shape plays an important role in determining the deformation pattern. Actually the geometry induced phenomena has been investigated in

related studies, one case being coffee ring effect where the evaporate flux reaches maximum value at the contact line because the open angle and consequently space for vapor diffusion is largest at the contact line if we consider the droplet in two dimensional radial geometry [121]. The liquid flow and evaporate flux are illustrate in the following Figure 5.3.

5.2 Recommendations for future work

5.2.1 Imbibition with gravity

In chapter 2, we studied the imbibition in the absence of gravity (or in the regime where gravity is negligible). However, the gravity comes into play when wetted area is large enough. Taking upwards 1D imbibition for example, where the gravity acts to slow down the diffusion process, the pressure gradient in equation (2.3) is revisited to incorporate gravity ρgl:

$$l\frac{dl}{dt} = \frac{k}{\mu}(p_c - \rho g l) \tag{5.1}$$

In the upwards 1D imbibition, the length l will reach a value L_{critical} where the gravity is equal to capillary pressure P_c. and it is $L_{\text{critical}} = P_c/\rho g$. This critical value is called capillary rise and is an important concept in the microfluidics. On the contrary, when the imbibition is going downwards, the gravity acts to accelerate the imbibition process, the minus sign in parenthesis in equation (5.1) becomes plus sign.

Equation (5.1) is a first order nonlinear Ordinary Differential Equation. Although

its analytical solutions are difficult to obtain, it is relative easy to solve numerically. However in the two dimensional geometry and three dimensional geometry, the gravity is not always aligned with the imbibition direction. So we do not have an elegant governing equation as (2.10) and (2.20) as the pressure difference should be revisited to reflect gravity similarly. FEM software is a good way to solve this problem as we did in section 2.3. It is expected the wetted shape will be an ellipse or ellipsoid, but the quantitative results should come from the simulations. This study will be practically helpful for the bloodstain analysis in the forensics [14] and the understanding of oil transportation in the porous soil.

5.2.2 Improvement for the three dimensional buckled beam under lateral constraints

We have examined buckling and post buckling patterns for the three dimensional beam under cylindrical constraints in chapter 3. Several stages of the buckling and post buckling process, *i.e.* initial 2D stage, 3D spiral stage and foldup stage, and the transition between these stages have been studied in the FEM simulation. Experiments of the 3D buckled beam with constraints are currently underway, and it is helpful to compare the experimental results to the results detailed in section 3.3.

We have proposed a theoretic frame work to explain the strain energy at helix shape and alpha shape. We employ the established results from literature to describe the shape at helix stage and alpha stage. A few assumptions are made at current stage of study

and they need to be considered in the further research. First the helix in Chapter 3 is assumed to be uniform without two ends with are fixed at the central axis of cylindrical constraints. We have chosen data points in Figure 3.24 from long beam to minimize the effect of the two ends, but the exact shape with the consideration of two ends are of academic interest in the following, and we can identify the contribution from two ends by solving for the exact shape. Second we use a solution template for the alpha shape stemmed from literature, but the current description for alpha shape don't consider the radius of constraints explicitly. So an updated version of analytical description for the alpha shape will bring more accurate calculation of strain energies, which leads to more accurate transition point for the secondary buckling.

We also mention that we can utilize the buckled beam under lateral constraints as an energy collecting mechanism in section 3.4. Releasing mechanism of stored energy is also briefly discussed in Figure 3.25. Based on current collecting and releasing mechanism, we could design a small scale device to recycle the minute kinetic energy in the environment. In order to do that, we need to study the beam buckling under different lateral constraints other that cylindrical shape, such as the square shape and triangular shape of which one boundary could be readily removed to release the beam.

5.2.3 The protruding pattern on three dimensional core shell structure

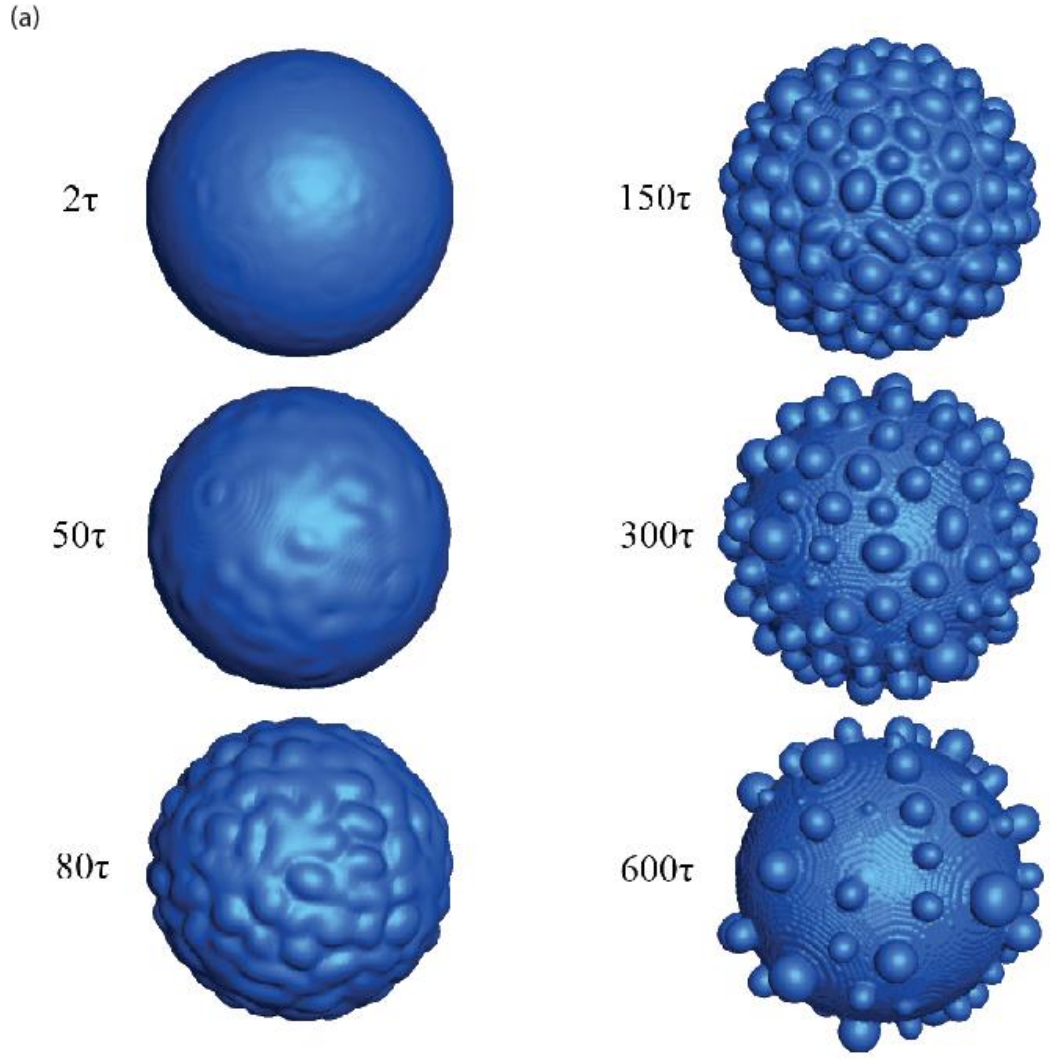

Figure 5.1 The evolution of nanoscale solid core solid shell structure using phase field method [122], τ is the typical time scale used in the computation

We have stated that ordinary buckling and post buckling for initial spherical structures take the shape of concave pattern, as explained in Figure 4.3. But in Figure 4.4 an interesting protruding pattern appears on the surface of spherical silica shell silver core structure. We have proved in our studies that solid shell liquid core structure can't generate convex pattern by only considering the strain energy. Currently we have been using phase

field method to calculate the redistribution of silica shell as illustrate in Figure 5.1. During the evolution, the underling silver core doesn't change, but the molecules in silica shell relocate to form the small scale hills due to high diffusion rate at high temperature and nanoscale. The whole process is governed by the energy minimization by considering the mechanical strain energy and chemical energy. This method is effective on predicting the morphology of shell on the cylindrical surface, study on spherical structure requires new efforts.

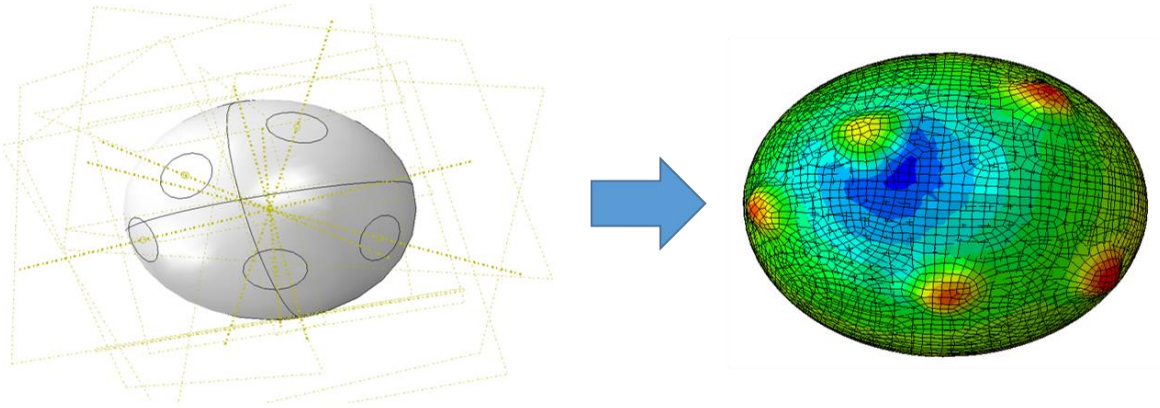

Figure 5.2 Delamination between solid shell and solid core and subsequent growth of protruding pattern

Phase field method in Figure 5.1 provides one possible explanation for the convex pattern on spherical core shell structure. The evolution described in phase field method takes a long time and the high temperature is a prerequisite, so it is possible that the convex shape doesn't come into full fledge at the beginning of cooling process. But the aggregation of silica molecules at different locations would serve as the initiation of delamination between shell and core during the cooling process. Once the delamination sites form, the shrinking of the core shell structure will generate protruding pattern on the delamination

sites as Figure 5.2 illustrated. A combination work of phase field simulation and delamination is still in process.

5.2.4 Manipulate micro/nano particles using liquid flow

Another direction has been under consideration recently, which is related to currently studies of fluid solid interaction: interaction between liquid and small particles. While we have studied the fluid imbibition in the particle assemble, particles are also possible to move with the surrounding fluid. So we could utilize natural fluid or designed flow to deposit microscale or nanoscale particles into ordered patterns. Researcher have studied the spontaneous assembly of microscale particle in the drying process of droplet of particle suspension on a flat substrate, so we could observe that exterior of the coffee stain is much darker than that of interior because small particles in the coffee droplet are transported to the exterior [31, 121, 123].

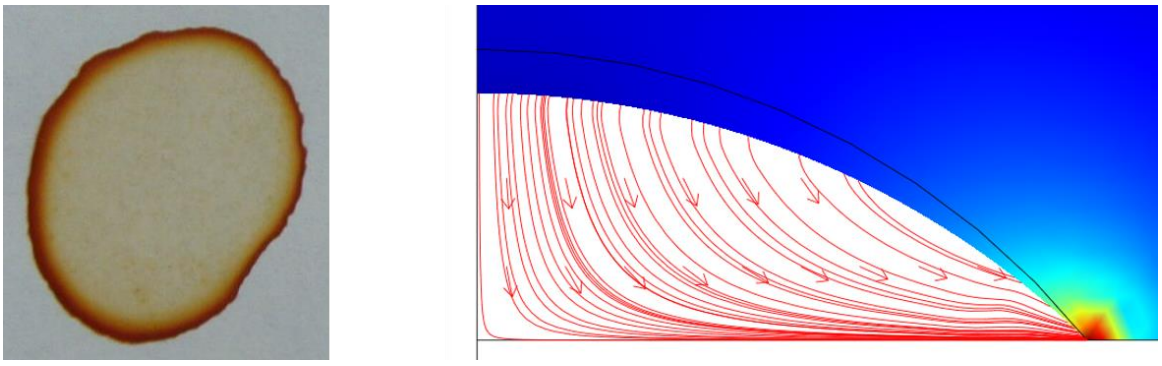

Figure 5.3 Coffee ring effect. The left side depicts a dried coffee stain; the right side illustrates 2D axi-symmetrical model of an evaporating droplet, arrows indicate the streamline in the droplet, color indicates the evaporative flux (highest on the contact line).

Furthermore, we could employ the same principle to deposit particles to desired

position, but in a more controllable manner [32, 124]. This is to switch contact line from a circle to straight line and move the substrate upon which the particles are deposited according to the transportation rate of particles. But controlling the evaporation rate and moving speed of substrate, we can obtain monolayer or bilayer or multiple layers of ordered particles assembly. This particle deposition will be useful to modify the optical properties of surface, such as reflectivity [125], and can serve as a precursor for the photonic crystal [126] or novel photolithography [127].

The transportation of particle with the flow of liquid would be difficult to analyze theoretically since it involves multiple physics coupled with each other. This process is usually demonstrated through experiments, and people are trying to simulate it using FEM [128]. The problem with FEM is that it is hard to deal with multiphase in fluidics, and it is extremely hard to process the topological change, such as coalescence or breakup of droplets and bubbles. The intrinsic discrete methods such Lattice Boltzmann Method would be a candidate for simulation of particles, droplets and bubbles.

Bibliography

1. Stone, H.A. and S. Kim, *Microfluidics: Basic issues, applications, and challenges.* AIChE Journal, 2001. **47**(6): p. 1250-1254.

2. Stone, H.A., A.D. Stroock, and A. Ajdari, *ENGINEERING FLOWS IN SMALL DEVICES.* Annual Review of Fluid Mechanics, 2004. **36**(1): p. 381-411.

3. Gennes, P.G., F. Brochard-Wyart, and D. Quéré, *Capillarity and wetting phenomena: drops, bubbles, pearls, waves*. 2004: Springer.

4. Roman, B. and J. Bico, *Elasto-capillarity: deforming an elastic structure with a liquid droplet.* J Phys Condens Matter, 2010. **22**(49): p. 493101.

5. Chen, X. and J. Yin, *Buckling patterns of thin films on curved compliant substrates with applications to morphogenesis and three-dimensional micro-fabrication.* Soft Matter, 2010. **6**(22): p. 5667.

6. Whitesides, G.M. and B. Grzybowski, *Self-Assembly at All Scales.* Science, 2002. **295**(5564): p. 2418-2421.

7. D'Onofrio, T.G., et al., *Experimental and numerical study of spread and sorption of VX sessile droplets into medium grain-size sand.* Langmuir, 2009. **26**(5): p. 3317-3322.

8. Mendez, S., et al., *Imbibition in porous membranes of complex shape: quasi-stationary flow in thin rectangular segments.* Langmuir, 2009. **26**(2): p. 1380-1385.

9. *Modeling Guide of COMSOL 3.5a*.

10. ABAQUS, *ABAQUS 6.4 User's Manual*. 2004: ABAQUS Inc.

11. Hall, C., *Comment on "Source-like Solution for Radial Imbibition into a Homogeneous Semi-infinite Porous Medium".* Langmuir, 2012. **28**(22): p. 8587-8587.

12. Alava, M., M. Dubé, and M. Rost, *Imbibition in disordered media.* Advances in Physics, 2004. **53**(2): p. 83-175.

13. MacDonell, H.L., *Bloodstain Patterns*. Second ed.: Laboratory of Forensic Science.

14. Attinger, D., et al., *Fluid dynamics topics in bloodstain pattern analysis: Comparative review and research opportunities.* Forensic Science International, 2013. **231**(1–3): p. 375-396.

15. Osborn, J.L., et al., *Microfluidics without pumps: reinventing the T-sensor and H-filter in paper networks.* Lab on a Chip, 2010. **10**(20): p. 2659-2665.

16. Martinez, A.W., et al., *Patterned Paper as a Platform for Inexpensive, Low-Volume, Portable Bioassays.* Angewandte Chemie International Edition, 2007. **46**(8): p. 1318-1320.

17. Washburn, E.W., *The dynamics of capillary flow.* Physical Review, 1921. **17**(3): p. 273.

18. Reyssat, M., et al., *Imbibition in geometries with axial variations.* Journal of Fluid Mechanics, 2008. **615**: p. 335-344.

19. Gruener, S., et al., *Capillary rise of water in hydrophilic nanopores.* Physical Review E, 2009. **79**(6): p. 067301.

20. Clarke, A., et al., *Spreading and Imbibition of Liquid Droplets on Porous Surfaces.* Langmuir, 2002. **18**(8): p. 2980-2984.

21. Anderson, D.M., *Imbibition of a liquid droplet on a deformable porous substrate.* Physics of Fluids, 2005. **17**(8): p. 087104.

22. Hilpert, M. and A. Ben-David, *Infiltration of liquid droplets into porous media: Effects of dynamic contact angle and contact angle hysteresis.* International Journal of Multiphase Flow, 2009. **35**(3): p. 205-218.

23. Oko, A., P. Claesson, and A. Swerin, *Imbibition and Evaporation of Water Droplets on Paper and Solid Substrates.* Journal of Imaging Science and Technology, 2011.

55(1): p. 10201-1-10201-6.

24. Mason, G., et al., *Spontaneous Counter-Current Imbibition into Core Samples with All Faces Open.* Transport in Porous Media, 2009. **78**(2): p. 199-216.

25. Xiao, J., R. Bhardwaj, and D. Attinger. *Manufacturing self-assembled coatings of micro- and nano-particles by controlled evaporation of drops and thin films*. in *Micro- and Nanotechnology Sensors, Systems, and Applications III*. 2011. Orlando, Florida, USA: SPIE.

26. Zou, R.P., M.L. Gan, and A.B. Yu, *Prediction of the porosity of multi-component mixtures of cohesive and non-cohesive particles.* Chemical Engineering Science, 2011. **66**(20): p. 4711-4721.

27. Reyssat, M., et al., *Imbibition in layered systems of packed beads.* EPL (Europhysics Letters), 2009. **86**(5): p. 56002.

28. Coelho, D., J.F. Thovert, and P.M. Adler, *Geometrical and transport properties of random packings of spheres and aspherical particles.* Physical Review E, 1997. **55**(2): p. 1959-1978.

29. Bear, J., *Dynamics of Fluids in Porous Media*. 1988: Dover.

30. Kralchevsky, P.A. and N.D. Denkov, *Capillary forces and structuring in layers of colloidal particles.* Curr. Opin. Collidal Interface Sci., 2001. **6**(4): p. 383.

31. Hu, H. and R.G. Larson, *Evaporation of a sessile droplet on a substrate.* J. Phys. Chem., 2002. **106**(6): p. 1334.

32. Chen, K., et al., *Restricted meniscus convective self-assembly.* Journal of Colloid and Interface Science, 2010. **344**(2): p. 315-320.

33. VanWylen G J, S.R. E., and B. C., *Fundamentals of Classical Thermodynamics*. 1994.

34. Timoshenko, S.P. and J.M. Gere, *Theory of Elastic Stability*. second, reprint ed. 2009: Dover Publications.

35. Adan, N., I. Sheinman, and E. Altus, *Post-buckling behavior of beams under contact constraints.* Journal of Applied Mechanics, Transactions ASME, 1994. **61**(4): p. 764-772.

36. Chai, H., *The post-buckling response of a bi-laterally constrained column.* Journal of the Mechanics and Physics of Solids, 1998. **46**(7): p. 1155-1181.

37. Chai, H., *On the post-buckling behavior of bilaterally constrained plates.* International Journal of Solids and Structures, 2002. **39**(11): p. 2911-2926.

38. Su, T., et al., *Buckling of an elastic rod embedded on an elastomeric matrix: planar vs. non-planar configurations.* Soft Matter, 2014. **10**(33): p. 6294-6302.

39. Su, T., et al., *Mechanism by which a frictionally confined rod loses stability under initial velocity and position perturbations.* International Journal of Solids and Structures, 2013. **50**(14–15): p. 2468-2476.

40. Brangwynne, C.P., et al., *Microtubules can bear enhanced compressive loads in living cells because of lateral reinforcement.* The Journal of Cell Biology, 2006. **173**(5): p. 733-741.

41. Marvi, H. and D.L. Hu, *Friction enhancement in concertina locomotion of snakes.* Journal of The Royal Society Interface, 2012. **9**(76): p. 3067-3080.

42. Hu, D.L., et al., *The mechanics of slithering locomotion.* Proceedings of the National Academy of Sciences, 2009. **106**(25): p. 10081-10085.

43. Guo, Z.V. and L. Mahadevan, *Limbless undulatory propulsion on land.* Proceedings of the National Academy of Sciences, 2008. **105**(9): p. 3179-84.

44. Gray, J., *The Mechanism of Locomotion in Snakes.* Journal of Experimental Biology, 1946. **23**(2): p. 101-120.

45. Jayne, B.C., *Muscular mechanisms of snake locomotion: an electromyographic study of the sidewinding and concertina modes of Crotalus cerastes, Nerodia fasciata and Elaphe obsoleta.* Journal of Experimental Biology, 1988. **140**(1): p. 1-33.

46. Pocheau, A. and B. Roman, *Uniqueness of solutions for constrained Elastica.* Physica D: Nonlinear Phenomena, 2004. **192**(3–4): p. 161-186.

47. Shan, W.L., et al., *Attenuated short wavelength buckling and force propagation in a biopolymer-reinforced rod.* Soft Matter, 2013. **9**(1): p. 194-199.

48. Chai, H., *On optimizing crash energy and load-bearing capacity in cellular structures.* International Journal of Solids and Structures, 2008. **45**(2): p. 528-539.

49. Thompson, J.M.T., et al., *Helical post-buckling of a rod in a cylinder: with applications to drill-strings.* Proceedings of the Royal Society A: Mathematical, Physical and Engineering Sciences, 2012. **468**(2142): p. 1591-1614.

50. Wu, J. and H.C. Juvkam-Wold, *Buckling and Lockup of Tubulars in Inclined Wellbores.* Journal of Energy Resources Technology, 1995. **117**(3): p. 208-213.

51. Miller, J.T., et al., *Buckling-induced lock-up of a slender rod injected into a horizontal cylinder.* International Journal of Solids and Structures, 2015. **72**: p. 153-164.

52. Shi, Y. and J.E. Hearst, *The Kirchhoff elastic rod, the nonlinear Schrödinger equation, and DNA supercoiling.* Journal of Chemical Physics, 1994. **101**(6): p. 5186.

53. Nizette, M. and A. Goriely, *Towards a classification of Euler–Kirchhoff filaments.* Journal of Mathematical Physics, 1999. **40**(6): p. 2830-2866.

54. Podvratnik, M., *Torsional instability of elastic rods*. 2011.

55. Coyne, J., *Analysis of the formation and elimination of loops in twisted cable.* Oceanic Engineering, IEEE Journal of, 1990. **15**(2): p. 72-83.

56. Liu, Y., *Nonlinear Mechanics of Thin Elastic Rod: Theoretical Basis of Mechanical Model of DNA*. 2006, Beijing: Springer.

57. Goriely, A. and M. Tabor, *Nonlinear dynamics of filaments. IV Spontaneous looping of twisted elastic rods.* Proceedings of the Royal Society of London A:

Mathematical, Physical and Engineering Sciences, 1998. **454**(1980): p. 3183-3202.

58. Mahadevan, L. and J.B. Keller. *Coiling of Flexible Ropes*. in *Proceedings: Mathematical, Physical and Engineering Sciences*. 1996. Royal Society.

59. Fang, J., S.-Y. Li, and J.-S. Chen, *On a compressed spatial elastica constrained inside a tube.* Acta Mechanica, 2013. **224**(11): p. 2635-2647.

60. Chen, J.-S. and H.-C. Li, *On an Elastic Rod Inside a Slender Tube Under End Twisting Moment.* Journal of Applied Mechanics, 2011. **78**(4): p. 041009-041009.

61. Thompson, J.M.T. and A.R. Champneys, *From Helix to Localized Writhing in the Torsional Post-Buckling of Elastic Rods.* Proceedings of the Royal Society of London A: Mathematical, Physical and Engineering Sciences, 1996. **452**(1944): p. 117-138.

62. Yin, J., et al., *Stress-driven buckling patterns in spheroidal core/shell structures.* Proceedings of the National Academy of Sciences, 2008. **105**(49): p. 19132-19135.

63. Gerbode, S.J., et al., *How the Cucumber Tendril Coils and Overwinds.* Science, 2012. **337**(6098): p. 1087-1091.

64. Hirose, S., *Biologically inspired robots: snake-like locomotors and manipulators*. 1993: Oxford University Press.

65. Bowden, N., et al., *Spontaneous formation of ordered structures in thin films of metals supported on an elastomeric polymer.* Nature, 1998. **393**(6681): p. 146-149.

66. Davidovitch, B., et al., *Prototypical model for tensional wrinkling in thin sheets.* Proceedings of the National Academy of Sciences, 2011. **108**(45): p. 18227-32.

67. Vaziri, A. and L. Mahadevan, *Localized and extended deformations of elastic shells.* Proceedings of the National Academy of Sciences, 2008. **105**(23): p. 7913-8.

68. Li, B., et al., *Mechanics of morphological instabilities and surface wrinkling in soft materials: a review.* Soft Matter, 2012. **8**(21): p. 5728.

69. Holmes, D.P. and A.J. Crosby, *Draping Films: A Wrinkle to Fold Transition.* Physical Review Letters, 2010. **105**(3): p. 038303.

70. Brau, F., et al., *Wrinkle to fold transition: influence of the substrate response.* Soft Matter, 2013. **9**(34): p. 8177-8186.

71. Cai, S., et al., *Osmotic collapse of a void in an elastomer: breathing, buckling and creasing.* Soft Matter, 2010. **6**(22): p. 5770-5777.

72. Cai, S., et al., *Creasing instability of elastomer films.* Soft Matter, 2012. **8**(5): p. 1301-1304.

73. Chen, X. and J.W. Hutchinson, *Herringbone Buckling Patterns of Compressed Thin Films on Compliant Substrates.* Journal of Applied Mechanics, 2004. **71**(5): p. 597-603.

74. Chen, X. and J.W. Hutchinson, *A family of herringbone patterns in thin films.* Scripta Materialia, 2004. **50**(6): p. 797-801.

75. Pocivavsek, L., et al., *Stress and Fold Localization in Thin Elastic Membranes.* Science, 2008. **320**(5878): p. 912-916.

76. Huang, J., et al., *Capillary Wrinkling of Floating Thin Polymer Films.* Science, 2007. **317**(5838): p. 650-653.

77. Vella, D., M. Adda-Bedia, and E. Cerda, *Capillary wrinkling of elastic membranes.* Soft Matter, 2010. **6**(22): p. 5778-5782.

78. King, H., et al., *Elastic sheet on a liquid drop reveals wrinkling and crumpling as distinct symmetry-breaking instabilities.* Proceedings of the National Academy of Sciences, 2012. **109**(25): p. 9716-9720.

79. Huang, R. and Z. Suo, *Instability of a compressed elastic film on a viscous layer.* International Journal of Solids and Structures, 2002. **39**(7): p. 1791-1802.

80. Huang, R. and Z. Suo, *Very thin solid-on-liquid structures: the interplay of flexural rigidity, membrane force, and interfacial force.* Thin Solid Films, 2003. **429**(1–2):

p. 273-281.

81. Pineirua, M., et al., *Capillary buckling of a floating annulus.* Soft Matter, 2013. **9**(46): p. 10985-10992.

82. Jiang, H., et al., *Finite deformation mechanics in buckled thin films on compliant supports.* Proceedings of the National Academy of Sciences, 2007. **104**(40): p. 15607-15612.

83. Ko, H.C., et al., *A hemispherical electronic eye camera based on compressible silicon optoelectronics.* Nature, 2008. **454**(7205): p. 748-753.

84. Chen, Y., et al., *Mechanism of the Transition From In-Plane Buckling to Helical Buckling for a Stiff Nanowire on an Elastomeric Substrate.* Journal of Applied Mechanics, 2016. **83**(4): p. 041011-041011.

85. Lazarus, A., H.C.B. Florijn, and P.M. Reis, *Geometry-Induced Rigidity in Nonspherical Pressurized Elastic Shells.* Physical Review Letters, 2012. **109**(14): p. 144301.

86. Stoop, N., et al., *Curvature-induced symmetry breaking determines elastic surface patterns.* Nat Mater, 2015. **14**(3): p. 337.

87. Cao, G., et al., *Self-Assembled Triangular and Labyrinth Buckling Patterns of Thin Films on Spherical Substrates.* Physical Review Letters, 2008. **100**(3): p. 036102.

88. Cao, Y.-P., B. Li, and X.-Q. Feng, *Surface wrinkling and folding of core-shell soft cylinders.* Soft Matter, 2012. **8**(2): p. 556-562.

89. Vella, D., et al., *Indentation of Ellipsoidal and Cylindrical Elastic Shells.* Physical Review Letters, 2012. **109**(14): p. 144302.

90. Vella, D., et al., *The indentation of pressurized elastic shells: from polymeric capsules to yeast cells.* J R Soc Interface, 2012. **9**(68): p. 448-55.

91. Vella, D., et al., *Wrinkling of Pressurized Elastic Shells.* Physical Review Letters, 2011. **107**(17).

92. Quilliet, C., *Numerical deflation of beach balls with various Poisson's ratios: From sphere to bowl's shape.* The European Physical Journal E, 2012. **35**(6): p. 1-9.

93. Aumaitre, E., et al., *Wrinkling in the deflation of elastic bubbles.* The European Physical Journal E, 2013. **36**(3): p. 1-5.

94. Pogorelov, A.V.e., *Bendings of Surfaces and Stability of Shells*. 1988: American Mathematical Society.

95. Li, C., X. Zhang, and Z. Cao, *Triangular and Fibonacci Number Patterns Driven by Stress on Core/Shell Microstructures.* Science, 2005. **309**(5736): p. 909-911.

96. Yin, J., X. Chen, and I. Sheinman, *Anisotropic buckling patterns in spheroidal film/substrate systems and their implications in some natural and biological systems.* Journal of the Mechanics and Physics of Solids, 2009. **57**(9): p. 1470-1484.

97. Datta, S.S., H.C. Shum, and D.A. Weitz, *Controlled buckling and crumpling of nanoparticle-coated droplets.* Langmuir, 2010. **26**(24): p. 18612-6.

98. Datta, S.S., et al., *Delayed Buckling and Guided Folding of Inhomogeneous Capsules.* Physical Review Letters, 2012. **109**(13): p. 134302.

99. Gordon, V.D., et al., *Self-Assembled Polymer Membrane Capsules Inflated by Osmotic Pressure.* Journal of the American Chemical Society, 2004. **126**(43): p. 14117-14122.

100. Xu, H., et al., *Shape and Buckling Transitions in Solid-Stabilized Drops†.* Langmuir, 2005. **21**(22): p. 10016-10020.

101. Cui, M., T. Emrick, and T.P. Russell, *Stabilizing liquid drops in nonequilibrium shapes by the interfacial jamming of nanoparticles.* Science, 2013. **342**(6157): p. 460-3.

102. Boulogne, F., F. Giorgiutti-Dauphine, and L. Pauchard, *The buckling and invagination process during consolidation of colloidal droplets.* Soft Matter, 2013. **9**(3): p. 750-757.

103. Kim, D.H., et al., *Mechanical Properties and Microstructure of Polycrystalline Phospholipid Monolayer Shells: Novel Solid Microparticles.* Langmuir, 2003. **19**(20): p. 8455-8466.

104. Finan, J., et al., *Nonlinear Osmotic Properties of the Cell Nucleus.* Annals of Biomedical Engineering, 2009. **37**(3): p. 477-491.

105. Finan, J.D. and F. Guilak, *The effects of osmotic stress on the structure and function of the cell nucleus.* J Cell Biochem, 2010. **109**(3): p. 460-7.

106. Vaziri, A. and M.R.K. Mofrad, *Mechanics and deformation of the nucleus in micropipette aspiration experiment.* Journal of Biomechanics, 2007. **40**(9): p. 2053-2062.

107. Vaziri, A., H. Lee, and M.R.K. Mofrad, *Deformation of the cell nucleus under indentation: Mechanics and mechanisms.* Journal of Materials Research, 2006. **21**(08): p. 2126-2135.

108. Yeung, A. and E. Evans, *Cortical shell-liquid core model for passive flow of liquid-like spherical cells into micropipets.* Biophysical Journal, 1989. **56**(1): p. 139-149.

109. Gracheva, M. and H. Othmer, *A continuum model of motility in ameboid cells.* Bulletin of Mathematical Biology, 2004. **66**(1): p. 167-193.

110. Hoffman, B.D. and J.C. Crocker, *Cell Mechanics: Dissecting the Physical Responses of Cells to Force.* Annual Review of Biomedical Engineering, 2009. **11**(1): p. 259-288.

111. Gao, C., et al., *Elasticity of hollow polyelectrolyte capsules prepared by the layer-by-layer technique.* The European Physical Journal E, 2001. **5**(1): p. 21-27.

112. Guilak, F., J.R. Tedrow, and R. Burgkart, *Viscoelastic Properties of the Cell Nucleus.* Biochemical and Biophysical Research Communications, 2000. **269**(3): p. 781-786.

113. Lim, C.T., E.H. Zhou, and S.T. Quek, *Mechanical models for living cells—a review.* Journal of Biomechanics, 2006. **39**(2): p. 195-216.

114. Stone, H.A., *Dynamics of Drop Deformation and Breakup in Viscous Fluids.* Annual Review of Fluid Mechanics, 1994. **26**(1): p. 65-102.

115. Ristenpart, W.D., et al., *Non-coalescence of oppositely charged drops.* Nature, 2009. **461**(7262): p. 377-380.

116. Grotberg, J.B. and O.E. Jensen, *BIOFLUID MECHANICS IN FLEXIBLE TUBES.* Annual Review of Fluid Mechanics, 2004. **36**(1): p. 121-147.

117. Zu, W.-H., et al., *Immersed Boundary-Lattice Boltzmann Method for Biological and Biomedical Flows*, in *Parallel Computational Fluid Dynamics: 25th International Conference, ParCFD 2013, Changsha, China, May 20-24, 2013. Revised Selected Papers*, K. Li, et al., Editors. 2014, Springer Berlin Heidelberg: Berlin, Heidelberg. p. 383-392.

118. Peskin, C.S., *The immersed boundary method.* Acta Numerica, 2002. **11**: p. 479-517.

119. Stone, H.A., A.M. Forsyth, and J. Wan, *Viewpoint: Slipping through blood flow.* Physics, 2009. **2**: p. 89.

120. Kaoui, B., G. Biros, and C. Misbah, *Why Do Red Blood Cells Have Asymmetric Shapes Even in a Symmetric Flow?* Physical Review Letters, 2009. **103**(18): p. 188101.

121. Deegan R. D, et al., *Capillary flow as the cause of ring stains from dried liquid drops.* Nature, 1997. **389**(6653): p. 827.

122. Liao, X., et al., *Unpublished work.* 2016.

123. Hu, H. and R.G. Larson, *Analysis of microfluid flow in an evaporating sessile droplet.* Langmuir, 2005. **21**(9): p. 3963.

124. Kumnorkaew, P., A.L. Weldon, and J.F. Gilchrist, *Matching Constituent Fluxes for Convective Deposition of Binary Suspensions.* Langmuir, 2009. **26**(4): p. 2401-2405.

125. Malaquin, L., et al., *Controlled Particle Placement through Convective and Capillary Assembly.* Langmuir, 2007. **23**(23): p. 11513-11521.

126. Dushkin C D, et al., *Effect of growth conditions on the structure of two-dimensional latex crystals: experiment.* Colloid Polym. Sci., 1999. **277**(10): p. 914.

127. Xia, Y.N., et al., *Monodispersed colloidal spheres: Old materials with new applications.* Advanced Materials, 2000. **12**(10): p. 693-713.

128. Bhardwaj, R., et al., *Self-Assembly of Colloidal Particles from Evaporating Droplets: Role of DLVO Interactions and Proposition of a Phase Diagram.* Langmuir, 2010. **26**(11): p. 7833-7842.